

3-10-2010

Experimental Validation Techniques for the HELEEOS Off-Axis Laser Propagation Model

John D. Haiducek

Follow this and additional works at: <https://scholar.afit.edu/etd>

 Part of the [Atmospheric Sciences Commons](#), and the [Inorganic Chemistry Commons](#)

Recommended Citation

Haiducek, John D., "Experimental Validation Techniques for the HELEEOS Off-Axis Laser Propagation Model" (2010). *Theses and Dissertations*. 2168.

<https://scholar.afit.edu/etd/2168>

This Thesis is brought to you for free and open access by the Student Graduate Works at AFIT Scholar. It has been accepted for inclusion in Theses and Dissertations by an authorized administrator of AFIT Scholar. For more information, please contact richard.mansfield@afit.edu.



**EXPERIMENTAL VALIDATION
TECHNIQUES FOR THE HELEEOS
OFF-AXIS LASER PROPAGATION MODEL**

THESIS

John Haiducek, 1st Lt, USAF
AFIT/GAP/ENP/10-M07

**DEPARTMENT OF THE AIR FORCE
AIR UNIVERSITY**

AIR FORCE INSTITUTE OF TECHNOLOGY

Wright-Patterson Air Force Base, Ohio

APPROVED FOR PUBLIC RELEASE; DISTRIBUTION UNLIMITED.

The views expressed in this thesis are those of the author and do not reflect the official policy or position of the United States Air Force, Department of Defense, or the United States Government.

AFIT/GAP/ENP/10-M07

EXPERIMENTAL VALIDATION TECHNIQUES FOR THE HELEEOS
OFF-AXIS LASER PROPAGATION MODEL

THESIS

Presented to the Faculty
Department of Physics
Graduate School of Engineering and Management
Air Force Institute of Technology
Air University
Air Education and Training Command
in Partial Fulfillment of the Requirements for the
Degree of Master of Science in Physics

John Haiducek, BS, Physics

1st Lt, USAF

March 2010

APPROVED FOR PUBLIC RELEASE; DISTRIBUTION UNLIMITED.

EXPERIMENTAL VALIDATION TECHNIQUES FOR THE HELEEOS
OFF-AXIS LASER PROPAGATION MODEL

John Haiducek, BS, Physics
1st Lt, USAF

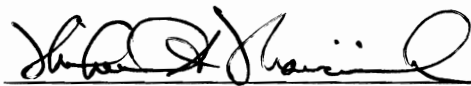
Approved:



Steven T. Fiorino, Ph.D. (Chairman)

23 MAR 10

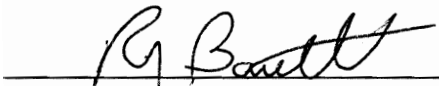
Date



Michael A. Marciniak, Ph.D. (Member)

23 Mar 10

Date



Richard J. Bartell (Member)

23 MR 10

Date

Abstract

The High Energy Laser End-to-End Operational Simulation (HELEEOS) off-axis scattering algorithm is designed to predict the irradiance that will be detected at a given off-axis location due to atmospheric scattering of a high-energy laser. The HELEEOS system models the propagation of the laser through the atmosphere, accounting for such effects as turbulence, thermal blooming, and atmospheric absorption. The HELEEOS off-axis scattering algorithm uses the scattering phase functions of the Mie scattering models to predict the amount of radiation that will be scattered toward a particular observation location from each point along the beam path, and the total irradiance that will be received at that location. Algorithm outputs were compared with data from a laser test conducted at Wright-Patterson Air Force Base using 1.53-1.59 μm communications lasers operating at 0.6 W of power. The off-axis irradiance was measured using an Indium Gallium Arsenide (InGaAs) camera. A software application was developed to assist in camera calibration and the analysis of the collected images. The application was used to reduce the data from each image to a single irradiance value which could be compared with HELEEOS predictions. Preliminary results show an agreement within 1-2 orders of magnitude between the HELEEOS algorithm and the measured off-axis irradiance, although the potential exists for improving this result through more detailed analysis of the same data set.

Acknowledgements

No research is performed in a vacuum, and this project was no exception. First, I would like to thank Chris Rice, who collected all of the field data used in my thesis, and who gave me considerable help in picking up the radiometry concepts required to analyze it. I would like to thank my advisor, Dr. Fiorino, for mentoring me through this project, answering my questions about HELEEOS, and giving me ample conversation about meteorology besides. Dr. Marciniak gave me assistance on radiometry and error analysis at several stages in the process, and Greg Smith helped me figure out how to make my calibration work. LtCol Hawks gave me the suggestion to sample the results in increments along the beam, enabling me to test HELEEOS in more detail with the existing data.

My family, particularly my parents and brother, have been most supportive through this project, including my brother's willingness to go on a crazy long road trip so I can present my results at a conference. My roommates, as well as the rest of my physics department section, have been frequent sources of amusement and perspective. I wish them all well in their next assignments. Like many other grad students, I owe it to Donald Knuth and Leslie Lamport and others for creating \TeX and \LaTeX with which this document was typeset, and to Linus Torvalds et al. for making Unix-like operating systems available to the free world. I would like to thank the Air Force Personnel center for letting me out of my last assignment early so I could go to the Air Force Institute of Technology. Hopefully my next assignment will be equally as wonderful. Finally, I thank God for giving me my self, my life, and all these people who support me through it.

John Haiducek

Contents

	Page
Abstract	iv
Acknowledgements	v
List of Figures	ix
List of Tables	xv
List of Abbreviations	xvi
I. Introduction	1
1.1 Background	2
1.2 Motivation	3
1.3 Problem Statement	4
1.4 Methodology	4
1.5 Overview	5
II. Literature Review	6
2.1 Atmospheric Interaction	6
2.1.1 Absorption	7
2.1.2 Scattering	8
2.1.3 Optical turbulence	13
2.2 Infrared detection	14
2.2.1 InGaAs detector properties	14
2.2.2 CCD detector properties	14
2.3 Gaussian process regression	15
2.4 Laser communications	17
III. Theory	18
3.1 Camera Calibration	18
3.2 Experiment geometry calculations	21
3.2.1 Determining the off-axis angle	22
3.2.2 Entering observer geometry into HELEEOS	22
3.2.3 Locating a pixel position along the beam	23
3.2.4 Relating image irradiances to HELEEOS irradiance	24

	Page
IV. Analysis Process	26
4.1 Camera calibration	26
4.1.1 Analysis of the calibration data	27
4.1.2 Calibration results	35
4.2 Background subtraction	43
4.3 Total irradiance for an image	44
4.4 Error analysis	47
4.5 Computing irradiances in HELEEOS	51
V. Field Measurements	52
5.1 Experiment setup	52
5.2 Image selection	58
5.3 Results	60
VI. Conclusions	68
6.1 Future work	70
6.1.1 Parameter sensitivities	71
6.1.2 Different geometries	71
6.1.3 Higher power tests	72
6.1.4 Improvements to the calibration software	73
6.1.5 Inputting real weather data into HELEEOS	74
6.2 Closing remarks	74
A. Calibration software user documentation	75
1.1 Dependencies	75
1.2 Using	75
1.2.1 Calibration scenarios	77
1.2.2 Loading and editing images	77
1.2.3 Viewing images	78
1.2.4 Overlays	79
1.3 Viewing histograms	80
1.4 Image settings	80
1.4.1 Image section	80
1.4.2 Field Scenario section	80
1.4.3 Optics section	83
B. HELEEOS inputs	85
C. Table of field images with corresponding data	89
Bibliography	122

Vita..... 124

List of Figures

Figure		Page
1	Scattering phase function for Rayleigh scattering in directions θ relative to the propagation direction. Results are shown for light polarized perpendicular, parallel, and unpolarized relative to the scattering direction (based on Figure 12.2 and Equation 12.9 of [14]).	9
2	Effect of polarization on HELEEOS off-axis irradiance outputs. Although polarization can make large differences at high altitudes, it has little effect below 1,200 km.	10
3	Mie scattering phase functions for various size parameters (based on Figure 12.7 of [14]). The radial axis is a logarithmic scale, and the angles are relative to the direction of propagation. Features of note include the peaks at 0° and 180° , corresponding to forward and back scattering, respectively, as well as the fact that all the phase functions reach their minimum values somewhere around 90° . Finally, it should be noted that the scattered intensity increases with the size of the scattering particles, denoted by the size parameter x	12
4	Mie scattering phase functions used in HELEEOS. Both phase functions are computed from the Wiscombe Mie module, but with different size parameters. Note that aerosol scattering dominates; this is because the Mie model predicts stronger scattering for larger particles.	13
5	Responsivity spectrum for a typical InGaAs detector at 25°C with a 5V bias. Based on Figure 7.55 in [9].	14
6	Relative response spectra for CCD detectors. Based on Figure 7.30 in [9].	15
7	Experiment setup with a triangle shown between the observer, source, and a point of interest along the laser beam path.	22

Figure	Page
8	HELEEOS observer geometry settings. The settings in the Initializations section are changed according to the location of the observer. 23
9	HELEEOS computes the total irradiance from a cylindrical length of the beam, while each pixel of an image records the total irradiance scattered from points in its field of view. To compare the two, irradiances from multiple pixels must be combined such that they contain the cylindrical region being integrated in HELEEOS. 25
10	The telescopes and camera used for the field data collection. The 10.10 cm refracting telescope can be seen attached to the side of the larger 31.75 cm reflecting telescope, with the camera (the blue cube) attached to the back of the smaller telescope. 27
11	Blackbody images taken with a mask over the blackbody, used for spatial calibration. 28
12	Histograms of raw camera data. Top: Histogram of an image with many underexposed pixels. Middle: Histogram of an image with many overexposed pixels. Bottom: A good histogram. 30
13	Camera response versus integration time for a 300 C blackbody. Note the erratic behavior between 2000 and 3000 μs . This image shows data for the pixel at (91,118), but other pixels behave similarly. 31
14	Blackbody images showing banding artifacts. 32
15	Planck emissivity curves for the various blackbody temperatures. 33
16	The transmittance spectrum of the filter. 34

Figure	Page
17	Camera response versus energy received for various blackbody temperatures and integration times. Linear fits are shown for each of the blackbody temperatures for which at least 2 points are available; the positive slope of each line is a result of increasing integration time. The range of integration times used is listed in the legend of Figure 18. 36
18	The same data set as seen in Figure 17, with linear fits conducted on groups of points having the same integration time. Most of the lines are parallel, suggesting that the offset varies as a function of integration time but the gain varies very little. The exception to this is an integration time for which only two close-together points were available, resulting the line running across the bottom of the plot. 38
19	Gain and Offset versus integration time and temperature. The integration time relationship is largely linear beyond 3000 μs (a larger number of data points below 2500 μs might reveal a separate linear domain in that region), while the gain shows only weak dependence on integration time. The offset shows no consistent temperature dependence, but the gain shows a nonlinear temperature dependence. 39
20	Result of including integration time in the regression process. 40

21	Image plots of the calibration result. Magenta-colored pixels are considered “bad.” The gain array (upper left) characterizes the way the camera output varies as the incoming radiation is increased. The dark region in the middle of the gain array is probably caused by a temperature gradient over the surface of the blackbody (the blackbody tends to be hottest in the middle). The offset array (upper right) represents the camera’s output in the absence of incident radiation; the vertical lines in the offset array are responsible for removing similar features from images taken with the camera. The array of integration time coefficients (lower left) is a correction factor which had to be added to the offset array, probably due to dark currents or stray radiation entering the system. The variance array (lower right) is the sum of the residuals for all of the images; it gives an indication of the errors associated with the linear fit. 42	42
22	Observer optics settings in HELEEOS. The analysis software maps the distance ranges under “Linear Focusing” (here identified by a red box) to a region of pixels in the image. 45	45
23	Parameters defining the selection region. All angles and distances are defined relative to the location of the beam source, and were entered manually. The angle θ defines the apparent direction of the beam, clockwise from the horizontal axis. The selection region includes all pixels whose direction from the beam source is between $\theta - \Delta\theta$ and $\theta + \Delta\theta$, and whose distance from the source is FOV Start and FOV Stop. FOV Start and FOV Stop are typically entered in meters (representing distances along the beam from the source), and are converted to angles and pixel ranges in the observer’s field of view using Equation 25. 46	46
24	The trailer from which the lasers operated when located out doors. The apertures for each laser are at the front of the black cylindrical object pointing out of the trailer. 53	53
25	Optics settings for the lasers. Non-default values are marked in red. 54	54

Figure	Page
26	Building 622 at Wright-Patterson Air Force Base. The target was in the left-most of the two visible windows. 55
27	Experiment geometry for the 15 July 2009 test. For this test, the observer was located almost directly below the beam. The 300 m field of view is representative of the 31.75 cm reflecting telescope, which was used for most of the observations on 15 July. 55
28	Experiment geometry for the 17 July 2009 test. The source is denoted by a laser symbol, the target by a bulls-eye, and the observer by an eyeball. The observer's field of view is identified by a blue line along the laser beam path. The 400 m field of view is representative of the 10.1 cm refracting telescope, which was used for most of the observations on 17 July. 56
29	HELEEOS Scenario page, with fields populated with the input data used for HELEEOS runs in the study. 57
30	Ratios of HELEEOS-derived irradiances to the measured irradiances, as a function of laser power. HELEEOS outputs are always within two orders of magnitude of the measured irradiances, and frequently within one order of magnitude. 61
31	Comparison of HELEEOS-derived irradiances with measured irradiances, showing a weak correlation. 62
32	Angle increments within the selected field of view, used for computing irradiances as a function of viewing angle for Figure 33. 63
33	HELEEOS-predicted irradiance (solid lines) and measured irradiance (points) as a function of observation direction for two images. Although the overall magnitude differs between HELEEOS and the measured irradiance, as does the rate at which the irradiance falls off with distance, the downward trend is present in both. 64

Figure	Page
34	HELEEOS-predicted irradiance as a function of observation direction for an observer located 1.22° off-axis. Each point along the line represents an equal span of angles in the observer's field of view. An observation angle of 0° indicates the observer is looking directly at the source; 90° indicates the observer is looking 90° away from the beam source, approximately perpendicular to the beam. HELEEOS outputs NaN for the irradiance from 75-90°. 65
35	HELEEOS-predicted irradiance as a function of observer off-axis angle. Larger angles indicate the observer was further offset from the beam path, maintaining the same distance from the laser source. The strong dependence of the output on this parameter suggests that accurate results from HELEEOS require an accurate measurement of the experiment geometry. 66
36	The calibration program's main window 76
37	The table of blackbody images 78
38	The table of field images 79
39	Image Settings dialog for a field image 81
40	Image Settings dialog for a blackbody image 82

List of Tables

Table		Page
1	Examples of background subtraction.	59
2	Fields in the Blackbody Images table.	77
3	Fields in the Field Images table.	78
4	View types.	79
5	Options in the Image Settings dialog.	84
6	HELEEOS inputs.	85
7	Properties of the two optical setups.	89
8	Field irradiance and corresponding HELEEOS output (red areas in the images denote the region over which summation was performed)	90

List of Abbreviations

Abbreviation		Page
HELEEOS	High Energy Laser End-to-End Operational Simulation	iv
InGaAs	Indium Gallium Arsenide	iv
ABL	Airborne Laser	2
ATL	Advanced Tactical Laser	2
COIL	Chemical Oxygen Iodine Laser	2
AFRL	Air Force Research Laboratory	4
CCD	charge-coupled device	5

EXPERIMENTAL VALIDATION TECHNIQUES FOR THE HELEEOS OFF-AXIS LASER PROPAGATION MODEL

I. Introduction

The purpose of this thesis is to develop techniques for experimental validating the off-axis propagation algorithm within the High Energy Laser End-to-End Operational Simulation (HELEEOS) model. HELEEOS is a software package developed at the Air Force Institute of Technology to simulate laser propagation through the atmosphere. Its core purpose is to predict the properties of a high energy laser beam at every point along its path, taking into account its interaction with the atmosphere [3]. In 2006, Scott Belton extended the model to simulate off-axis scattering, giving HELEEOS the ability to determine the irradiance received from laser at some off-axis location [3]. Although HELEEOS's basic functionality has been experimentally validated, the off-axis scattering capability has not previously been validated. Tests with an infrared camera and 1-watt infrared lasers at Wright-Patterson Air Force Base provide a means to determine the accuracy of the off-axis scattering model. HELEEOS was designed with high-energy laser weapons in mind, but these tests provide useful data for verifying the off-axis scattering algorithm, as well as to determine the viability of using the same model for lower power communication lasers. Additional tests, conducted in December 2009 at Dahlgren, VA, using a more powerful 20-kilowatt laser, will provide a means to test the model against a high energy laser.

It is assumed that the reader has a basic understanding of laser propagation and atmospheric properties.

1.1 Background

Lasers are operated in the atmosphere for a variety of military applications, including illumination of targets for bombs and missiles, communication, and most recently as experimental directed-energy weapons. Currently the Air Force is building two experimental laser weapons, the Airborne Laser (ABL) and the Advanced Tactical Laser (ATL). Both use a Chemical Oxygen Iodine Laser (COIL). The ATL is carried inside a modified C-130 aircraft and designed to damage ground targets along slant paths of up to 10 km. The ABL, on the other hand, is intended for use against theater ballistic missiles such as the SCUD, and would be operated from a modified Boeing 747 aircraft. The ABL operates at power levels on the order of one megawatt, while the ATL has power outputs on the order of kilowatts [2, 1].

As high-powered lasers become more common, U.S. government agencies will require information about lasers used by our adversaries. Atmospheric scattering makes it possible to observe a laser beam from an off-axis point (i.e. not in the immediate path of the beam), opening the possibility of characterizing the laser by remote observation. Molecules and aerosol particles cause light to be scattered out of the beam in all directions. If the location of the laser, its target, and the observer's location are known, with the atmospheric environment sufficiently well characterized, the power of the laser can be determined from the irradiance of scattered light seen by an off-axis observer. It may also be possible to use the same technique on some communications lasers. A computer program, written by Belton and since integrated into HELEEOS, provides the computational tools to determine off-axis scattered irradiance for a laser of known properties [3].

HELEEOS predicts laser propagation by an empirical method, taking into account a variety of factors including the atmospheric environment, and the laser's ability to compensate for atmospheric turbulence. The model supports scattering calculations

for electromagnetic beams operating between 355 *nm* and 8.6 *m*. HELEEOS provides the intensity of light in all directions at each point along the beam; Belton's model uses this to determine the irradiance received at a particular off-axis point, taking into account extinction of light traveling from the beam to the observer [3].

While Belton's model predicts the off-axis scattered irradiance for a laser whose properties are known, a new feature of HELEEOS due to be added by Eric Magee and William Gruner is the ability to determine the power of a laser based on measurements of off-axis scattering. This feature will be implemented using a Gaussian process regression model to map off-axis irradiances to laser power outputs. The Gaussian process technique also provides the ability to determine a probability distribution to indicate the degree of uncertainty in the prediction [11].

1.2 Motivation

The capability to determine laser power from backscatter would provide a means to determine basic characteristics of noncooperative laser systems. In the case of communications lasers, it may also be possible to collect some portion of the data being transmitted. Thus the technique would provide an important intelligence gathering capability, particularly if laser weapons entered widespread use among U.S. adversaries.

A software model already exists as a component of the HELEEOS computer program. The core functionality of the HELEEOS program, that is, to characterize laser beam propagation for a known laser system, was validated in previous studies. This current study provides an initial validation for the off-axis scattering model developed by Belton, and develops techniques which can be used for future testing.

1.3 Problem Statement

The primary goal of this research is to develop techniques for experimental validation of the HELEEOS off-axis scattering model, and to provide a preliminary assessment of its accuracy. A secondary goal is to determine whether the techniques used to measure off-axis irradiance are effective for communications lasers.

1.4 Methodology

Tests conducted in July 2009 by the Air Force Research Laboratory (AFRL) at Wright-Patterson Air Force Base provided the first set of validation data. The lasers used in the test operated at 1.533, 1.589, and 1.595 μm , within the range supported by HELEEOS, and with power levels varying from 0.6 to 5.7 W. This comparatively low power level may produce results that differ somewhat from megawatt-class COIL lasers of interest, but testing against low powers opens up the possibility of characterizing noncooperative communications lasers as well as laser weapons. The more powerful weapons lasers would likely be easier to detect and measure than these communications lasers.

Additional tests were conducted in December 2009 using a 1.07 μm laser in Dahlgren, VA [11]. These tests used a 20-kilowatt laser intended for use as a weapon, so they help fulfill the need to demonstrate the off-axis scattering technique against a high-energy laser.

Irradiance measurements at the July 2009 test were made with an infrared camera using an Indium-Gallium-Arsenide (InGaAs) array. Although the HELEEOS off-axis scattering module was designed with a single-element detector in mind, the camera provided a more flexible method of data collection. By analyzing the images collected it is possible to clearly distinguish background pixels from laser beam pixels, and the background irradiance can easily be subtracted out to find the irradiance of the

scattered laser light [11]. Furthermore, decisions could be made after the data was collected about which part of the camera's field of view should be analyzed, which might not have been possible using a single-element detector.

Measurements collected during the December 2009 test used a CCD camera. Although CCD's are designed to detect visible light, they have adequate sensitivity at the $1.07 \mu m$ laser wavelength to detect the scattered laser light.

1.5 Overview

HELEEOS simulates a number of mechanisms by which the atmosphere affects laser beam propagation. All of these are described in Chapter II. The most important of these is atmospheric scattering, which will be discussed in greater detail. The scattered light from the optical scattering was collected by an InGaAs camera, which was calibrated against a blackbody. Chapter III discusses the radiometry theory required to calibrate the camera and apply the calibration to field images, while the results of the calibration are described in Chapter IV. The calibration was applied to 56 test cases, which are compared against HELEEOS runs in Chapter V. For those interested, a detailed summary of the input data and results for all the test cases can be found in Appendices B and C.

II. Literature Review

This chapter summarizes some of the fundamental concepts relating to atmospheric laser propagation and scattering detection using infrared cameras. The Gaussian process regression to be used for correlating scattered irradiance with laser power is also described. Finally, a discussion of communications lasers is included as a prelude for later discussion on the viability of using HELEEOS against such lasers.

2.1 Atmospheric Interaction

Lasers interact with the atmosphere in a number of ways. Molecules in the air (primarily CO_2 , N_2 , H_2O , and O_2) may both scatter and absorb radiation. Similarly, aerosols may contribute both scattering and absorption. Finally, optical turbulence (variances in the index of refraction of the air) can perturb the beam position, expanding it over a time average. Turbulence can also cause localized irradiance fluctuations in the beam [22, 18].

For this thesis, the interactions of primary concern are absorption and scattering. Scattering along the beam is necessary for light to reach any off-axis detector, but any additional scattering along the path between the beam and the detector will contribute to extinction, decreasing the observed irradiance. Absorption decreases the irradiance both of the beam itself and of the off-axis scattering.

Regardless of the mechanism, a laser beam's power decays exponentially with distance as long as the atmospheric properties remain constant. The decay rate γ is given by

$$\gamma = \alpha_m + \beta_m + \alpha_a + \beta_a, \quad (1)$$

where α_m and β_m denote absorption and scattering, respectively, by molecules, and

α_a and β_a denote absorption and scattering by aerosol particles [18]. The degree of attenuation at a particular distance is then given by Beer's Law:

$$\tau = \frac{I(z)}{I_0} = e^{-\gamma z}, \quad (2)$$

where τ is the transmittance, γ is the attenuation coefficient, and z is the distance from the source [18]. If the atmospheric properties vary along the beam path, the exponent $-\gamma z$ is replaced by the integral

$$-\int_0^z \gamma(z) dz. \quad (3)$$

The absorption and scattering coefficients depend on the concentrations of the contributing particles, and may be expressed as the product of a cross section with the particle concentration [18]. The cross sections are given as σ_a for absorption and σ_s for scattering, and the absorption and scattering coefficients are given by

$$\alpha = \sigma_a N_a \quad (4)$$

and

$$\beta = \sigma_s N_s, \quad (5)$$

where N_a and N_s are the concentrations of absorbers and scatterers, respectively.

2.1.1 Absorption.

Each molecular species in the atmosphere has a characteristic absorption spectrum which contributes to the total attenuation. Of the molecular species present in the atmosphere, H_2O and CO_2 contribute the most to absorption. These molecules absorb

incident light by changing between various rotational and vibrational modes [18].

Many high energy lasers are designed to operate in “clean-window” bands for which molecular absorption is minimized. For these lasers, scattering is the dominant attenuation mechanism [10].

2.1.2 Scattering.

Atmospheric scattering is commonly treated using two models: Rayleigh scattering and Mie scattering. Rayleigh scattering models scattering by particles, primarily molecules, which are smaller than the size of the wavelength in question. Mie scattering models larger particles for which the shape of the scattering particle is a factor [18].

Rayleigh scattering. Rayleigh scattering occurs when the electric field of the laser beam displaces bound electrons in molecules of the air. This causes a dipole moment which oscillates at the same frequency as the incident field. For light scattered in a direction Ω , the scattered intensity has the proportionality

$$I \propto \omega^4(1 - \sin^2(\theta) \cos^2 \phi), \quad (6)$$

where θ is the angle between Ω and the direction of propagation, and ω is the frequency of the light. ϕ is the angle between the electric field of the polarized light and the component of Ω in a plane perpendicular to the propagation direction [14]. Dropping the frequency dependence gives us the scattering phase function

$$p(\theta, \phi) = \omega^4(1 - \sin^2(\theta) \cos^2 \phi). \quad (7)$$

This scattering profile, also known as the scattering phase function, is shown in Figure 1.

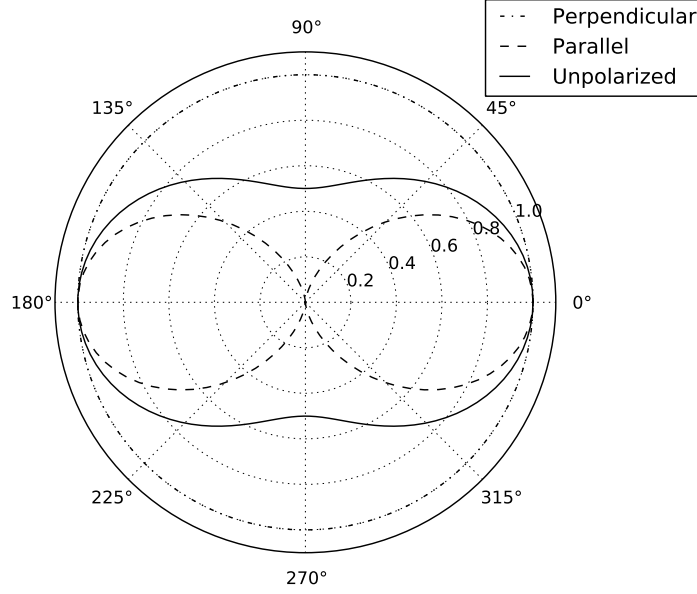


Figure 1. Scattering phase function for Rayleigh scattering in directions θ relative to the propagation direction. Results are shown for light polarized perpendicular, parallel, and unpolarized relative to the scattering direction (based on Figure 12.2 and Equation 12.9 of [14]).

Although the Rayleigh scattering model accounts for polarization effects, HELEEOS treats the light as being unpolarized during propagation, except for considering polarization that is induced by the scattering process itself [11]. Furthermore, no polarization information was available for the lasers used in the test data for this project. Studies previously conducted by the AFIT Center for Directed Energy show that polarization has little effect on HELEEOS outputs for lasers below 12 *km* of altitude, as shown in Figure 2. This is because the dominant scattering mechanism at lower altitudes is aerosol scattering, which does not induce polarization [11].

The frequency dependence of Rayleigh scattering means that high-frequency light is scattered most strongly. This effect is responsible for the blue color of the sky, since blue light is scattered more strongly than red. The frequency dependence also means that Rayleigh scattering plays a minimal role for wavelengths greater than 1 μm .

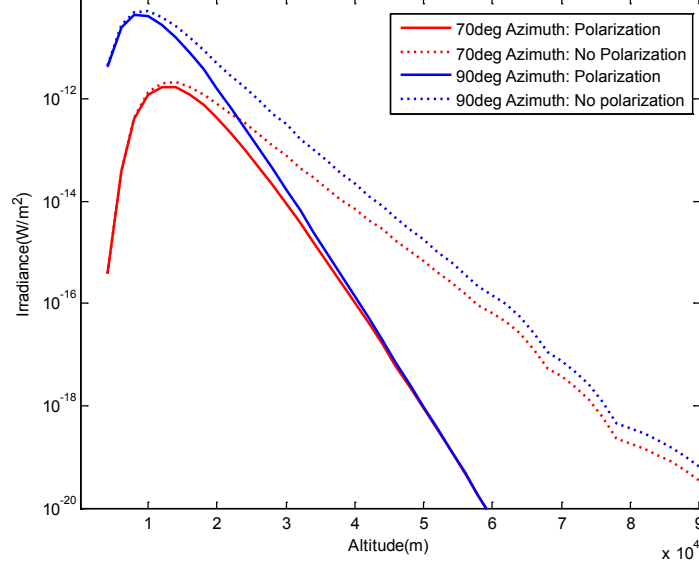


Figure 2. Effect of polarization on HELEEOS off-axis irradiance outputs. Although polarization can make large differences at high altitudes, it has little effect below 1,200 km.

Mie scattering. Aerosol scattering is the most important factor for lasers operating in the troposphere (which is the case for all the planned validation tests) [10]. Aerosols are small particles in the air which can include dust, salt grains, and water droplets. Rayleigh scattering ignores the geometry of the scatterers and treats them as point particles, but this assumption is invalid for scatterers whose size is on the order of the laser wavelength or larger. Therefore the Mie model is instead used for these particles.

The attenuation cross-section σ for Mie scattering is given by

$$\sigma = K\pi a^2, \quad (8)$$

where K is called the attenuation factor and a is the radius of the scattering particle. In general K may include both an attenuation term and a scattering term, and depends on both wavelength and the radius a :

$$K(a, \lambda) = K_{scat}(a, \lambda) + K_{abs}(a, \lambda). \quad (9)$$

K_{scat} and K_{abs} are also called absorption and scattering efficiencies.

The presence of both absorption and scattering terms in K presents a challenge, particularly in the infrared where the molecular absorption coefficients can be significant. This is further complicated by the fact that the particle sizes may vary, and normally there are multiple particle sizes present. In order to determine the Mie attenuation coefficient it is then necessary to obtain a particle size distribution and integrate that distribution over the various radii [18]:

$$\beta(\lambda) = \pi \int_{a_1}^{a_2} N(a) K_{scat} a^2 da. \quad (10)$$

Normally the Mie computations are performed using a nondimensional size parameter

$$x \equiv \frac{2\pi a}{\lambda}, \quad (11)$$

so that the results of Mie scattering computations can be compared across wavelengths and the results applied more generally. In the case of $x \ll 1$, the Mie model predicts Rayleigh scattering behavior, in which forward and back scattering are roughly equal. At larger size parameters, forward scattering is stronger, as shown in Figure 3.

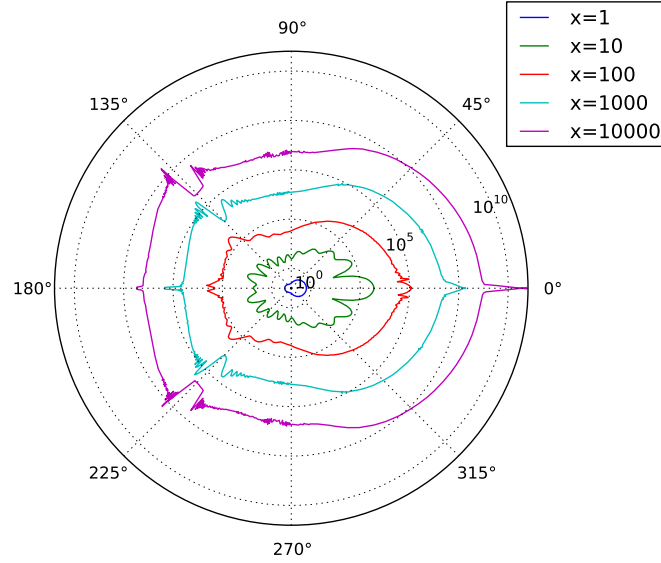


Figure 3. Mie scattering phase functions for various size parameters (based on Figure 12.7 of [14]). The radial axis is a logarithmic scale, and the angles are relative to the direction of propagation. Features of note include the peaks at 0° and 180° , corresponding to forward and back scattering, respectively, as well as the fact that all the phase functions reach their minimum values somewhere around 90° . Finally, it should be noted that the scattered intensity increases with the size of the scattering particles, denoted by the size parameter x .

The Mie model makes the simplifying assumption that all the scatterers are spherical in shape. The spherical particle assumption can introduce significant errors at short wavelengths, but according to Yang et al. the effect of particle nonsphericity is insignificant at thermal infrared wavelengths (8-12 μm) [21]. Although the wavelengths of interest in this study are shorter than that, the assumption may still be relevant because random variations of the orientations and sizes of the particles cause the errors to average out [11]. The HELEEOS model therefore uses Mie scattering exclusively to simulate atmospheric scattering. The phase function used for HELEEOS runs in this thesis is shown in Figure 4; this phase function is computed within HELEEOS using an implementation of the Wiscombe Mie algorithm [10], a technique published in 1980 which provides superior performance compared to previous methods of computing Mie scattering phase functions [19].

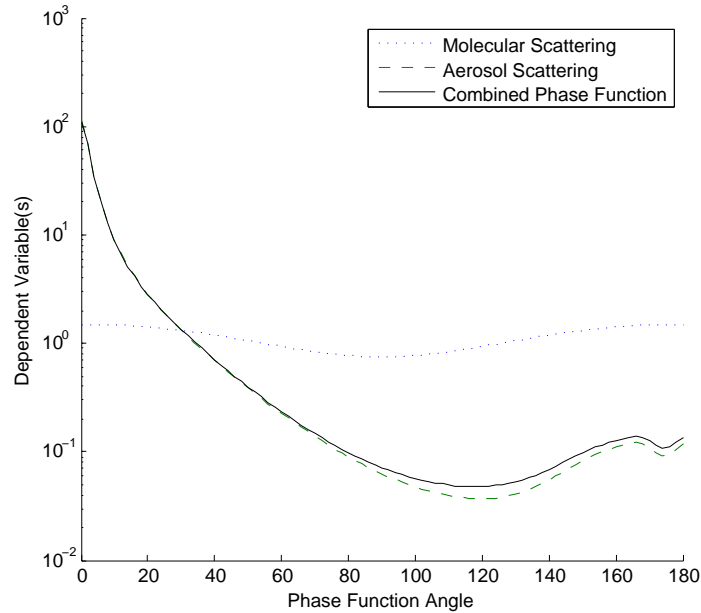


Figure 4. Mie scattering phase functions used in HELEEOS. Both phase functions are computed from the Wiscombe Mie module, but with different size parameters. Note that aerosol scattering dominates; this is because the Mie model predicts stronger scattering for larger particles.

2.1.3 Optical turbulence.

Optical turbulence is caused by random localized temperature variations in the air, which affect the index of refraction and thus distort the shape of the beam, causing it to be wider over a time average than it would be in a vacuum. Small pockets of turbulence (smaller than the beam diameter) can also cause intensity fluctuations, or scintillation, in the beam [18]. Optical turbulence is an important factor influencing laser beam quality and spread, but it is of less importance for off-axis scattering. The broadened beam will impose lower irradiances on the scattering particles in the air, but no loss will result when one looks at the entire beam as a whole.

2.2 Infrared detection

2.2.1 InGaAs detector properties.

The data used in this thesis were collected using an infrared camera containing an indium-gallium-arsenide (InGaAs) focal plane array. An InGaAs array benefits from a low dark current and high quantum efficiency. In addition to cameras, InGaAs detectors are often used for fiber-optic communication.

InGaAs arrays are popular infrared detectors because of their wide bandwidth. InGaAs detectors have a response range from 0.5 to 1.7 μm , with the strongest response between 1.2 and 1.5 μm , as shown in Figure 5 [9]. This overall response range overlaps well with the 1.5-1.6 μm wavelength range of the lasers in question.

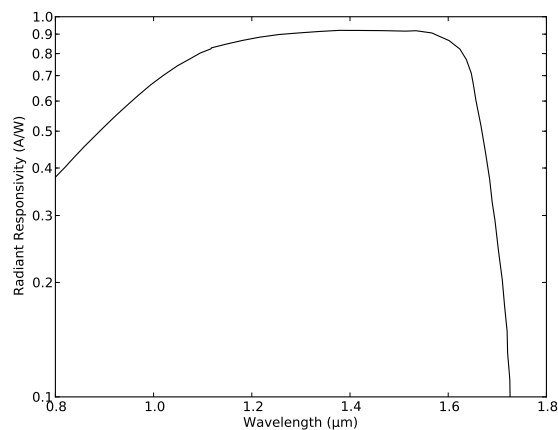


Figure 5. Responsivity spectrum for a typical InGaAs detector at 25°C with a 5V bias. Based on Figure 7.55 in [9].

2.2.2 CCD detector properties.

The data from the December 2009 test were collected using a charge-coupled device (CCD), which employs an array of silicon photodiodes. Silicon detects radiation between 0.2 and 1.15 μm , with the best response between 0.6 and 0.8 μm , as shown

in Figure 6. Because this overlaps well with the the response range of human eyesight, the silicon photodiode is the most commonly used type of photovoltaic detector [9].

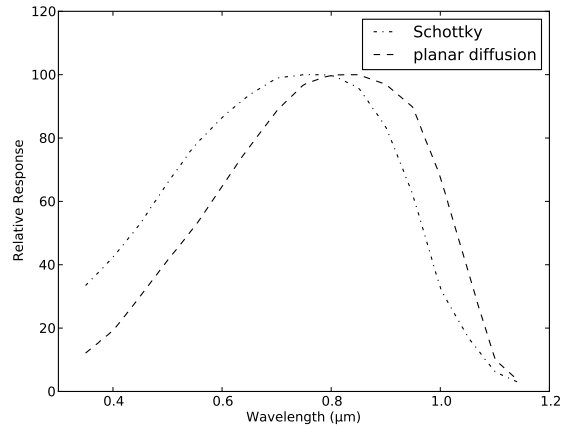


Figure 6. Relative response spectra for CCD detectors. Based on Figure 7.30 in [9].

Silicon’s spectral response would make it unsuitable for the July 2009 test, but silicon does respond at the shorter $1.05 \mu m$ wavelength of the laser used in the December 2009 test. Therefore, although it is less suitable for infrared detection than an InGaAs array, the CCD is capable of detecting the radiation of interest for in the case of the December test.

2.3 Gaussian process regression

Gaussian process regression is a technique for “machine learning,” a process of mapping some set of input parameters to an output parameter. A machine learning process takes a set of input data with corresponding output data (the “training” data set) and produces a numerical function which maps the inputs to the outputs, attempting to smooth out noise such that the function will work for other inputs besides those used in the training set [15].

A machine learning process should fit the training data with reasonable accuracy,

but not so well that noise in the training data influences the training data too much. If the fit is too good, the model may be unstable, meaning that it works excellently for the training data but poorly for any new (or “test”) data with which it is used.

A simple example of machine learning is linear regression, in which the mapping function is simply the sum of one or more known functions, which are scaled by coefficients. This approach is relatively simple and its output easy to interpret. It affords the implementor tight control over basis functions, which is desirable when the physics of the system to be modeled is well known. The linear model cannot, however, model systems involving complex interactions between input parameters. One can always improve the quality of the fit to the input data by increasing the number and variety of basis functions, but this can lead to over-fitting if one is not careful.

More complex systems that cannot be modeled by linear regression are sometimes modeled using neural networks. Neural networks are more flexible than the linear models, but they are in some respects *too* flexible. Neural networks offer a wide range of choices for the implementor in terms of design parameters, and no straightforward framework yet exists to aid in such decisions [15]. As with linear models, the high degree of flexibility can lead to overfitting if one is not careful [12].

Gaussian process regression offers an alternative which is more flexible than the linear models but provides a rigorous approach to avoiding an over-fit of the training data. It can work with a large (even infinite) set of basis functions, while maintaining the stability of the model by computing a characteristic length scale. The characteristic length scale is a measure of how far one can move through the input data set before seeing a significant change in the output [15].

In the HELEEOS off-axis scattering model, Gaussian process regression will be used to create a model that predicts the laser power for a given off-axis observation

scenario. A training data set will initially be produced by running the existing off-axis scattering model with various input parameters. After more experimental data are available, they will be used to form a new training data set.

2.4 Laser communications

Although they are not a predominant means of communication today, lasers are of interest for their high bandwidth, security, and freedom from radio interference difficulties [13, 4]. The line-of-sight nature of laser beams means that data carried through them will not interfere with radio communications, and as a result laser communications are not currently regulated by the FCC [4]. Since nearly all the transmitted power is directed at the intended receiver, it is possible to obtain a desired signal strength at the receiver's end using a much smaller, lighter, and less powerful transmitter [13]. For military applications, the line-of-sight restriction means that laser communications are more secure than radio communications because they are more difficult to intercept [13].

The particular lasers used for the test cases in this study were designed for use in laser communications, and operated at power levels of 0.6 to 5.7 watts. Thus the data already demonstrates the possibility of detecting the use of laser communications systems. Depending on the manner in which laser communications were transmitted, it might also be possible to decipher some of the transmitted data. Barring that, software such as HELEEOS could be used to glean information on the communications system itself, such as its operating power. Doing so requires that the camera observing the laser operations be carefully calibrated. The following chapter describes the theory required to calibrate the camera, and to use the calibration result to compute a single irradiance value for an image.

III. Theory

In order to convert the raw camera data into irradiances which could be compared with HELEEOS, the camera had to be calibrated against a known radiation source, in this case a blackbody whose spectral radiance is described by Planck theory. Radiometric theory allows this radiance to be converted into the power received at the camera's aperture as long as the aperture size, the distance and direction from the blackbody to the camera, and the camera's field of view are all known.

Once the calibration has been applied to images taken in the field, geometric conversions must be made in order to determine the distance along the laser beam path that corresponds to each pixel. In order to accomplish this, the angle between the laser beam and a line from laser source to the observer, referred to as the off-axis angle, must be known. Once this is done, the irradiances computed from the camera can then be compared with irradiance values from HELEEOS in a meaningful way.

3.1 Camera Calibration

In order to convert the digital outputs from the camera into irradiances, the camera must be calibrated against a known radiation source, and a blackbody was chosen for this purpose. The radiance of the blackbody at a particular temperature and wavelength is given by the Planck radiation law as[6]

$$L_{\lambda} = \frac{2hc^2}{\lambda^5} \frac{1}{\exp\left(\frac{hc}{\lambda kT}\right) - 1}. \quad (12)$$

The form of the Planck formula given here is the spectral (wavelength dependent) form. Strictly speaking, photodetectors such as an InGaAs array respond to photons rather than energy. That is, a single photon will liberate one electron if it is sufficiently energetic, and the energy of individual photons is immaterial as long as it is above

that threshold. Therefore, it would be more correct to use the photon count form of the Planck law, rather than the radiant flux form used here. However, for a narrow wavelength range the two equations produce essentially the same result. The July 2009 measurements and the corresponding calibration were conducted using a filter with sufficiently narrow band that the energy form of the Planck equation may be safely substituted for the photon count form. The energy form was chosen over the photon count form because it produces outputs in the form of an irradiance rather than a photon flux, so that the units are the same as the output from HELEEOS.

The radiance L is related to the exitance M by

$$M = \frac{\partial \phi}{\partial A_s} = \int_{\Omega_d} L \cos \theta_s \partial \Omega_d. \quad (13)$$

For a blackbody, the radiance L is independent of the direction of Ω_d . A radiation source having this property is called a Lambertian radiator. For a planar Lambertian source, the relation simplifies to [9]

$$\begin{aligned} M &= \int_{\Omega_d} L \cos \theta_s \partial \Omega_d \\ &= \int_0^{2\pi} d\phi \int_0^{\frac{\pi}{2}} L \cos \theta_s \sin \theta_s d\theta_s \\ &= 2\pi L \frac{1}{2} = \pi L. \end{aligned} \quad (14)$$

Ultimately the goal is to find the power ϕ received at the aperture, which is related to the radiance L by

$$L = \frac{d^2 \phi}{dA_{\text{proj}} d\Omega_d}, \quad (15)$$

where dA_{proj} is an area element of the emitting surface projected into a plane perpen-

dicular to the line of transmission. $dA_{\text{proj}} = dA_s \cos \theta_s$ where dA_s is the area of the emitting surface and θ_s is the angle between the line of transmission and the normal to the emitting surface, and $d\Omega_d$ is the solid angle subtended by the camera aperture as viewed from the surface element in question, and whose value is given by

$$\Omega = \frac{a}{r^2}, \quad (16)$$

where a is the surface area of the aperture and r is the distance from the emitting surface element to the aperture. Solving equation 15 for $d^2\phi$ and integrating yields

$$\phi = \int \int L dA_{\text{proj}} d\Omega. \quad (17)$$

In the calibration tests, the blackbody has an angular extent of $\pm 3^\circ$ from the vantage point of the camera, so by a small angle approximation $dA_{\text{proj}} \approx dA$. [16] Similarly the solid angle Ω can be treated with a constant radius $r = 600\text{cm}$. Thus equation 17 simplifies to

$$\phi = LA\Omega \quad (18)$$

in the small-angle approximation.

To further verify that this small-angle approximation is valid, the full integral of equation 17 can be performed numerically. For the square planar blackbody in question, this becomes

$$\phi = L \int_{-w}^w \int_{-w}^w \cos \theta \Omega dx dy \quad (19)$$

where

$$\cos \theta = \frac{r}{\sqrt{x^2 + y^2 + r^2}} \quad (20)$$

and

$$\Omega = \frac{a}{x^2 + y^2 + r^2}, \quad (21)$$

so that the integral to be evaluated is

$$\phi = L \int_{-w}^w \int_{-w}^w \frac{ar}{(x^2 + y^2 + r^2)^{\frac{3}{2}}} dx dy. \quad (22)$$

Using the values of $a = \frac{10.1^2}{4}\pi \text{ cm}$, $r = 600 \text{ cm}$, and $w = 15.24 \text{ cm}$, the integral 22 evaluates to $\phi = 0.206624L$, while the small-angle approximation of equation 18 evaluates to $\phi = 0.206757L$. Thus the small-angle approximation introduces an error of about 0.06%. Note that this numeric integral still uses a small-angle approximation for the evaluation of Ω inside the integral; this introduces an additional error but this error will be smaller than 0.06% since the aperture of the telescope is smaller than the width of the blackbody. Therefore the total error caused by the small angle approximation is likely to be at most 0.1%.

The radiant flux (or power) is multiplied by the integration time (a parameter controlled by the camera operator) to obtain a radiant energy Q . This can then be divided by the total number of pixels in the array to obtain a radiant energy received per pixel.

3.2 Experiment geometry calculations

In analyzing the data, it will be necessary to relate pixels in the scene to physical locations in the experiment. In order to do this, the geometry relevant to each pixel is considered relative to the source and observer as shown in Figure 7. The location

of a pixel along the laser beam path is described relative to the source in the form of the distance BD, and relative to the observer in terms of the angle a , called the observer angle. In order to determine the distance BD from the angle a , or vice versa, the off-axis angle b and the distance AB must be known.

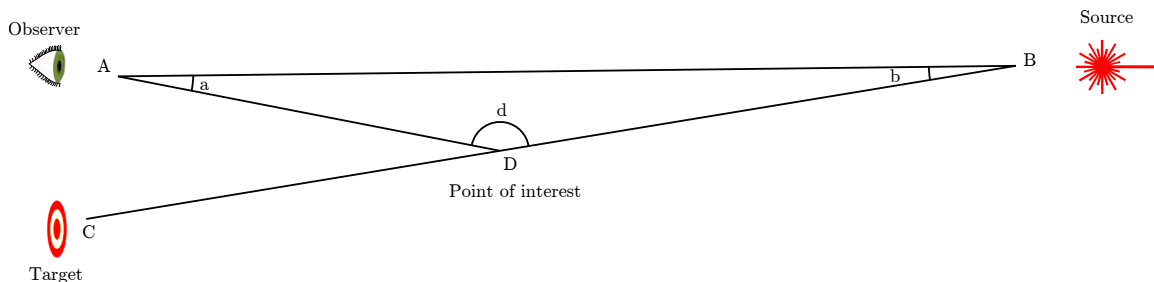


Figure 7. Experiment setup with a triangle shown between the observer, source, and a point of interest along the laser beam path.

3.2.1 Determining the off-axis angle.

Due to the extreme distances involved, it is seldom possible to measure the off-axis angle b directly. Instead, the angle must be determined from the distances between source, observer, and target. The angle is then given by the Law of Cosines as

$$b = \frac{(BC)^2 + (AB)^2 - (AC)^2}{2(AB)(BC)}, \quad (23)$$

where BC is the distance from the source to the target, AB is the distance from the source to the observer, and AC is the distance from the observer to the target, relating to the points A, B, C, and D in Figure 7.

3.2.2 Entering observer geometry into HELEEOS.

The distance AB and the angle b are entered into the observer geometry tab of HELEEOS, shown in Figure 8. The distance AB is entered into the “Initial Distance from Platform (m)” field. In the scenarios used here, the azimuth from the Platform

to the Target was set to 90° , so the off-axis angle b is not entered directly, but rather $90 - b$ is entered into the Relative Azimuth from Platform field. In practice this data entry process was automated by a script.

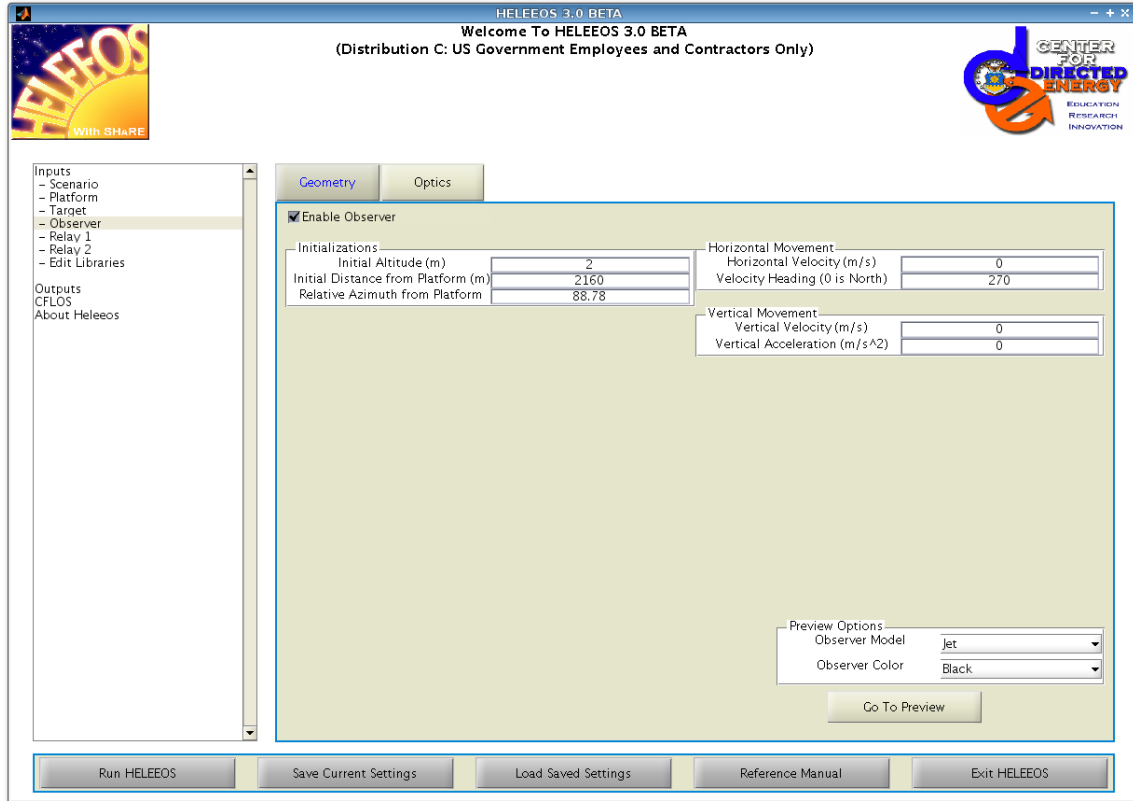


Figure 8. HELEEOS observer geometry settings. The settings in the Initializations section are changed according to the location of the observer.

3.2.3 Locating a pixel position along the beam.

The HELEEOS off-axis scattering model requires a specific point or range of points along the length of the beam at which to compute the scattering toward the observer. In order to obtain verifiable output, this range of points must be matched to pixels in the camera image.

Figure 7 shows the experiment setup showing the observer (labeled A) the beam source (labeled B), the target (labeled C) and some point of interest along the beam

(labeled D). We can obtain the distance BD using the Law of Sines and solving the resulting system to obtain

$$BD = \frac{(AB) \sin a}{\sin d}. \quad (24)$$

We can obtain the angle b from the locations of A, B, and C, and the angle a can be obtained directly from the images as long as the source is visible in the image in question. The d is then simply the difference $\pi - a - b$. The distance AB can be determined from the locations but laser rangefinder measurements are also available.

In practice, it may be more convenient to pick the distance BD and compute the angle at A from it. Again by the Law of Sines:

$$\sin a = \frac{(BD) \sin b}{(AD)}, \quad (25)$$

where the distance AD can be found using the Law of Cosines:

$$AD = \sqrt{(AB)^2 + (BD)^2 - 2(AB)(BD) \cos b}. \quad (26)$$

By a small-angle approximation, each pixel in the image represents a fixed angle in the camera's field of view. Using this assumption, the angle a can be measured directly from the image as the number of pixels from the source location to the pixel of interest. In this way, each pixel that is along the laser beam in the image can be related to a specific distance from the source, enabling the irradiance from that pixel to be attributed to scattering that occurred at that distance along the beam.

3.2.4 Relating image irradiances to HELEEOS irradiances.

HELEEOS calculates scattering in a cylindrical region along the beam path, giving aggregate scattering across the entire width of the beam in a range of distances

specified by the user. Pixel values in the image, on the other hand, represent the irradiance produced by all points in their field of view. Figure 9 illustrates this. Typically, a pixel's field of view does not span the entire width of the beam, so the irradiances from multiple pixels must be added together. A single irradiance value can be computed for an image by adding up pixels covering some region of interest, which can then be compared with predictions from HELEEOS. The implementation of this process will be discussed in more detail in the next chapter.

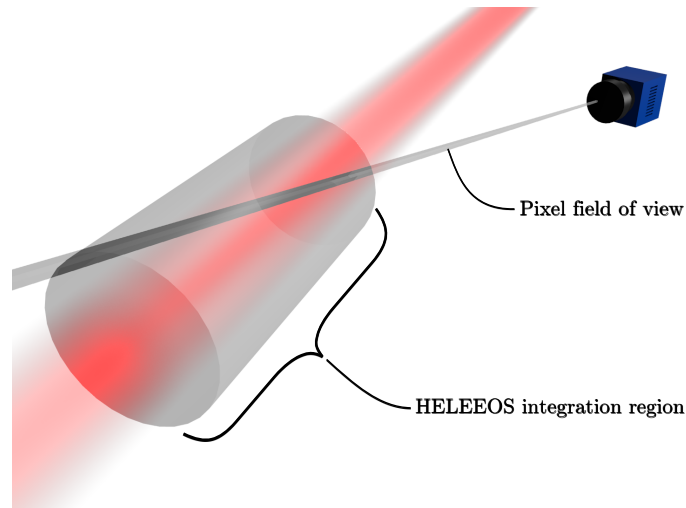


Figure 9. HELEEOS computes the total irradiance from a cylindrical length of the beam, while each pixel of an image records the total irradiance scattered from points in its field of view. To compare the two, irradiances from multiple pixels must be combined such that they contain the cylindrical region being integrated in HELEEOS.

IV. Analysis Process

Before analyzing the field images, the camera had to be calibrated against a known radiation source, in this case a blackbody. This calibration process cleans up the images, but more importantly it converts the arbitrary units of the camera into physical units of energy. The process also revealed some quirks of the camera, and provided a means to quantify some of the uncertainties in the final result.

4.1 Camera calibration

The camera, a XenICs Xeva 409, was calibrated against a CI Systems SR80-12HT blackbody at a variety of temperatures between 200 and 500 °C, with the camera placed at a distance of 600 cm [16]. During both the calibration and the field data collection, the camera's cooling temperature was set to 200 K. The camera viewed the blackbody through a telescope having a 10.1 cm aperture, the smaller of the two telescopes used in field observations. A band-pass filter was placed in front of the telescope, which has a pass band extending from 1.49 μm to 1.62 μm . The field of view of telescope-camera combination was sufficiently small that the 12-inch blackbody over-filled the detector's field of view. Were the detector not over-filled, a more complicated calibration process would be required.

The larger of the two telescopes, a reflecting telescope with a 31.75 cm aperture, needed to be much farther away from its target in order to focus, and adequate space was not available in the laboratory. Therefore the calibration of the smaller telescope had to be applied to the larger telescope as well. This was possible to do because the same camera was moved back and forth between the two telescopes. The process by which the calibration results were applied to the larger telescope is discussed in Section 4.1.2.1. Both telescopes and the camera are shown in Figure 10.

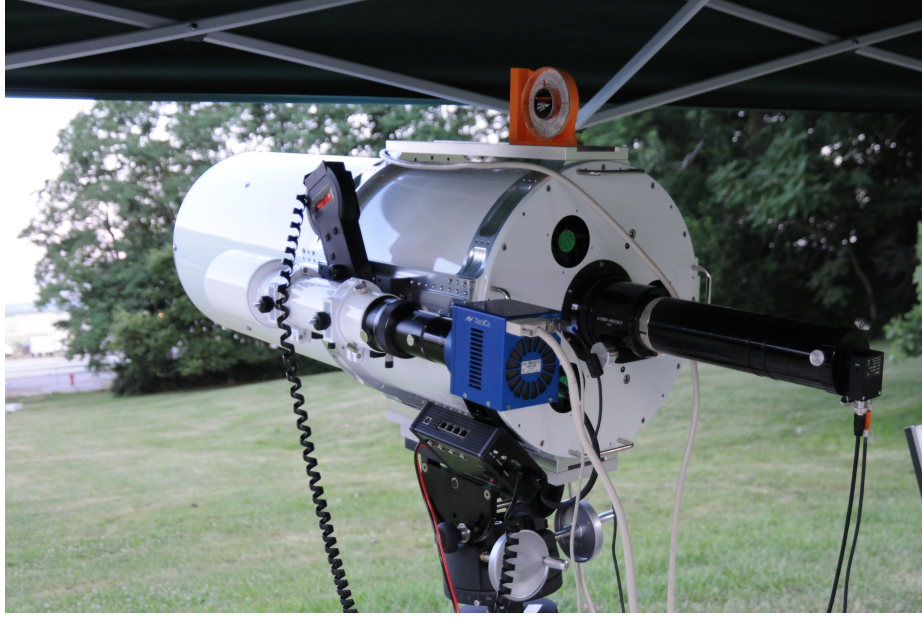


Figure 10. The telescopes and camera used for the field data collection. The 10.10 cm refracting telescope can be seen attached to the side of the larger 31.75 cm reflecting telescope, with the camera (the blue cube) attached to the back of the smaller telescope.

4.1.1 Analysis of the calibration data.

This section discusses the process of analyzing the blackbody images. A software application was developed to assist with this analysis and to apply the calibration results to images taken in the field. This program is documented in Appendix A.

4.1.1.1 Spatial calibration.

The first blackbody images were taken with a mask placed over the blackbody. This mask provided a means to focus the camera, as well as to perform a spatial calibration. The mask consisted of a foam-core board with holes cut in it so that the blackbody could be viewed through the holes. Examples of these images are shown in Figure 11. The dimensions of the holes were measured in physical space with a ruler, as well as in image space. The quotient of the physical extent of a hole divided by the 600-cm distance between the camera and the blackbody, using a small-angle

approximation, is equal to the angular extent of the hole. The ratio of this angle to the hole's extent in pixels, the per-pixel field of view of the camera, provides a mapping of dimensions in image space to physical dimensions of the subject being imaged.

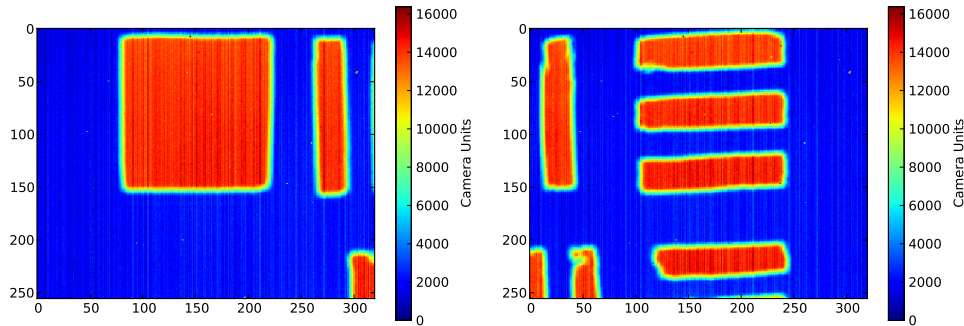


Figure 11. Blackbody images taken with a mask over the blackbody, used for spatial calibration.

4.1.1.2 Selecting blackbody images.

Of the 254 blackbody images taken, only 162 were used to compute the final calibration. Of those discarded, a handful had been taken with a mask in front of the blackbody in order to facilitate spatial calibration as discussed in the previous section, but most were either overexposed, underexposed, or otherwise flawed. This section describes the process by which suitable blackbody images were selected.

Histograms of the blackbody images provided one means of assessing the quality of a histogram. Since the scene in front of the camera is mostly a constant flux with a few perturbations added to it, a good histogram of a blackbody looks roughly Gaussian. Before calibration, variations in the detector properties over the surface of the focal-plane array (the part of the camera that detects incident photons) widen the Gaussian distribution, but a good blackbody image will retain a Gaussian appearance both before and after calibration. Truncation of the Gaussian shape is an indication of

a large number of over-exposed or under-exposed pixels, so images having a truncated Gaussian distribution were excluded from the calibration. Examples of these are shown in Figure 12.

One common cause of overexposure or underexposure is the use of an integration time that is too high or too low. Integration time is equivalent to exposure time in film photography, so a longer integration time allows more photons to enter the detector. Setting too high an integration time will overexpose the image, while a low integration time can underexpose the image.

One would expect the camera output to vary linearly with integration time, but this was not the case, as seen in Figure 13. The camera's output is a linear function of integration time between about 3000 and 10000 μs , and a small region of linearity (albeit off-set from the first) can be seen between 2000 and 2500 μs . Between 2500 and 3000 μs , however, the camera outputs varies erratically, with several points at which the camera outputs zeros throughout the image. Some of the large variations in camera output shown in Figure 13 occurred after changing the integration time by only 1 μs , and did so instantly when the setting is changed. The erratic outputs did not fluctuate substantially with time (fluctuations over time appeared no larger than were observed for outputs in the linear region). Furthermore, the erratic outputs appeared to be repeatable, such that when one observed an output at a given integration time, changed the integration time and then changed it back, the output appeared the same as was previously observed at the first integration time. Data were not collected to substantiate this observation about repeatability, but the abrupt changes in output as the integration time was changed, combined with the repeatability of these erratic values, suggest that the behavior was a quirk of the camera as opposed to the experimental setup.

Images for which the output varied significantly from linearity were discarded and

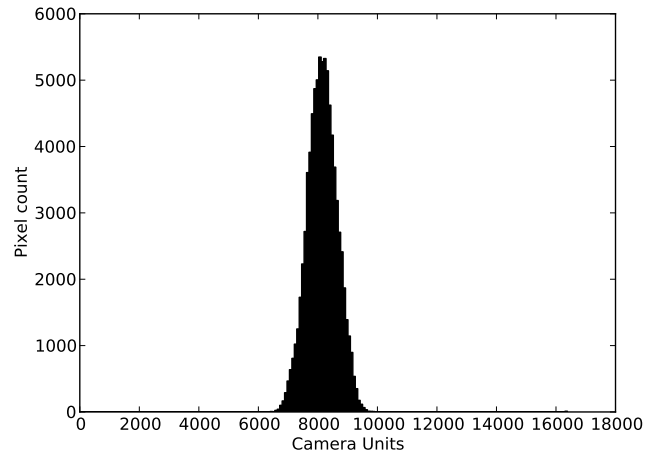
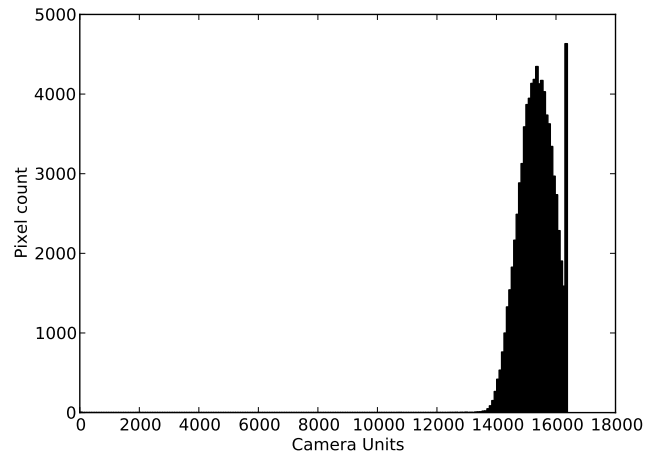
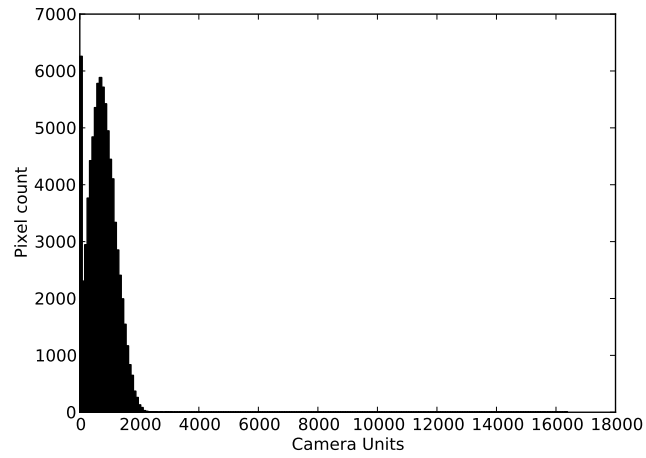


Figure 12. Histograms of raw camera data. Top: Histogram of an image with many underexposed pixels. Middle: Histogram of an image with many overexposed pixels. Bottom: A good histogram.

not used in the calibration. The calibration process assumed linearity throughout and did not account for the offset between the two linear regions seen in Figure 13, but the error introduced by this assumption was captured by the error analysis process described in Section 4.4.

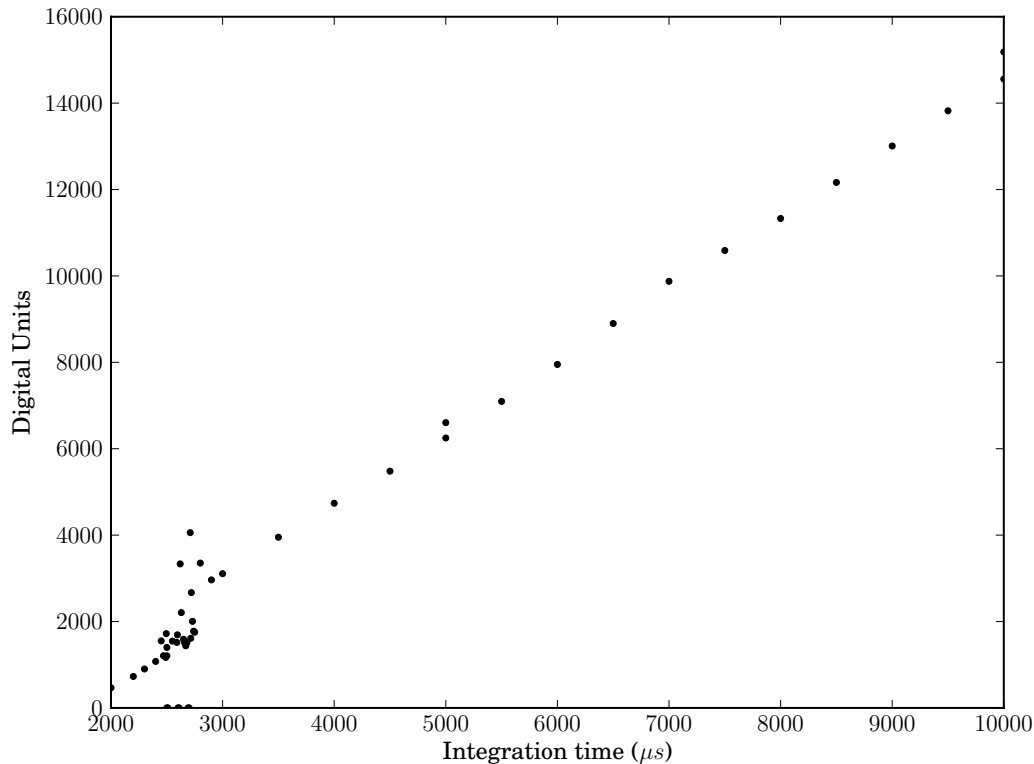


Figure 13. Camera response versus integration time for a 300 C blackbody. Note the erratic behavior between 2000 and 3000 μs . This image shows data for the pixel at (91,118), but other pixels behave similarly.

A number of blackbody images showed artifacts of unknown origin, most commonly horizontal bands across the image. These images were nearly always outliers when the camera output was plotted against integration time and so were discarded. Examples of these are shown in Figure 14. Some of the blackbody images, particularly those for the higher temperatures, contained fluctuations caused by hot air

convecting upward in front of the blackbody. These images were used, and the effects of convection mitigated by time-averaging the data before performing the regression.

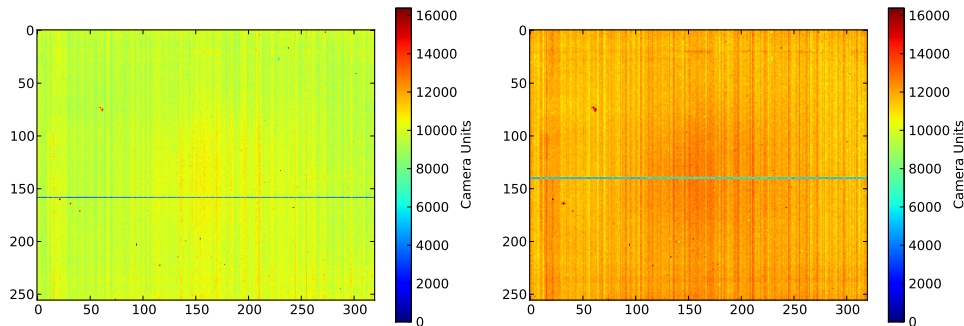


Figure 14. Blackbody images showing banding artifacts.

4.1.1.3 Computing the calibration.

The calibration was computed by performing multiple linear regression, where the pixel values from the camera served as the independent variable and the per-pixel energies served as the dependent variable. The per-pixel energies were calculated using the Planck radiation law for the respective blackbody temperatures and integration times. By using linear regression, gain and offset arrays could be computed that provided a best fit for all the blackbody images.

Planck integration. Since the camera has a fairly broad wavelength range, a bandpass filter was used to reduce the bandwidth detected. To obtain the radiant power output of the blackbody at each temperature, the spectral emissivity given by the Planck theory (Equations 12 and 14) was integrated over the bandwidth of the filter. The Planck emissivity curves are shown in Figure 15. The emissivities of the various curves in Figure 15 span several orders of magnitude. With these temperatures, and the wide variety of integration times used, the calibration spanned the entire dynamic range of the camera.

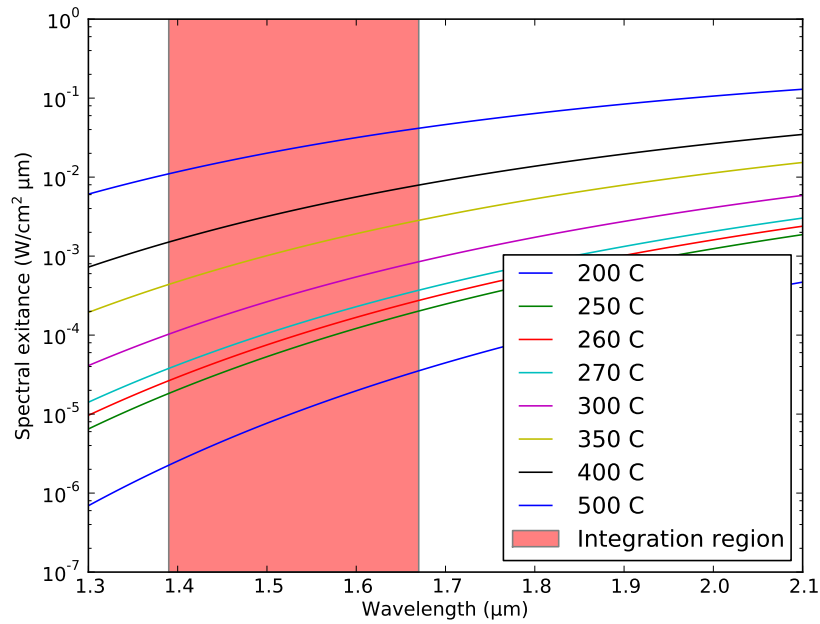


Figure 15. Planck emissivity curves for the various blackbody temperatures.

To better capture the filter’s transmittance, the spectral radiance was multiplied by the filter’s spectral transmittance at each wavelength. Since the actual transmittance was integrated along with the spectrum, the integration was extended well into the tails of the filter spectrum, as shown in Figure 16. For the upper limit, the integration was cut off at $1.67 \mu m$, the point at which an InGaAs camera’s responsivity falls off by 50% according to the responsivity curve in Figure 5. This is consistent with the manufacturer’s advertisement that the camera’s spectral band extends to $1.7 \mu m$ [20].¹ Since both 1.67 and $1.7 \mu m$ are in the tail of the filter spectrum, the difference between 1.67 and $1.7 \mu m$ will probably not change the calibration results to a large degree.

¹The Xeva 409 camera is no longer sold and a specification sheet was not available; the source cited here is the specification sheet for the currently manufactured XS-1.7-320, which is believed to be a nearly identical product.

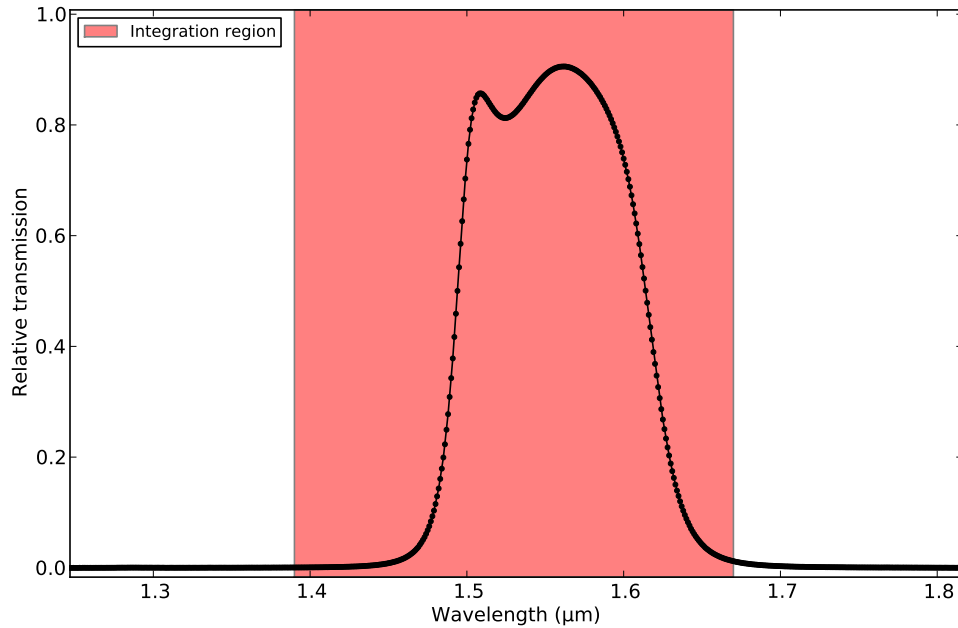


Figure 16. The transmittance spectrum of the filter.

Handling bad pixels. A handful of pixels produced the same numerical value regardless of the input energy, and for these pixels the regression model failed. These were identified as “bad” pixels and their coordinates stored in an array.

Once the regression was completed, it could then be applied to the blackbody images used in the calibration. Ideally the calibrated images should consist of randomly varying values with an average near the energy calculated for the corresponding blackbody temperature and integration time. Any pixels deviating far from the average for the image could be presumed to have a significantly nonlinear response and therefore be identified as “bad” pixels. The calibration program provided two methods for handling this. The first method was to automatically identify pixels as bad if their value was more than some user-specified threshold from the image’s mean value; this threshold was expressed as a multiple of the standard deviation so that it could be applied uniformly to all the images in use. The second method (used alone or in com-

bination with the first) was to allow the user to pick pixels to be treated as “bad” and manually add them to the array. In the end, the automatic method proved sufficient and the manual method was not used.

When applying the calibration to an image, the pixel values were multiplied by the computed gain array and then added to the computed offset array. The “bad” pixels were then handled by replacing their values with the average of nearby pixels. Normally this meant simply averaging all the good pixels adjacent to them, but for pixels with no adjacent pixels the program automatically increased the radius until at least one good pixel was available to compute an average.

Once a calibration was computed, it was tested against some of the blackbody images not used in the calibration (those with many over- or under-exposed pixels) to verify that the calibration produced energies near those predicted by Planck theory for the respective blackbody temperatures. Finally, it was tested against images taken in the field to ensure that they appeared qualitatively correct. These last tests provided an additional opportunity to identify “bad” pixels.

4.1.2 Calibration results.

The calibration process revealed some interesting characteristics of the camera. The camera has the characteristic that its output varies nonlinearly (and sometimes erratically) as a function of integration time. Its response increases linearly for a large range of integration times, but with a few notable exceptions, particularly between 2500 and 3000 μs , as shown in Figure 13. These nonlinearities appear in an identical fashion when the camera integration time is manipulated up or down; this repeatability suggests that they are a quirk of the camera rather than a consequence of the experimental set-up. Images taken using integration times within the range of linear response should be unaffected by these problems.

Once the bad integration times are removed from the data set, Planck theory can be used to compute the energy expected for each blackbody temperature, as shown in Figure 17. The results show a weak linear trend overall, but the points associated with each blackbody temperature are grouped in lines, and the points spread along these lines considerably according to their respective integration times. Clearly some significant factor has not yet been accounted for here.

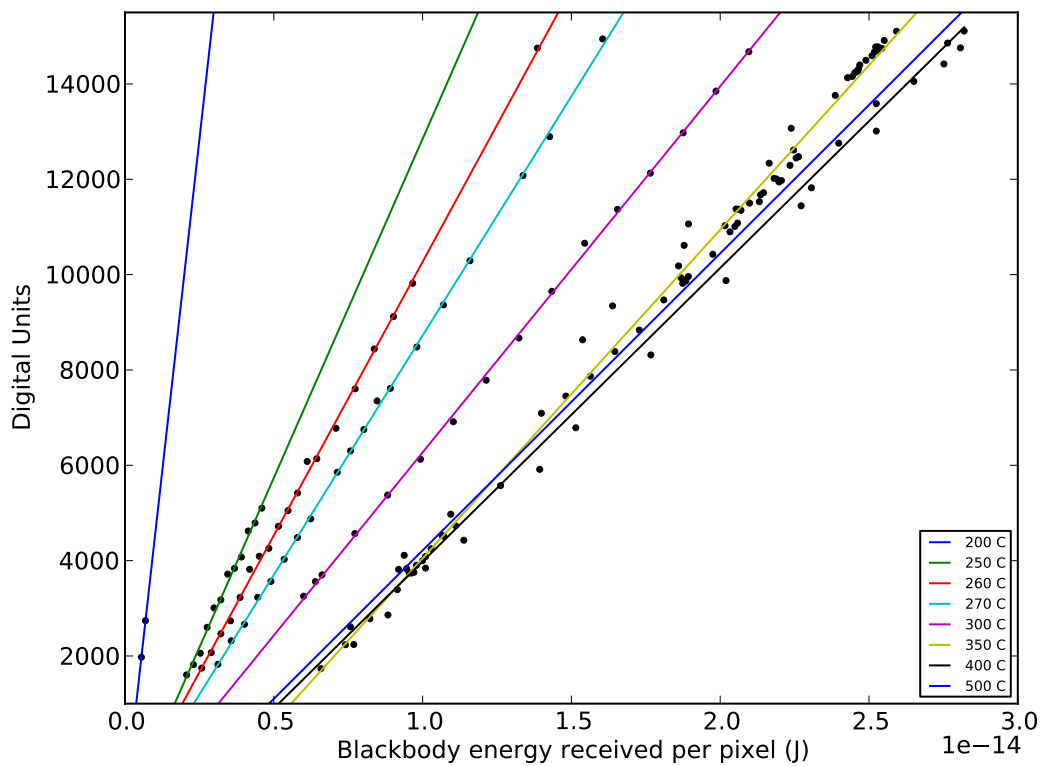


Figure 17. Camera response versus energy received for various blackbody temperatures and integration times. Linear fits are shown for each of the blackbody temperatures for which at least 2 points are available; the positive slope of each line is a result of increasing integration time. The range of integration times used is listed in the legend of Figure 18.

By grouping points according to integration time and performing linear regression on each group, as shown in Figure 18, it is seen that the offset varies with integration

time but the gain changes relatively little. Plotting the offset against the integration time reveals a predominantly linear relationship, as shown in Figure 19. A possible physical explanation for this is that the focal plane array is receiving energy from some other source besides the aperture, and that this energy arrives at a roughly constant rate. This could be caused by ambient radiation entering the aperture at extreme angles and scattering inside the camera body before reaching the focal plane array, or by electrical processes producing currents independently of any radiation source. Since the process is a linear function of integration time, it is possible to remove the effect by linear regression. The dependence of gain on integration time, also shown in Figure 19, would be more difficult to account for, but is fortunately less pronounced.

The plot of offset versus blackbody temperature in Figure 19 reveals no consistent trend, but the plot of gain versus blackbody temperature shows a noticeable decay as temperature increases. Because this effect is related to blackbody temperature, it could be due to some unaccounted for characteristic of the experimental setup and not the camera. On the other hand, the lower blackbody temperature might produce a larger number of photons which are near the edge of the camera's response range (1.7 microns), resulting in a nonlinear response at that temperature.

The calibration program was modified to use multiple regression in order to account for this effect of the integration time. Including the integration time as part of the regression process produces a much better fit, as shown in Figure 20. Additional blackbody images have been included in the plot to verify the stability of the fit. The outlier images in this plot are extreme cases of erratic behavior on the part of the camera or other unusual factors. Each outlier image contains readily visible defects, such as a horizontal line across the center of the image, or a histogram showing a truncated distribution such as those shown in Figure 12. Therefore, the calibration

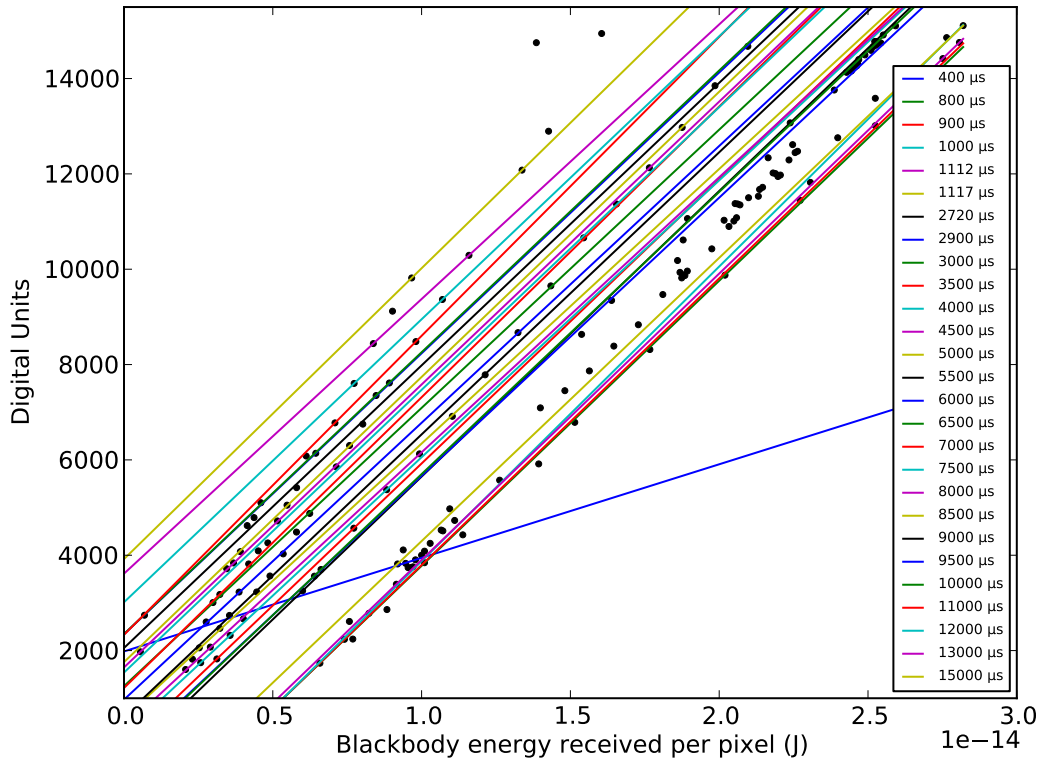


Figure 18. The same data set as seen in Figure 17, with linear fits conducted on groups of points having the same integration time. Most of the lines are parallel, suggesting that the offset varies as a function of integration time but the gain varies very little. The exception to this is an integration time for which only two close-together points were available, resulting the line running across the bottom of the plot.

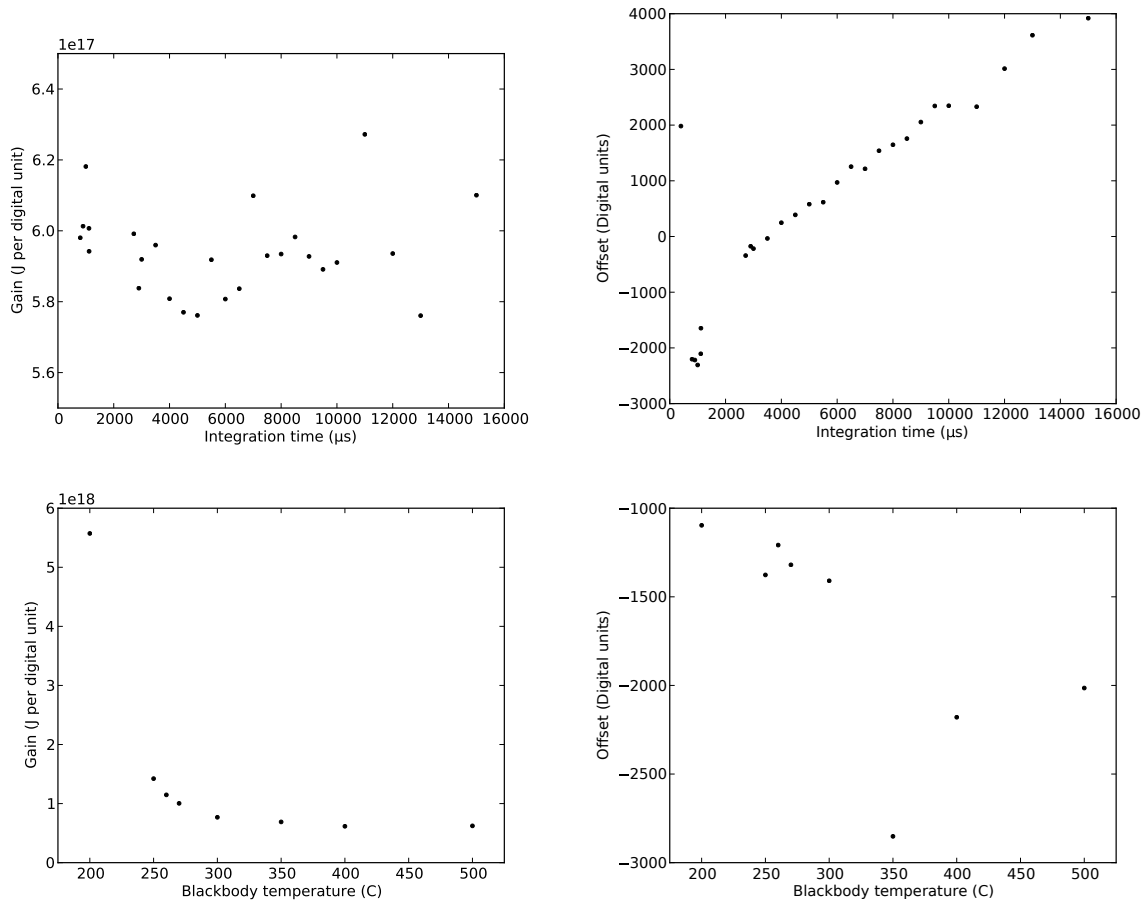


Figure 19. Gain and Offset versus integration time and temperature. The integration time relationship is largely linear beyond $3000 \mu s$ (a larger number of data points below $2500 \mu s$ might reveal a separate linear domain in that region), while the gain shows only weak dependence on integration time. The offset shows no consistent temperature dependence, but the gain shows a nonlinear temperature dependence.

is likely to be reasonably stable when applied to the field images.

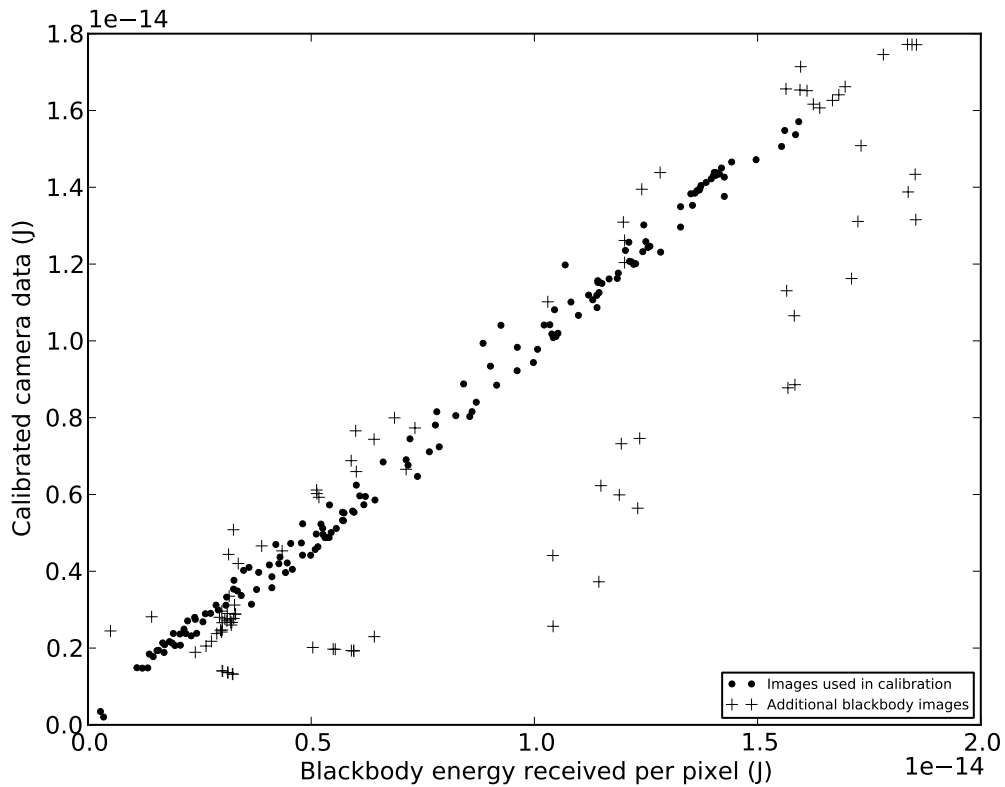


Figure 20. Result of including integration time in the regression process.

Figure 21 shows the calibration result across the focal plane array in the form of four image plots. The most interesting of these is the gain array, which shows a smooth decrease of about 10% from outside to inside. Removing a small-angle approximation from the calibration software did not fix this. According to Greg Smith, however, this particular blackbody exhibits a temperature gradient of about 1.5°C , with the highest temperatures typically toward the center of the blackbody surface. He said that the temperature spread was 1.5°C regardless of the blackbody temperature; it did not increase or decrease substantially when the blackbody was heated. This temperature gradient is a likely cause of the main variation in the gain array. Mr. Smith allowed

the blackbody to sit 15-20 minutes after the thermostat stabilized before making this measurement [17]. Many of the images used in the calibration were taken much sooner after the thermostat stabilized, so the temperature gradient contributing to the spread in the gain array may be larger than 1.5°C. Although the exact temperature gradient was not measured when the images were taken, the errors contributed to the calibration by this gradient can be captured by taking the standard deviation of the gain array, since the temperature gradient appears to have been the dominant source of variation.

Both the gain array and the integration time coefficient array show some interesting streak features near the edges of the images. The cause of these is unknown, but they appear not to be representative of the camera's response in the field, since the same streaking artifacts appear in some of the field images after calibration. These features have magnitudes on the same order of the dark region attributed to the temperature gradient, so the standard deviation of the gain array will also include errors contributed by this effect.

Of the three arrays used to apply the calibration, the offset array is the one that contributes most to the appearance of the output. The vertical lines seen in the offset array are visible in every image produced by the camera, and they go away when the calibration is applied.

The variance array is computed from the residual terms associated with the linear regression. It consists of variances

$$\sigma_{fit} = \frac{1}{N - m} \sum_{img} (y_{img} - \bar{y})^2, \quad (27)$$

where N is the number of images used in the calibration, m is the number of fit parameters (3), y_{img} is the value of that pixel in each blackbody image, and \bar{y} is the value predicted by the calibration for that blackbody image (from its temperature

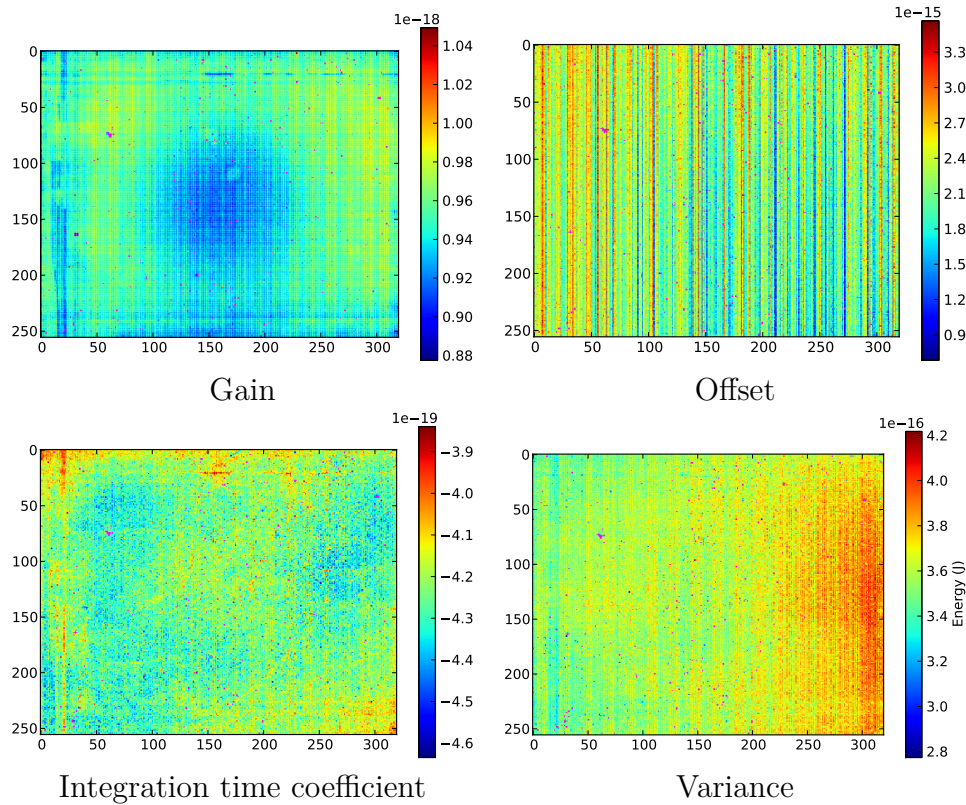


Figure 21. Image plots of the calibration result. Magenta-colored pixels are considered “bad.” The gain array (upper left) characterizes the way the camera output varies as the incoming radiation is increased. The dark region in the middle of the gain array is probably caused by a temperature gradient over the surface of the blackbody (the blackbody tends to be hottest in the middle). The offset array (upper right) represents the camera’s output in the absence of incident radiation; the vertical lines in the offset array are responsible for removing similar features from images taken with the camera. The array of integration time coefficients (lower left) is a correction factor which had to be added to the offset array, probably due to dark currents or stray radiation entering the system. The variance array (lower right) is the sum of the residuals for all of the images; it gives an indication of the errors associated with the linear fit.

and integration time). This is a standard way of quantifying uncertainties for linear regression [5]. Since the regression was performed separately on each pixel, this produces an independent value for each pixel.

4.1.2.1 Applying the calibration data to a different optical setup.

Since the larger telescope could not be used to image the blackbody directly, the calibration data from the small telescope had to be applied to images taken with the large telescope as well. In order to do this, the following assumptions were made:

- Losses due to the optics (from absorption, scattering, transmission through mirrors, reflection off lenses, etc.) are equal in both systems.
- The relative obscuration (the fraction of the field of view that was blocked by optical components such as mirrors) of the smaller telescope is zero.
- The secondary mirror of the large telescope was the only source of obscuration in that system (i.e. the spider and other parts contributed negligibly to the relative obscuration).

Using these assumptions, the calibration could be applied directly to the large telescope, and the only change required was to use the larger telescope's aperture diameter (31.75 *cm*) in converting from energy to irradiance, and to account for the relative obscuration by reducing the aperture area accordingly.

4.2 Background subtraction

In the field, the camera receives light from a variety of sources in the scene, and the laser's contribution to the final image must somehow be separated from everything else. This is done by quantifying the background radiation in the scene

and subtracting it from the calibrated image to find the radiation scattered by the laser.

Many of the scenes consist of animations in which the laser turns on or off. In this case the background can be computed as the average of some of the frames in which the laser is turned off. Subtracting this average from a frame in which the laser is on yields an image in which most pixels have values near zero, except for those containing laser beam scatter.

Unfortunately, the background fluctuates slightly with time, due to variances in solar illumination (due to passing clouds) or other factors. In order to eliminate this bias, a histogram is computed from the image being studied. Since most of the pixels are background pixels, the maximum of the histogram indicates the overall shift in background compared with the previously-computed average. Subtracting this maximum value from the entire image will remove most of the temporal variance in the background.

Much of the background contains noise which cannot be eliminated. After shifting the background, however, the noise has an average value of zero, so that positive noise will, on average, cancel out negative noise when a sum is computed over a region of the image.

4.3 Total irradiance for an image

The calibration process produces an irradiance for each pixel of an image, but HELEEOS produces irradiances for a particular span of the beam length, which is specified as a distance range under “Observer Field of View,” as shown in Figure 22. In order to compare HELEEOS outputs to the measured irradiances in a meaningful way, this distance range must be mapped to a set of pixels in each image. Once the appropriate pixels are selected, the total irradiance for the region can be found

by adding together the irradiances for all the pixels in the region. Ideally this total should be close to the irradiance produced by HELEEOS as long as the distance range and other parameters are consistent.

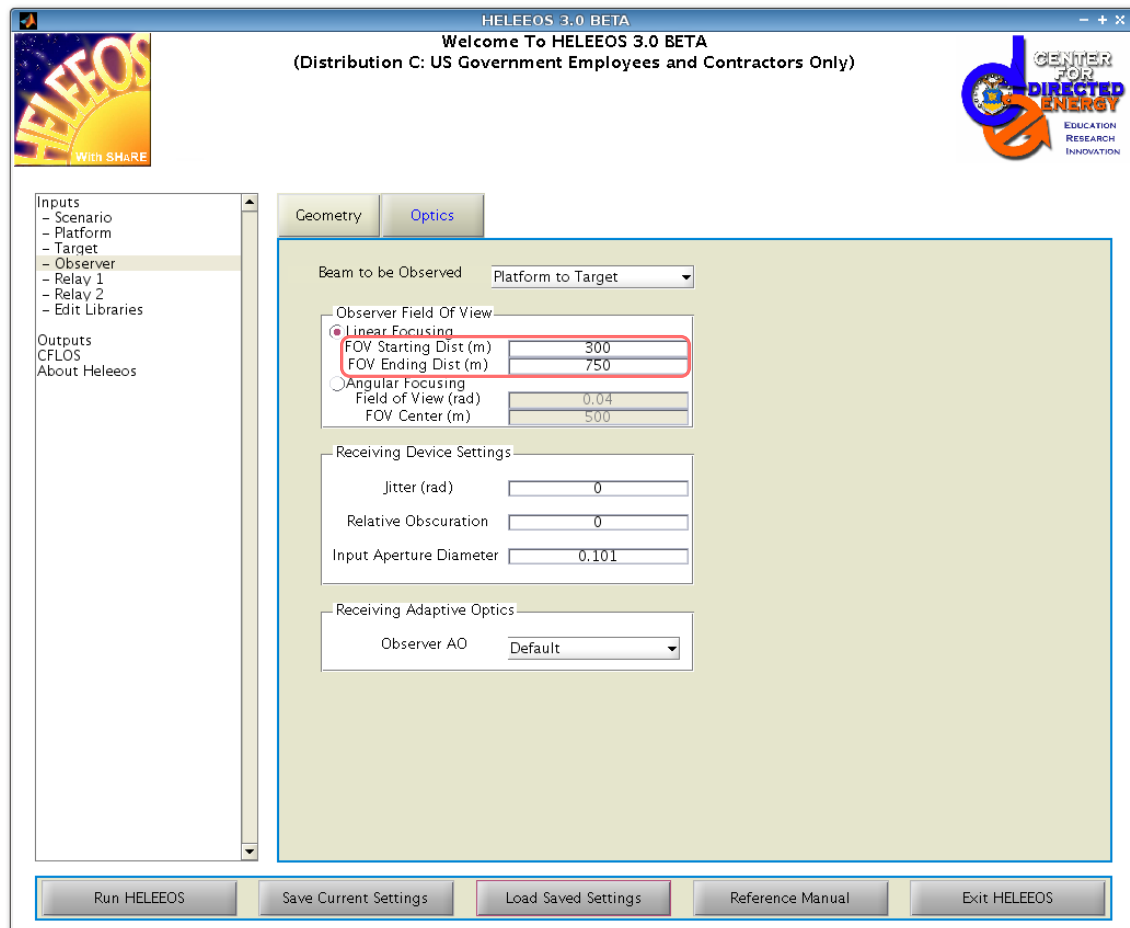


Figure 22. Observer optics settings in HELEEOS. The analysis software maps the distance ranges under “Linear Focusing” (here identified by a red box) to a region of pixels in the image.

For each image, a range of distances along the laser beam is selected. The distances, defined in meters from the laser source, are chosen such that the entire range is visible in the image. This distance range is converted to angles using Equation 25, and these angles are converted to distances in pixels using the per-pixel field of view computed in Section 4.1.1.1.

The selection region is defined in terms of the location of the laser source in the image, the coordinates of which are found manually for each image. The selection region is defined relative to the source, as shown in Figure 23. The parameters are chosen in such a way as to contain the entire beam within the desired distance range. The region is given in terms of an apparent beam direction, θ , which defines the direction of the beam in the image, clockwise from the horizontal direction. The beam's width in the image is defined in terms of a parameter $\Delta\theta$, which specifies a range of angles on either side of the beam's center. The beam's width in the image is defined in terms of a parameter $\Delta\theta$, which specifies a range of angles on either side of the beam's center.

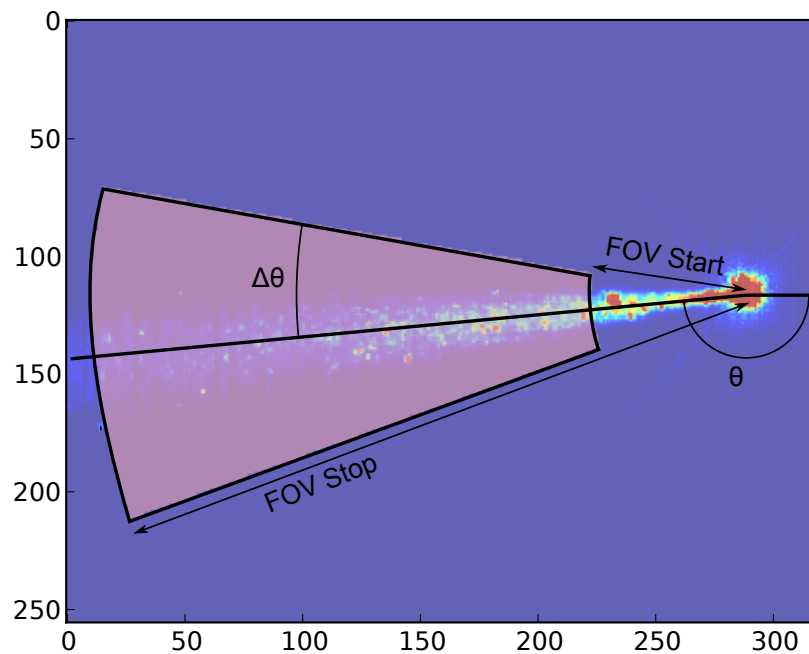


Figure 23. Parameters defining the selection region. All angles and distances are defined relative to the location of the beam source, and were entered manually. The angle θ defines the apparent direction of the beam, clockwise from the horizontal axis. The selection region includes all pixels whose direction from the beam source is between $\theta - \Delta\theta$ and $\theta + \Delta\theta$, and whose distance from the source is FOV Start and FOV Stop. FOV Start and FOV Stop are typically entered in meters (representing distances along the beam from the source), and are converted to angles and pixel ranges in the observer's field of view using Equation 25.

The total irradiance for the image is found by summing the irradiances computed for each pixel within the selected region. This summation is computed for each frame

within a range of interest. The frame range is selected such that the laser(s) are turned on and in a steady state (i.e. they are not in the middle of turning on or off). Sometimes several frame ranges were selected out of the same data set. This was typically the case when the lasers were turned on or off one by one, so that part of the data set showed one laser turned on, another showed two lasers, and perhaps another section showed three lasers. For each frame range, the irradiance reported as the final result was the average of the totals for all the frame, with the standard deviation of those totals being used as an error term.

4.4 Error analysis

Known and quantifiable errors in the analysis include: Random variances in the calibration data, nonuniformity of the blackbody temperature over its surface, non-zero background values that were not removed by background subtraction, and time-varying fluctuations in the irradiance from one frame to another.

Random differences between blackbody images are computed using the expression for σ_{fit} , given in Equation 27. σ_{fit} includes errors due to the blackbody temperature being higher or lower than it was assumed to be, changes in the energy entering the camera due to variations in room lighting, and changes in the state of the camera over the course of the calibration. It also includes errors introduced by the assumption that the camera's response is a linear function of incident energy, which is of course a simplification. The assumption that photon count and energy are equivalent introduced a small amount of error which is captured in σ_{fit} . Errors in measuring the distance between the aperture and the blackbody are also effectively included in σ_{fit} , since the calibration was conducted over the course of three days so this distance was measured several times. Even so, the 600 *cm* distance is considered to be accurate to within 1 *cm*; at 0.2%, this is smaller than most of the other errors being considered.

As mentioned previously, the dark area in the middle of the gain array was caused by a temperature gradient from the center to the edges of the blackbody. In addition, there are horizontal and vertical streaks near the edges of the gain array. The cause of these streaks is unknown, but they may well be caused by errors in the calibration process (such as an additional region of temperature variation on the blackbody surface), rather than an actual variation in gain from one pixel to another. In any case, these streaking features introduce gain variations on the order of those caused by the temperature fluctuations, as evidenced by the fact that both appear blue in Figure 21. Therefore, the standard deviation σ_g of the gain array can be considered to capture the impact of the blackbody temperature variations and other errors upon the gain array.

The temperature displayed on the blackbody thermostat comes from a thermocouple located behind the center of the blackbody surface. The temperature from this thermocouple is certified by the manufacturer to be accurate to within 0.5°C . The manufacturer's acceptance test report lists actual errors measured in testing the blackbody, all of which were considerably smaller than 0.5°C (they ranged from 0.01 to 0.07°C) [7]. Deviations of the blackbody temperature would bias the result, but since the 0.5°C is less than the 1.5°C variation in temperature over the blackbody surface (which has already been quantified), the uncertainty of the thermocouple was not included in the error analysis.

After performing background subtraction, most pixels of the image should have a value near zero, with only a handful containing the signal. Therefore the standard deviation σ_{bg} of all the pixel values in the image (after background subtraction) should be representative of the errors contributed by background subtraction.

Following the standard procedure of summing errors in quadrature to obtain the uncertainty for a summed value, the total uncertainty in the energy Q received at a

pixel is given by

$$\sigma_{Q_{px}} = \sqrt{\sigma_{fit}^2 + \sigma_{bg}^2 + D_{px}^2 \sigma_g^2}, \quad (28)$$

where D_{px} is the value in digital units produced by the camera at the pixel of interest, minus the value of the (un-calibrated) background at that pixel.

The total energy received is found by summing Q over a region of interest. The uncertainties σ_Q are not correlated, so they are summed in quadrature to obtain

$$\sigma_{Q_{img}} = \sqrt{\sum_{px} (\sigma_{Q_{px}})^2}. \quad (29)$$

When the irradiance is computed, this energy is multiplied by a conversion factor to get irradiance as

$$E = \frac{\sum_{px} (Q_{px})}{\frac{\pi d_1^2}{4} t_{int} (1 - C)}, \quad (30)$$

where d is the aperture diameter, t_{int} is the integration time, and C is the relative obscuration. The aperture diameter d_1 is known to 1 *mm*, as is the diameter of the obscuring secondary mirror d_2 , which is responsible for C in the larger telescope. Thus d_1 and C contribute uncertainties as follows:

$$\frac{\partial E}{\partial d_1} \sigma_{d_1} = \frac{8 \sum_{px} (Q_{px})}{(C - 1) d_1^3 \pi} \sigma_{d_1} \quad (31)$$

$$\frac{\partial E}{\partial C} \sigma_C = \frac{4 \sum_{px} (Q_{px})}{(C - 1)^2 d_1^2 \pi} \sigma_C \quad (32)$$

where σ_{d_1} and σ_C are the uncertainties in d_1 and C , respectively.

C is equal to the ratio of the area of the obscuring optic to the area of the whole aperture, that is, $C = \frac{d_2^2}{d_1^2}$. Thus the uncertainty in the relative obscuration C is

$$\sigma_C = \sqrt{\left(\frac{2d_2^2}{d_1^3}\sigma_{d_1}\right)^2 + \left(\frac{2d_2}{d_1^2}\sigma_{d_2}\right)^2}. \quad (33)$$

This leads to an expression for σ_E ,

$$\sigma_E = \sqrt{\left(\frac{\sigma_{Q_{img}}}{\frac{\pi d_1^2}{4}t_{int}(1-C)}\right)^2 + \left(\frac{8\sum_{px}(Q_{px})}{(C-1)d_1^3\pi}\sigma_{d_1}\right)^2 + \left(\frac{4\sum_{px}(Q_{px})}{(C-1)^2d_1^2\pi}\sigma_C\right)^2}. \quad (34)$$

Variations in the signal level over time may be caused by fluctuations in the background radiation, random noise due to the camera electronics, changes in laser output, and variations in atmospheric factors such as aerosol concentrations. Since the camera captures video, the irradiance is computed separately for each frame in a series of interest, and the final result is reported as an average of these. The standard deviation σ_t of these irradiances, then, provides an estimate of the time-varying error terms. To compute the uncertainty of the time-averaged values, the existing σ_E must be broken into its time-dependent and time-independent parts.

For this purpose, time-independent error terms will still be considered time-independent if they are multiplied by a time-dependent coefficient. For instance,

$$\frac{8\sum_{px}(Q_{px})}{(C-1)d_1^3\pi}\sigma_{d_1} \quad (35)$$

is considered time-independent because σ_{d_1} is time-independent, even though Q_{px} may vary with time. Although individual pixels may fluctuate considerably over time, the frame ranges have been selected such that the sum $\sum_{px}(Q_{px})$ should not fluctuate too drastically. The only time-dependent error term which must be considered is σ_{bg} , which can vary as the background fluctuates. All the other error terms are the result of measurements made prior to the collection.

When the images are averaged, they are summed and divided by the number of

frames. Since the background is simply subtracted from the image, it is effectively summed as well and divided by the same factor. The fluctuating background uncertainties do not correlate with one another, so they are summed in quadrature and then divided, so

$$\sigma_{bg_{avg}} = \frac{\sum_{frames} \sigma_{bg_{frame}}^2}{N}, \quad (36)$$

where N is the number of frames being averaged.

Separating σ_{bg} from the other terms yields the time averaged σ_E

$$\sigma_E = \sqrt{\frac{\sum_{px} (\sigma_{fit_{px}}^2 + D_{px}^2 \sigma_{g_{px}}) + \frac{1}{N} \sum_{img} \sigma_{bg}^2}{\left(\frac{\pi d_1^2}{4} t_{int} (1 - C)\right)^2} + \left(\frac{8 \sum_{px} (Q_{px})}{(C - 1) d_1^3 \pi} \sigma_{d_1}\right)^2 + \left(\frac{4 \sum_{px} (Q_{px})}{(C - 1)^2 d_1^2 \pi} \sigma_C\right)^2} + \sigma_t. \quad (37)$$

4.5 Computing irradiances in HELEEOS

For each image, the wavelengths and power levels of each laser were recorded using the calibration software, so that they would be stored alongside the rest of the data associated with that image. A script was written which ran HELEEOS with the parameters for each image (and each laser present in that image). When multiple lasers were present in an image, HELEEOS was run once for each, and the total reported. The results of these HELEEOS outputs will be reported in the following section and compared with the irradiances measured from the corresponding images.

V. Field Measurements

Field measurements were taken of a laser test conducted at Wright-Patterson Air Force Base Area B in July 2009. The test was conducted by AFRL over three days with the primary purpose of testing a new technique for measuring atmospheric turbulence. The three lasers used in the test operated at fixed wavelengths 1.533, 1.589, and 1.595 μm , respectively, and their power levels were adjusted from 0.6 to 5.7 W during the test. The two days of test data provided results for two different off-axis angles, nighttime and daytime conditions, as well as a significant amount of variation in laser power. Each data set was processed as described in the previous chapter, producing an irradiance value for each image. These irradiances were then compared with HELEEOS outputs for the same geometry and laser properties.

5.1 Experiment setup

Lasers. The lasers used were IPG Photonics erbium fiber lasers, models ELR-5-1595.3, ELR-5-1532.6, and ELR-5-1588.7. The spec sheets for each laser show their bandwidths to be $\pm 0.1 nm$, small enough to consider them monochromatic for this study. When operating from an outdoor location, the beams were pointed out the door of a trailer as shown in Figure 24. The lasers were reported to have an exit aperture of 4 mm and a spot size of 1.6 m at the target, so these values were entered into HELEEOS as shown in Figure 25

Experiment geometry. The 15 July 2009 test was conducted with a source laser at the west end of the abandoned runway at Patterson Field, with the target on the ninth floor of Building 622 [8]. Building 622, including the window which served as the target, is shown in Figure 26. The total distance from source to target was approximately 3050 m. The observer was located on a concrete pad on the west side



Figure 24. The trailer from which the lasers operated when located out doors. The apertures for each laser are at the front of the black cylindrical object pointing out of the trailer.

of the parking lot at Building 622, approximately 60 *m* from the target and 3015 *m* from the source. The distance from observer to target was measured using a laser rangefinder; all other distances were measured using Google Earth. This setup is shown in Figure 27.

The source was located at an elevation of 240 *m*, while the target was at 313 *m*. The observer was located at an elevation of 292 *m*. The observer elevation was computed relative to the building elevation by analyzing Figure 26. The elevation and altitude differences altogether place the observation location approximately 0.9 degrees off-axis.

For the 17 July 2009 test, the source laser was located near the east end of the abandoned runway at Patterson Field, with the target 2160 meters away at the west end of the runway. Off-axis scattering was observed from a location roughly 46 meters from the target in a direction perpendicular to the beam path. Thus the observer

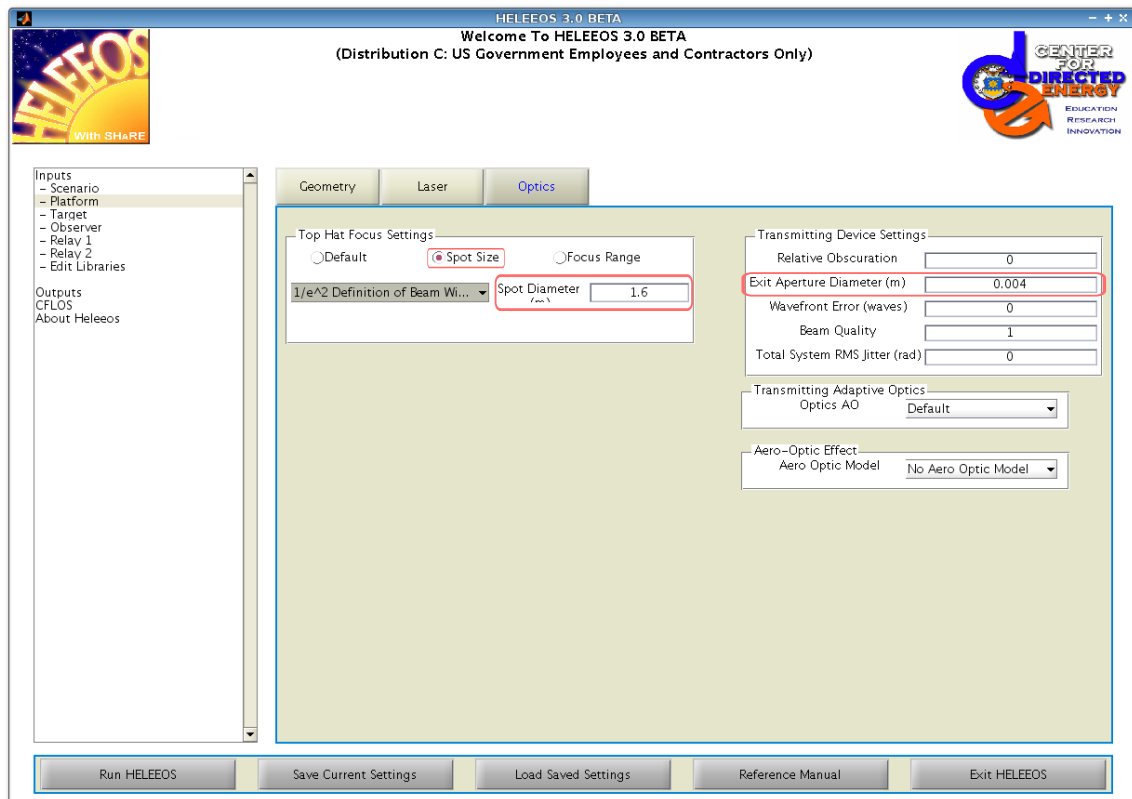


Figure 25. Optics settings for the lasers. Non-default values are marked in red.



Figure 26. Building 622 at Wright-Patterson Air Force Base. The target was in the left-most of the two visible windows.



Figure 27. Experiment geometry for the 15 July 2009 test. For this test, the observer was located almost directly below the beam. The 300 m field of view is representative of the 31.75 cm reflecting telescope, which was used for most of the observations on 15 July.

location is around 1.22 degrees off-axis. This setup is shown in Figure 28. The relevant distances were measured using a laser rangefinder. Observer, source, and target were all located at roughly the same elevation of 240 m.



Figure 28. Experiment geometry for the 17 July 2009 test. The source is denoted by a laser symbol, the target by a bulls-eye, and the observer by an eyeball. The observer's field of view is identified by a blue line along the laser beam path. The 400 m field of view is representative of the 10.1 cm refracting telescope, which was used for most of the observations on 17 July.

During the course of the experiment the lasers were sometimes walked off from the target, but the precise direction of the walk-off was not determined. Therefore, in computing the observer's off-axis angle it is assumed that the lasers are always pointed at the intended target. This off-axis angle is used both in determining the observation path and as an input parameter to HELEEOS.

Environmental conditions. Both days of testing were marked by fair weather, with temperatures around 20°C and scattered to broken cloud cover. National Weather Service records show the visibilities for both days to be 10 statute miles, but their measurements were limited to the farthest visible object. Those who were present at the test reported that the visibilities were extremely high, far above the 10 miles

reported.

The meteorological settings entered into HELEEOS were as follows: The approximate coordinates of Wright-Patterson Air Force Base were selected on the map and the DAYTON/WRIGHT-PATTE (sic) ExPERT site was selected. The “Enable Advanced Atmosphere Settings” checkbox was checked, as was the “Enable User Specified Ground Visibility,” checkbox, with the Aerosol Visibility setting set to 100 km. With these settings, HELEEOS was set to the ExPERT database for all weather parameters, except for the visibility which was set to a relatively high value to reflect the fact that the visibility was reported to be high by those present at the test. The HELEEOS Scenario pane is shown in Figure 29 with these settings entered.

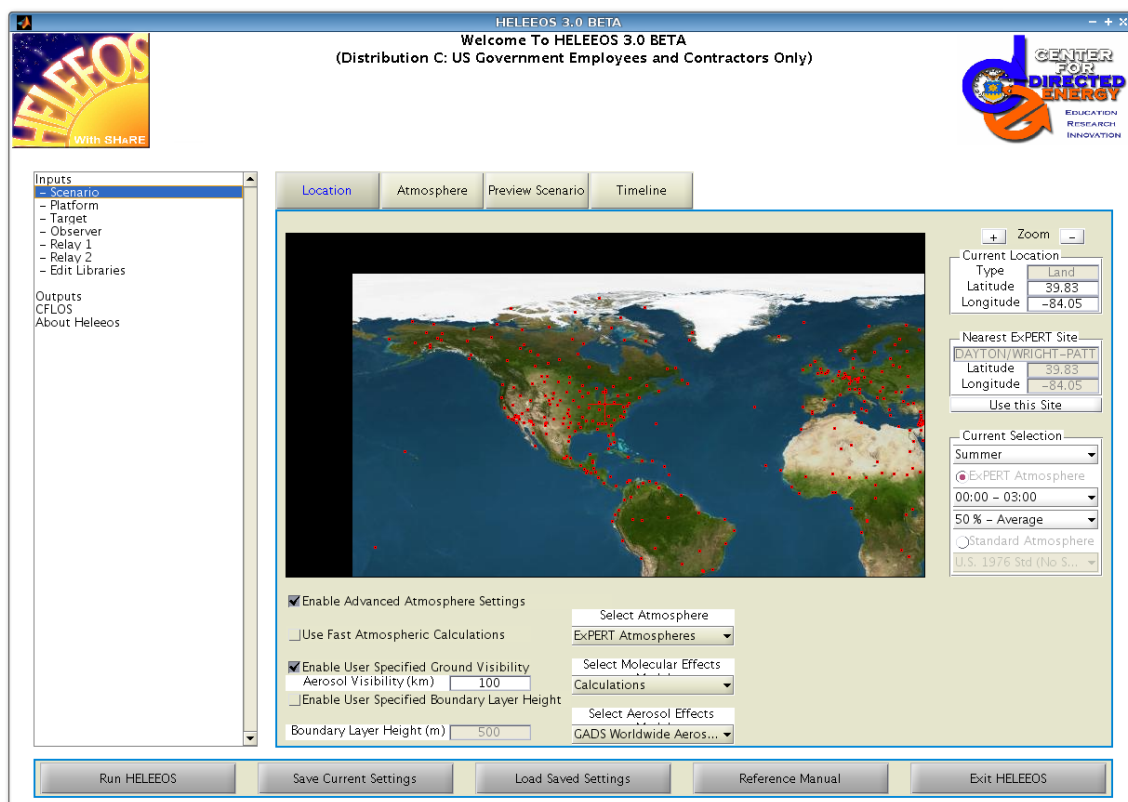


Figure 29. HELEEOS Scenario page, with fields populated with the input data used for HELEEOS runs in the study.

5.2 Image selection

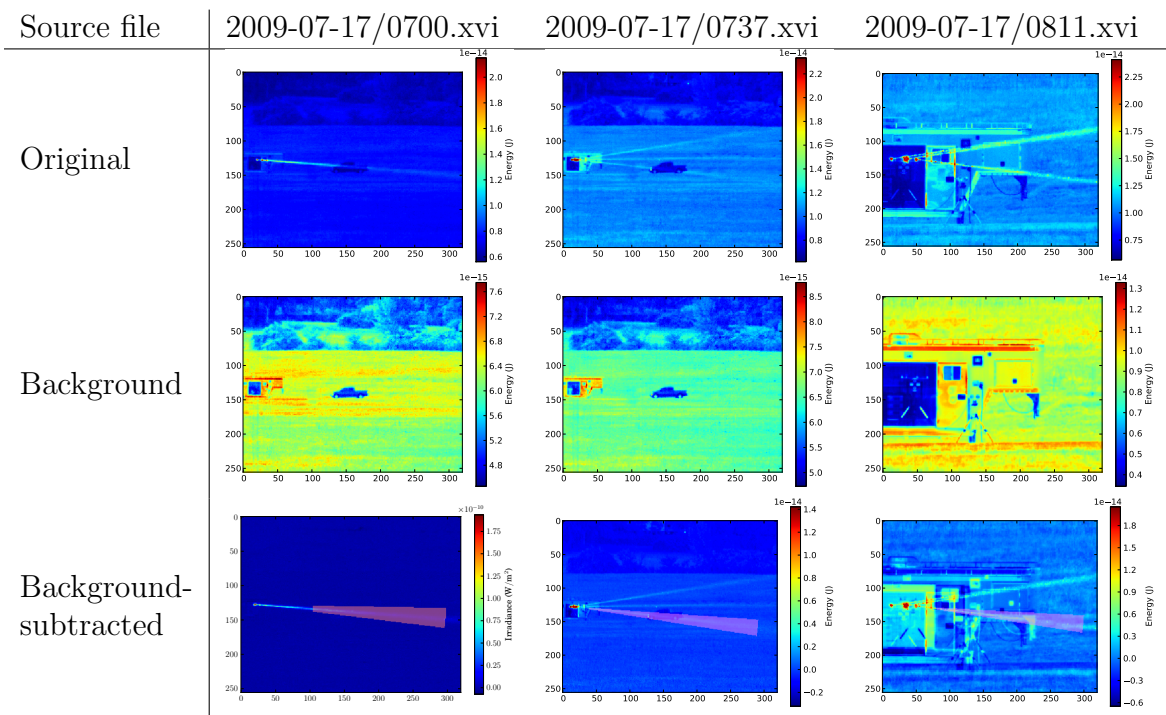
In order for a data collection to be used, atmospheric scattering must be visible in the images, and it must be possible to determine which of the lasers is responsible for the scattering. In addition, it must be possible to determine the physical location of the beam from image coordinates. In order to do this, images were selected in which the laser source was visible in the picture and in which the camera was stationary.¹ Finally, a background image must be available. Ideally this can be created from an average of frames in the same data set. For instance, if the movie shows the lasers being turned on or off it will often include a substantial number of frames in which no lasers are turned on. Otherwise, a background image can be constructed from another image of the same scene. When the background was constructed from another image, the result was generally inferior, but images processed in this way were kept since they did not consistently appear as outliers in the final data set.

The quality of the images used varied significantly. Most notable was the varying effectiveness of the background subtraction technique. The best results occurred when the background could be computed from different frames of the same file, while subtracting a background computed from a different file yielded far poorer results. Examples of the background subtraction results are shown in Table 1.

The left-hand column of Table 1 shows a highly successful background subtraction. The resulting image contains near-zero values almost everywhere except where the laser beam can be seen. The center column shows a moderately successful background subtraction. In this image, background features remain visible in the image after background subtraction has been performed, but the laser beam pixels generally contain much larger magnitudes than do background pixels.

¹It should be possible to handle the case of a panning camera using motion tracking software, or with other equipment it might have been possible to account for panning by measuring the camera direction in the field.

Table 1. Examples of background subtraction.



The right-hand column of Table 1 shows a relatively unsuccessful background subtraction. Many background features have magnitudes at or above those of the laser beam pixels, even after background subtraction. Still, the irradiances computed for these images did not tend to be outliers when compared with those computed from other images. As a result, less successful cases of background subtraction were included in the final data set.

5.3 Results

In total, the calibration was applied to 56 images taken at the July 2009 laser test. A detailed table of the results can be seen in Appendix C. For each image, an irradiance value was computed using HELEEOS and compared with that measured from the image. In a slight majority of cases, HELEEOS calculated irradiances 1-2 orders of magnitude higher than that measured in the field for the same scenario, as shown in Figure 30.

Each image showed scattering from either one, two, or all three lasers. When multiple laser beams were visible simultaneously, the sum of their power settings was shown as the “Laser power” on the x-axis of Figure 30. In a majority of cases, the lasers each operated at 0.6 W, accounting for the clusters of data at 0.6, 1.2, and 1.8 W. The three points plotted at around 17 W consisted of all three lasers operating at 5.5-5.7 W.

Figure 30 shows a weak downward trend in irradiance ratio as the laser power increases. There is not enough data at the higher power levels to ascertain whether this trend is representative of a real phenomenon or whether it is simply a side-effect of the small size of the data set.

Another view of this data set can be seen in Figure 31. This plot shows a weak correlation between measured irradiance and HELEEOS output. It is possible that

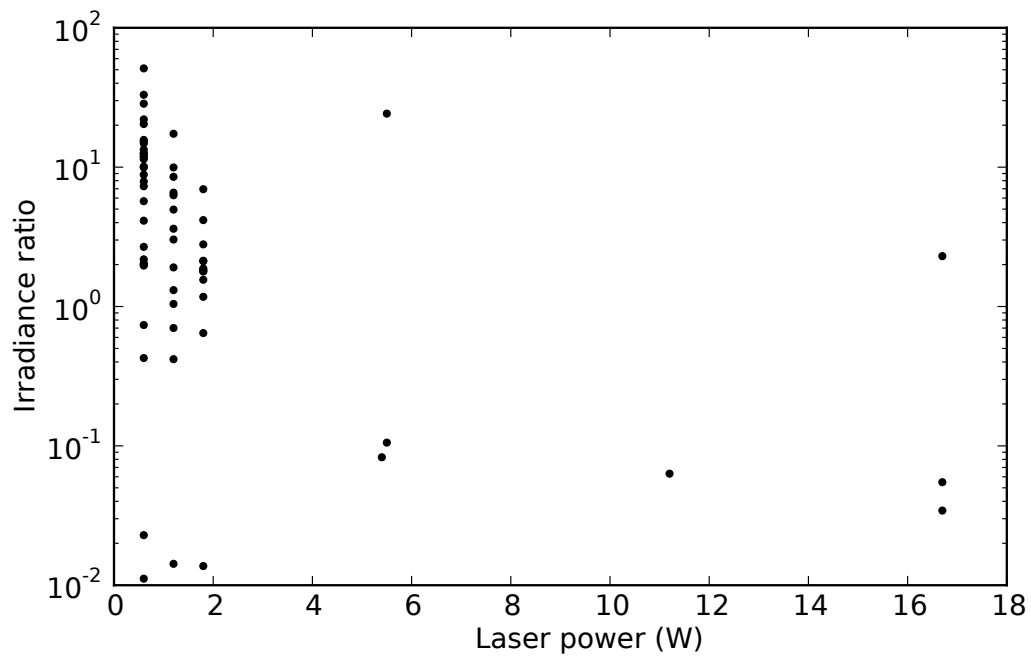


Figure 30. Ratios of HELEEOS-derived irradiances to the measured irradiances, as a function of laser power. HELEEOS outputs are always within two orders of magnitude of the measured irradiances, and frequently within one order of magnitude.

this correlation would appear stronger if more images were available at the higher laser powers, which would help show whether some of the poorly correlated points in this data set are anomalous or whether they are representative of typical variations.

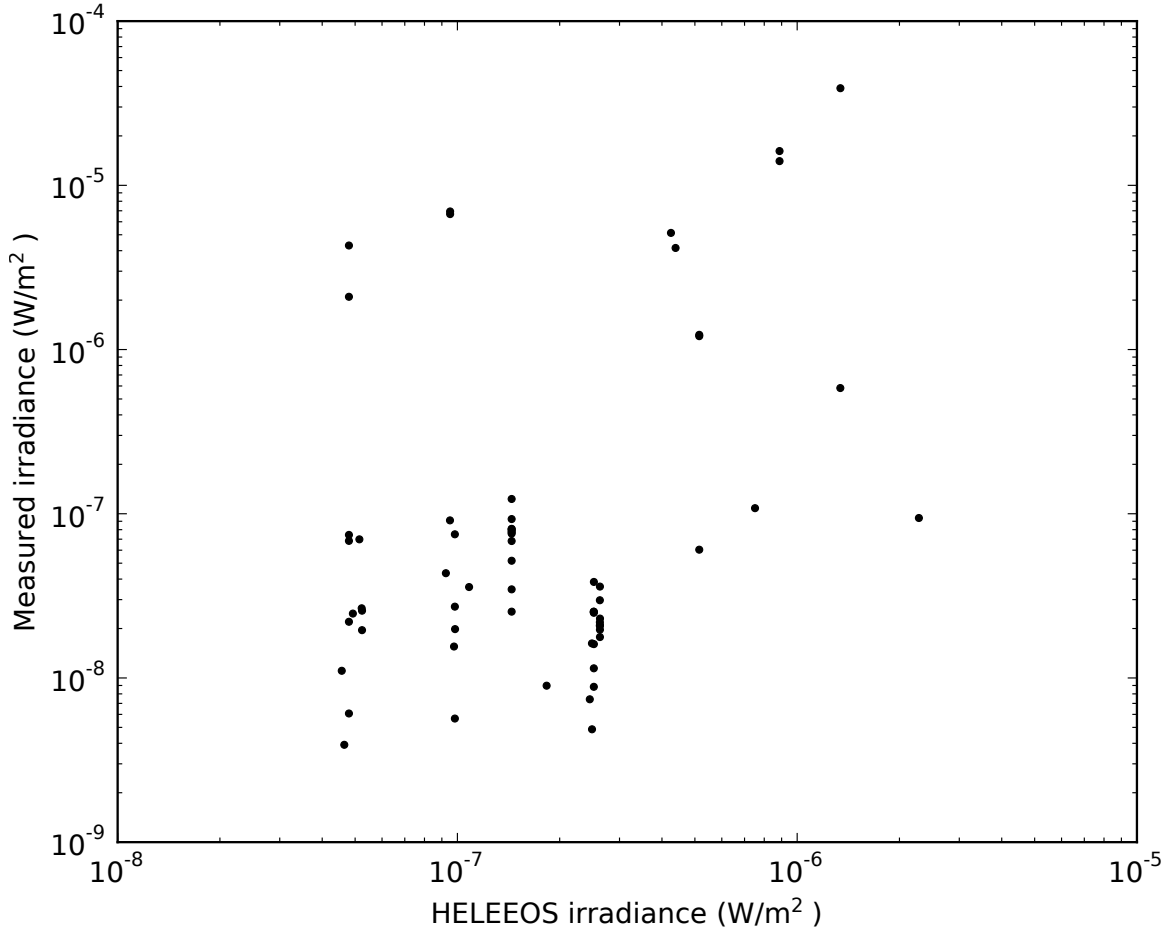


Figure 31. Comparison of HELEEOS-derived irradiances with measured irradiances, showing a weak correlation.

In nearly all of the field images, it is apparent that irradiance decays along the length of the beam. To determine whether HELEEOS outputs agreed with this trend, the the FOV Start and FOV Stop distances of the selection region were converted to angles in the observer’s field of view, and the angle range broken into increments of equal sizes, as shown in Figure 32. The start and stop angle of each increment was converted back into a distance range, which was passed to HELEEOS as the FOV

Starting Dist and FOV Ending Dist parameters. By running HELEEOS once for each angle increment, the trend of observer irradiance as a function of viewing angle could be determined. Similarly, the irradiances in the images were summed over each angle increment, producing measured irradiance values at intervals over the same range as was measured for HELEEOS.

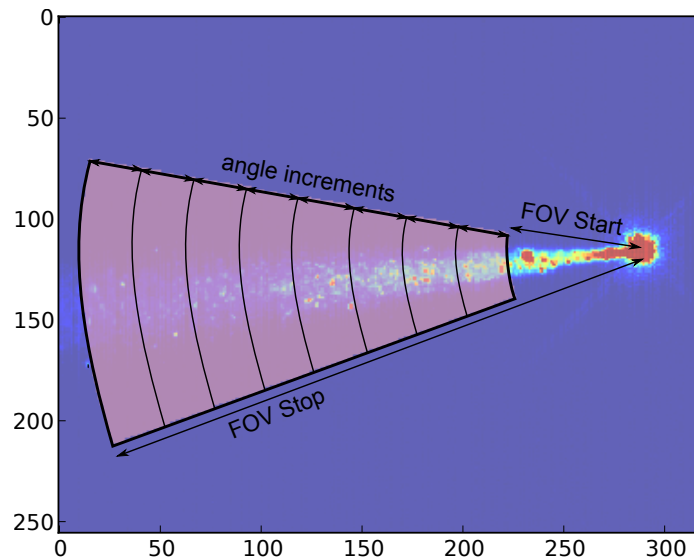


Figure 32. Angle increments within the selected field of view, used for computing irradiances as a function of viewing angle for Figure 33.

Results of this process for two images can be seen in Figure 33. For both images, a downward trend in irradiance can be seen in both the measurements and the HELEEOS outputs, although the overall magnitudes of the irradiances do not agree very well, nor do the rates at which the irradiance falls off with angle.

The beam could in some cases be detected at viewing angles as large as 20° , but at more extreme angles it became too dim for the camera to detect. Using the same process used previously to divide the field of view into equal angle increments, a succession of HELEEOS runs was performed using equal angle increments from 0° to 90° . In results of this test, shown in Figure 34, HELEEOS predicts the irradiance will continue to fall off through 75° , which is consistent with the fact that the beam

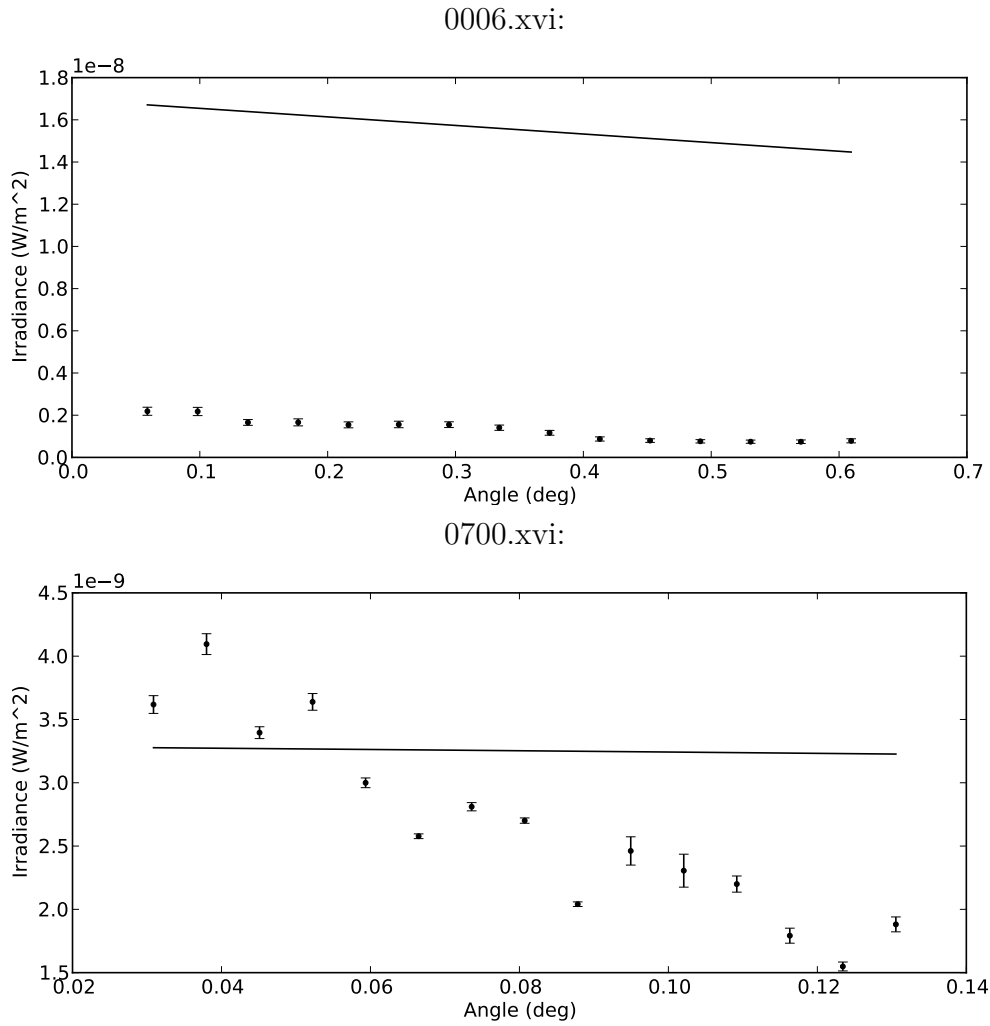


Figure 33. HELEEOS-predicted irradiance (solid lines) and measured irradiance (points) as a function of observation direction for two images. Although the overall magnitude differs between HELEEOS and the measured irradiance, as does the rate at which the irradiance falls off with distance, the downward trend is present in both.

was invisible to the camera at that angle.

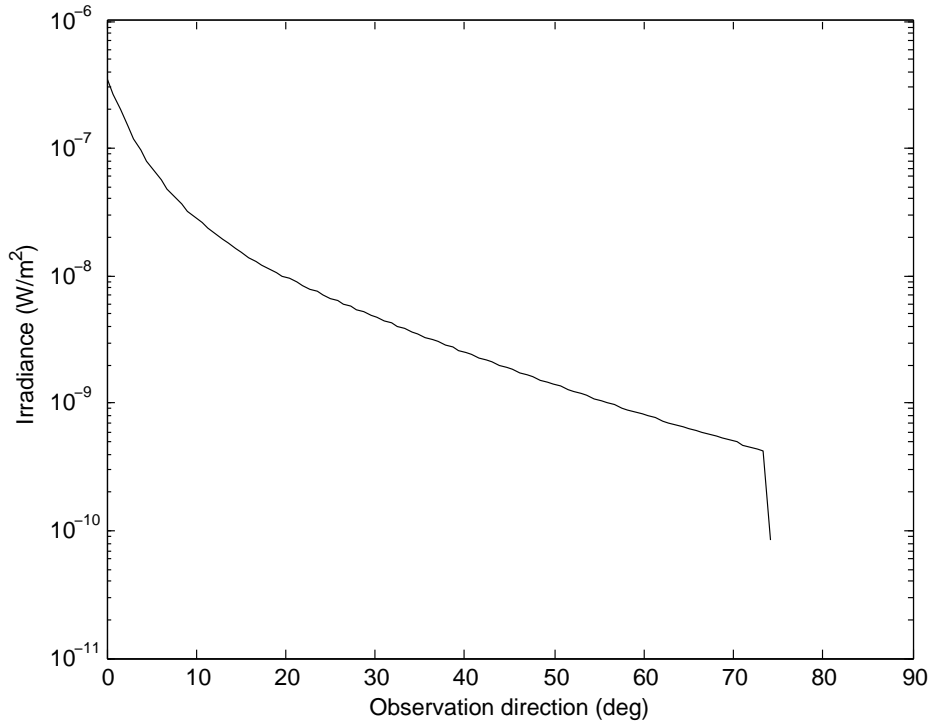


Figure 34. HELEEOS-predicted irradiance as a function of observation direction for an observer located 1.22° off-axis. Each point along the line represents an equal span of angles in the observer’s field of view. An observation angle of 0° indicates the observer is looking directly at the source; 90° indicates the observer is looking 90° away from the beam source, approximately perpendicular to the beam. HELEEOS outputs NaN for the irradiance from 75-90°.

The investigation into the viewing direction begs another question: How does the observer’s location off-axis affect the HELEEOS output? Since the Mie phase functions show strong forward scattering and a fairly rapid fall-off from the 0° direction, one would expect that the smallest off-axis angles (the angle between the observer and the laser beam path) will produce the greatest off-axis irradiances, with fairly rapid fall-off from there. Figure 35 shows HELEEOS-predicted irradiances for a range of small off-axis angles. As expected, the highest irradiances occur at the smallest angles, with a sharp reduction in irradiance as the observer is moved away from the beam.

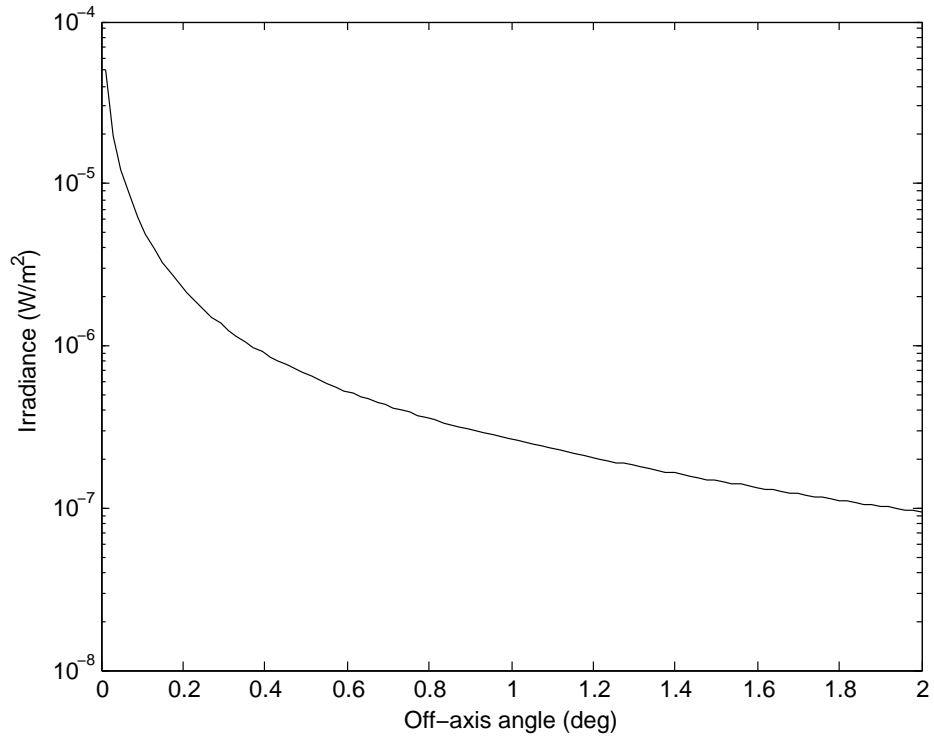


Figure 35. HELEEOS-predicted irradiance as a function of observer off-axis angle. Larger angles indicate the observer was further offset from the beam path, maintaining the same distance from the laser source. The strong dependence of the output on this parameter suggests that accurate results from HELEEOS require an accurate measurement of the experiment geometry.

The strong sensitivity of HELEEOS outputs to off-axis angle indicates that the off-axis angle must be determined precisely for the results to be accurate. The off-axis angles used for the test data, however, could only be determined to within 0.5° , but their magnitudes were on the order of 1° . This, combined with imprecisions in the other input parameters, provides one possible explanation for the wide disparities seen between HELEEOS and the test data.

At worst, HELEEOS agrees with the test data to within two orders of magnitude, although frequently it does much better than this, in some cases producing a value within a few percent of the test data. In addition, HELEEOS correctly predicts that irradiance should decay with respect to viewing direction. Imprecisions in the input parameters might explain many of the discrepancies. This test is not sufficient to validate HELEEOS, but it shows that HELEEOS has potential to be validated with further testing.

VI. Conclusions

The tests conducted in this research show some agreement between HELEEOS-predicted off-axis irradiances and those measured using a camera. The data were not in close enough agreement with HELEEOS to serve as a validation of HELEEOS by themselves, but HELEEOS showed some correlation with the test data in terms of laser power output and viewing angle.

For the entire set of test data, HELEEOS produced outputs within two orders of magnitude, and frequently within one order of magnitude. Although these errors are large, there are cases in which precision such as this would be adequate. For instance, if one wished to determine whether a certain laser could be detected under a particular set of conditions, one could use HELEEOS to do this. As long as HELEEOS predicted irradiances more than two orders of magnitude above or below the threshold for detection, one could make a fairly certain determination as to whether the laser could be detected under those conditions. For a laser weapon, a two order of magnitude accuracy would in certain cases be sufficient to determine whether a laser was capable of destroying a particular target.

Although the two order of magnitude threshold sets an upper bound on the uncertainty of HELEEOS results for this set of operating conditions (clear air, 1.5-1.6 μm , 0.6-5.7 W, and camera roughly 1° off axis), the real value of this test is to demonstrate techniques for collecting and analyzing off-axis scattering data, and to provide insights into the best path toward validating HELEEOS. The test showed that an infrared camera can be used successfully to measure off-axis scattering data, and techniques were developed that can be used to relate that data to HELEEOS inputs and outputs, both for purposes of validation and for later real-world applications. The large discrepancies between HELEEOS outputs and measured irradiances suggest that a sensitivity study of the off-axis scattering model should be accomplished in order to

guide further testing.

The quality of the input data to HELEEOS appears to have had a considerable influence on the off-axis scattering results. The off-axis angle (the angle at which the observer was off-set from the laser beam, measured from the source location) had magnitudes of 1.2° on the first day of testing and 0.9° on the second, but its uncertainty was on the order of 0.5° . Furthermore, it has been shown that HELEEOS off-axis scattering outputs are extremely sensitive to variations in this parameter when it is so small, so that changes of $\pm 0.5^\circ$ could change the results by an order of magnitude.

The atmospheric visibility could also influence the results by significant factors. Although the outputs are less sensitive to atmospheric visibility than they are off-axis angle, the range of possible visibilities was considerable. Atmospheric visibilities are typically reported based on the most distant visible object. Weather reports for Wright-Patterson Air Force Base never include visibilities over 10.0 miles because even on a perfectly clear day no objects beyond that distance can be seen. Those present at the test reported that the visibility during the test was much higher than that, but they could not quantify the actual visibility. A visibility of 100 km was chosen because it was consistent with the reports of excellent visibility, but this value could probably be set within a range of 50-200 km and remain consistent with those reports. Changes within this range can change the outputs by up to an order of magnitude.

The background subtraction did not always work as well as one would hope, because for some of the images the closest available background image had been taken several tens of minutes before or after the actual data. This certainly affected the accuracy of the irradiance values computed from these images. The best backgrounds were contained within the same animation file as the test data, so that the two were

very close in time. Future studies should take care to obtain high quality background images, as this can make a significant difference in the quality of results.

Another possible source of error is the laser power output. The power settings passed to HELEEOS came from the amount of electrical power used by the lasers, but in practice the optical power produced by the laser is probably significantly less than this. Placing a power meter in the beam path might help correct for this, although having one there continuously would partially block the beam and reduce the amount of scattered radiation.

Unfortunately, the data available gives no immediate indication as to whether the discrepancies are due to errors in HELEEOS or due to problems with the input data. Nonetheless, it gives some indications that the HELEEOS off-axis model is at least qualitatively accurate. The data also shows that HELEEOS irradiance varies with viewing angle in a manner similar to the physical reality. HELEEOS correctly predicts that irradiance should decay with viewing angle, and at extreme angles it produces very low irradiances consistent with the fact that the beam was not observable at those angles.

By collecting and analyzing off-axis scattered radiation, it has been demonstrated that off-axis scattering can be quantified for communications lasers, suggesting that with further refinement of the HELEEOS model and more accurate input parameters, much more consistent results can be obtained.

6.1 Future work

The existing data provides ample opportunities for additional work. Many of the images available were not used because of flaws which could be overcome with improvements to the calibration software. HELEEOS runs compared with these data were done using climatological weather and mostly default weather settings, but

studies could be done using actual weather conditions as well. Sensitivity studies of HELEEOS would help determine which input parameters, meteorological or otherwise, are most important to the observer irradiance output. Finally, HELEEOS could be compared with additional test data, including that already available from the December 2009 test in Dahlgren, VA.

6.1.1 Parameter sensitivities.

Since the HELEEOS outputs varied so widely compared with the measured irradiances, it would be valuable to conduct a sensitivity study on the off-axis scattering model in order to determine which parameters are most responsible for output variations. Once the parameters to which HELEEOS is most sensitive have been identified, care should be taken that those parameters are determined as precisely as possible while conducting tests of the off-axis scattering model.

A high degree of sensitivity has already been noted in the case of the off-axis angle, and this sensitivity is compounded by its small magnitude and comparatively large error term. This uncertainty may be reduced somewhat by increasing the off-axis angle, although doing so may make it more difficult to observe the beam.

6.1.2 Different geometries.

In addition to increasing the off-axis angle, observations should be made looking further down the beam rather than only a small distance from the source. A small number of images in the existing data set show irradiance farther down the beam, but these were not used because of difficulty in accurately determining the angles associated with individual pixels in those images. With some modification to the calibration software it should be possible to do so.

All the images in the existing data set showed forward scattering, and although

it has been seen that side-scattering may not be observable, it should be possible to produce images of back-scattering with a similar laser power. Indeed, back-scattering was observed (but not yet analyzed) in the recent Dahlgren, VA test.

6.1.3 Higher power tests.

It would be beneficial to test the off-axis scattering model against different laser equipment and under different environmental conditions. The July 2009 tests were conducted in very high visibility fair-weather conditions, with a narrow wavelength range and relative low power (compared with weaponized lasers). Tests against higher powered lasers, different wavelengths and different weather conditions would be beneficial. Data from the December 2009 test in Dahlgren, VA, once they are available, will help fulfill some of these needs. Although much of that test was also conducted in fair weather, the weather conditions were certainly somewhat different. Furthermore, the laser in use was much more powerful and operated at a significantly different wavelength than that used in the July 2009 test.

Because the Dahlgren, VA data were collected using CCD cameras rather than an InGaAs array, and because of the different calibration equipment available on site, a different calibration process must be used. The existing calibration software could be modified to accomplish this. The CCD's used at Dahlgren are to be calibrated against a laser source, which will not produce the constant radiation flux across the field of view that the 12-inch blackbody provided. Thus, an additional step may be required to measure the variance in quantum efficiency across the CCD or, alternatively, it may be assumed that the quantum efficiency is constant across the array. In either case, the existing calibration program is designed specifically to handle calibration against a blackbody, and would likely require modification to accommodate the new calibration process. The calibration software also would require modification in order

to be able to read the file format used to store the Dahlgren data.

6.1.4 Improvements to the calibration software.

The analysis process revealed some tolerable but noticeable performance limitations in the calibration tool. These could be addressed by re-writing the tool in a compiled language such as C or C++, or by implementing caching in order to reduce the number of floating point computations required. The latter would be more straightforward since the graphics features of the program use the matplotlib library which has no bindings for low-level languages. Alternatively, the low-level file i/o and numerical codes could be rewritten in a compiled language and the rest left in Python.

Integrating the calibration tool with HELEEOS would make the analysis process more convenient. It is possible to call Matlab from inside a Python script, and this capability was used to call HELEEOS in order to generate many of the numbers used in this thesis. However, this was done from a separate script, and was not integrated into the main calibration tool. Doing so would be fairly straightforward, depending on what subset of the HELEEOS inputs and outputs were exposed.

Another, potentially more interesting, modification would be to add a motion tracking capability. This would provide a means to use some of the images collected at the July 2009 test which could not be analyzed with the current program because the camera was shaking or panning during the shot. This would also improve the accuracy of output for some of the images which were analyzed in spite of moderate camera shake.

6.1.5 Inputting real weather data into HELEEOS.

The existing data set still leaves considerable possibilities for further study. In addition to analyzing some of the images omitted from analysis in this study, all the images could be re-analyzed using real weather data. By default, HELEEOS determines weather conditions from a climatological database, taking into account the location, season (summer or winter), time of day, and relative humidity. For this study, only the location was changed from the default. Future studies could replace these settings with actual weather conditions.

Most weather data could simply be acquired from National Weather Service records, but as discussed previously, the recorded visibilities are frequently well below the actual ones. Instead of inputting a visibility to HELEEOS, data from an aerosol particle counter could be used as inputs to the Mie scattering model. Particle counter data are available for the current data set but were not used in the current study. After the actual weather conditions are taken into account, a more detailed comparison between HELEEOS and the test data may be possible, hopefully providing a means to identify areas for improvement in the HELEEOS model.

6.2 Closing remarks

The techniques described here have proven effective for measuring off-axis irradiances for comparison with HELEEOS. Each laser scattering image can be reduced to a single irradiance value which can be compared with HELEEOS output. The present study found considerable discrepancies between HELEEOS and actual irradiance values, but was unable to determine whether HELEEOS itself or its input data were most responsible for the discrepancies in irradiance results. Further studies, with these data or with others, may provide a means to do so.

Appendix A. Calibration software user documentation

This section describes the calibration software in more detail from a user's perspective, providing a general description of the interface and how it is used.

1.1 Dependencies

The software has been tested on Ubuntu Linux 9.10. It should be possible to run it on other operating systems once the following dependencies are installed:

- python 2.4
- pygtk 2.4 or greater with libglade support
- NumPy 1.3.0 or greater
- SciPy 0.7.1 or greater
- matplotlib 0.99.1 or greater

The script `analyseFieldImages.py` calls HELEEOS to evaluate predicated irradiances; this script adds the following dependencies in order to interface with MATLAB:

- mlabwrap 1.1 or greater
- csh (required by mlabwrap)

1.2 Using

The application is launched by running `calgui.py`. This will display the application's main window, shown in Figure 36

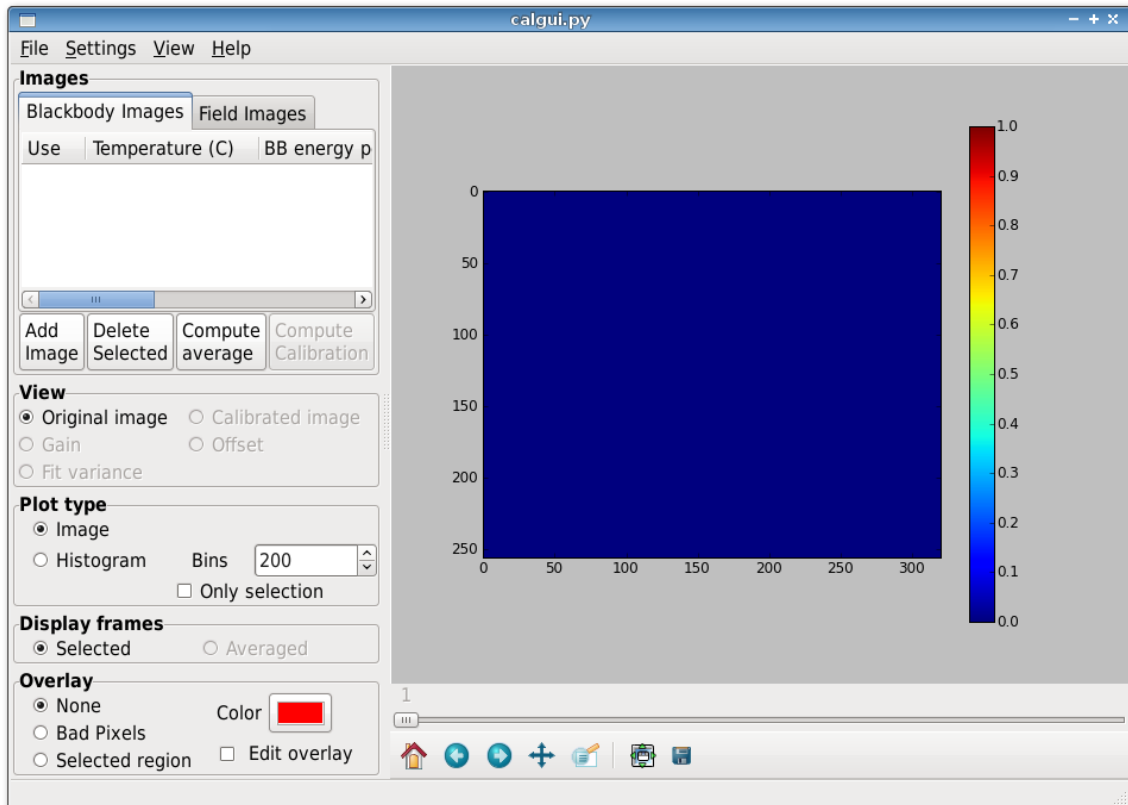


Figure 36. The calibration program's main window

1.2.1 Calibration scenarios.

A calibration scenario defines all the blackbody images and relevant settings used to build a calibration, as well as field images to which the calibration is to be applied. Calibration scenarios may be loaded by selecting “Open” from the File menu in the main window, and saved by selecting “Save” from the File menu.

1.2.2 Loading and editing images.

The **Add Image** button launches a file chooser dialog in which one can pick a XeniCS XVI file to load. The image is added to the Blackbody Images table or the Field Images table, depending on which of those tabs is selected.

When an image is added, an Image Properties dialog appears, prompting for temperature, integration time, and a frame range for averaging. The temperature should be the temperature of the blackbody for blackbody images; it is not used for field images. All properties can be edited later from the table.

The Blackbody Images table, shown in Figure 37, shows all the blackbody images defined in the loaded calibration scenario. Table 3 lists the fields in this table.

Table 2. Fields in the Blackbody Images table

	Use
Temperature	Whether the image is used in computing the calibration
BB energy per pixel^a	The blackbody temperature
	The energy in Joules received by each pixel according to Planck theory for a blackbody of the given temperature
Integration time	The integration time set when taking the image
Start frame	The start of the frame range for averaging
Stop frame	The end of the frame range for averaging
Filename^a	The path of the XVI file

^aNon-editable field

Use	Temperature (C)	BB energy per pixel	Integration time (ms)	Start frame	Stop frame	Filename
<input checked="" type="checkbox"/>	200	4.5726e-16	8000	1	371	/var/thesisd
<input type="checkbox"/>	300	1.7177e-14	10000	1	111	/var/thesisd
<input type="checkbox"/>	300	1.7177e-14	10000	1	240	/var/thesisd
<input checked="" type="checkbox"/>	400	9.3952e-15	500	1	715	/var/thesisd

Figure 37. The table of blackbody images

The Field Images table, shown in Figure 38, shows all the blackbody images defined in the loaded calibration scenario. Table 3 lists the fields in this table.

Table 3. Fields in the Field Images table

Bg Sub	Whether to do background subtraction for the image (only works after the average has been computed)
Integration time	The integration time set when taking the image
Start frame	The start of the frame range for averaging
Stop frame	The end of the frame range for averaging
Filename^a	The path of the XVI file

^aNon-editable field

1.2.3 Viewing images.

When an image is selected in one of the image tables, the figure pane is immediately updated according to the view settings. The data to be displayed may be selected under the following options shown in the “View” section of the main window. Table 4 shows the possible values.

The frame to be shown is selected using a slider under the figure area, or if the average has been computed the average may be displayed instead of the selected frame by selecting the “Averaged” radio button in the “Display frames” section.

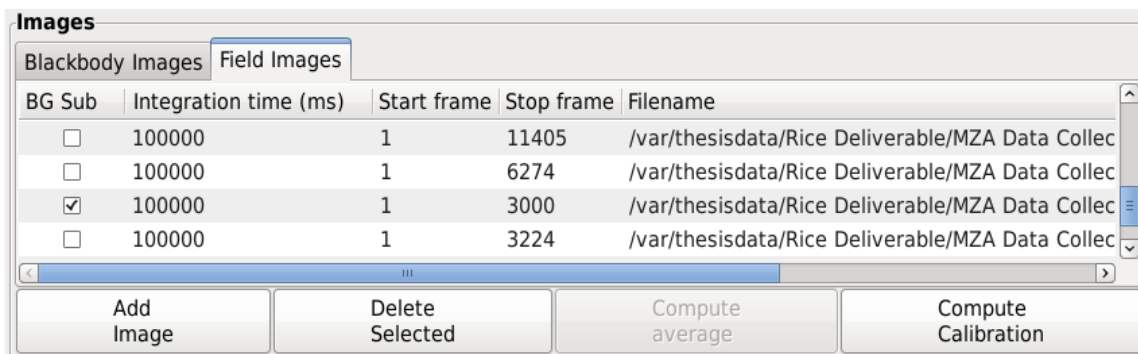


Figure 38. The table of field images

Table 4. View types	
Option	Data displayed
Original Image	Raw image data (possibly averaged)
Calibrated Image	Image data with calibration applied
Gain	Calibration gain array
Offset	Calibration offset array
Fit variance	Errors computed for each pixel

1.2.4 Overlays.

An overlay is an array of boolean data which may be drawn on top of the image. Two data sets may be overlaid: The “bad pixel” array computed from the calibration, and the “selected region,” which is created according to the procedure in Section 1.4.2. The overlay color and opacity can also be changed.

When the “Edit overlay” box is checked, the overlay may be edited manually. As long as the figure is not in “pan/zoom” or “zoom to rectangle” mode, a pixel can be added to the overlay array with a left mouse button click, or removed with a right click.¹

¹This feature is currently broken, and may never be fixed as it has become unnecessary due to improvements in the way the bad pixel array is initially computed.

1.3 Viewing histograms

By default, the data is displayed in the form of an image, but by selecting “Histogram” under the “Plot type” section, a histogram may be displayed instead. When displaying the histogram, the number of bins may be set using a text box. If the “Only selection” box is checked, the histogram will be computed using the pixels of the selected region (see Section 1.4.2) rather than the entire image.

1.4 Image settings

The Image Settings dialog can be accessed from the Image Settings option on the Settings menu, or by right-clicking on an image and selecting Image Settings from the menu that appears. The options in the Image Settings dialog vary depending on whether the image selected is a blackbody or a field image.

The appearance of this dialog for a field image is shown in Figure 39; its appearance for a blackbody image is shown in Figure 40.

1.4.1 Image section.

This section is available for both blackbody and field images. It displays the filename and provides a field to set or change the image’s integration time.

1.4.2 Field Scenario section.

This section is available only for field images. It provides an interface for setting observer geometry settings, laser wavelengths and power levels, the frame range, and the background image to use.

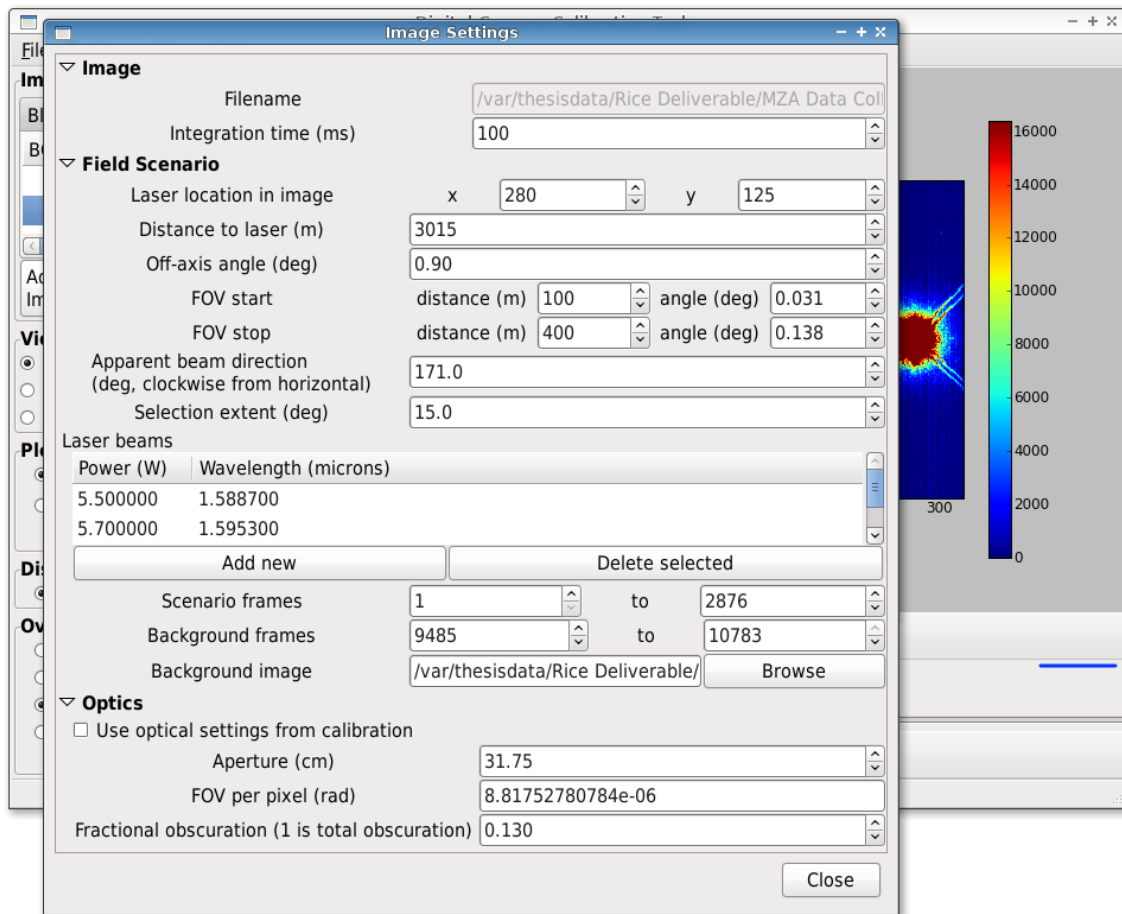


Figure 39. Image Settings dialog for a field image

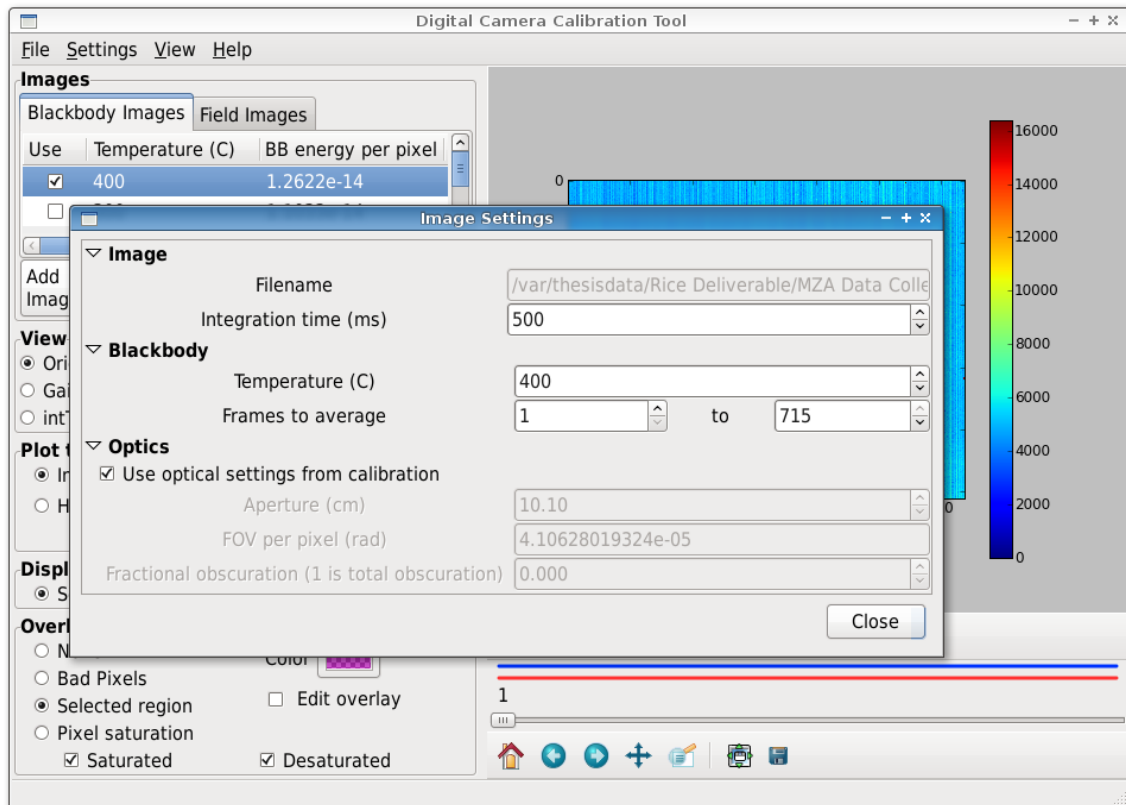


Figure 40. Image Settings dialog for a blackbody image

1.4.3 Optics section.

This section is available for both blackbody and field images. It contains settings related to the optics used to take the image.

Table 5. Options in the Image Settings dialog

Image	
Integration time	Camera integration time in μs
Blackbody	
Temperature	Blackbody temperature
Frames to average	Frame range to average for use in calibration
Field Scenario	
Laser location	Location of the laser source in image coordinates
Distance to laser	Distance from the laser source to the camera
Angle between observer, laser, and target	Angle between laser beam and observer path (angle B in Figure 7)
FOV starting distance	Start distance in meters along laser beam path (will be converted to image space)
FOV stopping distance	Stop distance in meters along laser beam path (will be converted to image space)
Apparent beam direction	Direction beam points in image space (clockwise where 0° points to the right)
Selection extent	How many degrees off of the beam direction a pixel must be before it is considered outside of the selection
Laser beams	Power and wavelength of each beam visible in the selection region
Scenario frames	Range of frames to use when computing the irradiance of the image
Background frames	Range of frames to average for use as a background
Background image	Filename of the file to use for the background. Defaults to the current image.
Optics	
Use optics settings from calibration	Whether the optics settings (aperture, obscuration, FOV) are the same as were used in the calibration (other fields in this section are disabled if this is checked)
Aperture	Aperture diameter of the receiving optic
FOV per pixel	Field of view in radians of a single pixel
Fractional obscuration	Fraction of the aperture that is obscured by a secondary mirror or other objects

Appendix B. HELEEOS inputs

The HELEEOS settings given here were used by default for all HELEEOS runs in the project. Observer and laser settings were overridden from these defaults based on the conditions under which each field image was taken. Specifically, the observer “Relative Azimuth from Platform” setting was replaced by $(90 - \theta_{obs})$ where θ_{obs} is the observer’s off-axis angle, and the observer “Initial Distance from Platform” setting was replaced by the actual distance from the source laser to the observer.

Table 6. HELEEOS inputs

Scenario: Location tab

Latitude	39.83
Longitude	-84.05
ExPERT Site	DAYTON/WRIGHT-PATTE
Season	Summer
Time of Day	00:00-03:00
ExPERT percentile	50% - Average
Enable Advanced Atmosphere Settings	Checked
Use Fast Atmospheric Calculations	Unchecked
Select Atmosphere	ExPERT Atmospheres
Enable User Specified Ground Visibility	Checked
Aerosol Visibility (km)	100
Select Molecular Effects Model	Calculations
Select Aerosol Effects Model	GADS Worldwide Aerosols
Enable User Specified Boundary Layer Height	Unchecked

Scenario: Atmosphere tab

Turbulence	HV 5/7
Turbulence Multiplier	1
Select Wind Model	Climatological Wind Profile
Enable Clouds and Rain	Unchecked

Platform: Geometry tab

Initial Altitude	2
Initial Relative Azimuth to next Object	90
Initial Distance to next Object	2150
Horizontal Velocity (m/s)	0
Velocity Heading (0 is North)	320
Vertical Velocity (m/s)	0
Vertical Acceleration (m/s ²)	0

Platform: Laser tab

Laser Propagation Model	Top Hat
Laser Type	Continuous Wave (CW)
Laser Wavelength	User Wavelength
User Wavelength	1.533e-6
Power (W)	0.6

Platform: Optics tab

Top Hat Focus Settings	Spot Size
Beam Width	$1/e^2$ Definition of Beam Width
Spot Diameter (m)	1.6
Relative Obscuration	0
Exit Aperture Diameter (m)	0.004
Wavefront Error (waves)	0
Beam Quality	1
Total System RMS Jitter (rad)	0
Optics AO	Default
Aero-Optic Effect	No Aero Optic Model

Platform: Lethality tab

Shape of the susceptible area of the target	Rectangular
Susceptible Target Width (m)	0.05
Distribution Type	Normal Distribution
Target Damage Threshold (J/m^2)	$5e7$
Target Damage Threshold (J/m^2)	$1e7$

Observer: Geometry tab

Enable Observer	Checked
Initial Altitude (m)	2
Initial Distance from Platform (m)	2160
Relative Azimuth from Platform	88.78
Horizontal Velocity (m/s)	0
Vertical Velocity (m/s)	0
Vertical Acceleration (m/s^2)	0

Observer: Optics tab

Beam to be Observed	Platform to Target
Focusing	Linear Focusing
FOV Starting Dist (m)	300
FOV Ending Dist (m)	750
Jitter (rad)	0
Relative Obscuration	0
Input Aperture Diameter (m)	0.101
Observer AO	Default

Relay 1: Geometry tab

Enable Relay 1	Unchecked
----------------	-----------

Relay 2: Geometry tab

Enable Relay 2	Unchecked
----------------	-----------

Edit Libraries: Atmosphere tab

Internet Database	Please Select ...
-------------------	-------------------

Edit Libraries: Advanced AO tab

Type of AO System	HWFS_DM
Error Rejection Bandwidth (Hz)	0
Latency of Transmit Loop (s)	0
Deformable Mirror Actuator Spacing (m)	0
Diameter of Beacon from Transmitter (m)	0
Type of Track System	FPA_FSM
Error Rejection Bandwidth (Hz)	0
Latency of Transmit Loop (s)	0

Appendix C. Table of field images with corresponding data

For each image used, the relevant configuration information is given, along with the irradiances computed by the Digital Camera Calibration Tool (DCCT) and by HELEEOS. Some image files are listed more than once because several different frame ranges were used, or because multiple selection areas were used due to lasers pointing in different directions.

Two optical setups were used, referred to by the names “Small telescope” and “Large telescope.” Their properties are listed in Table 7.

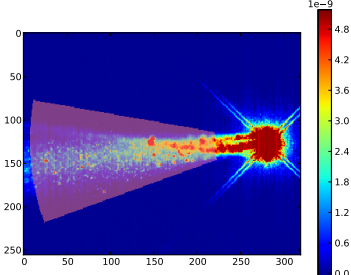
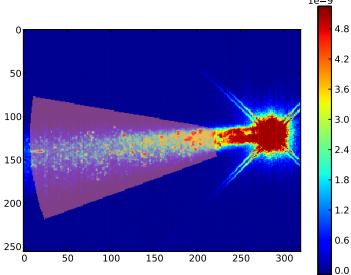
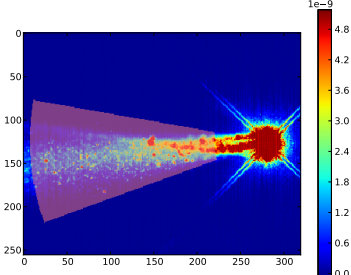
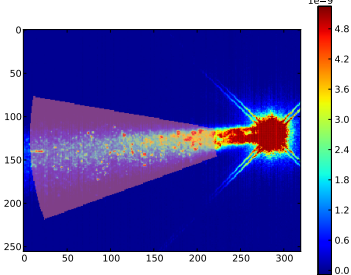
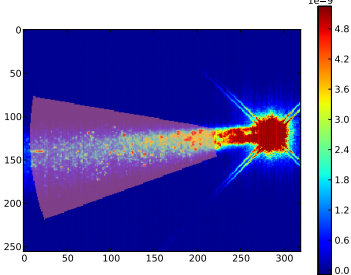
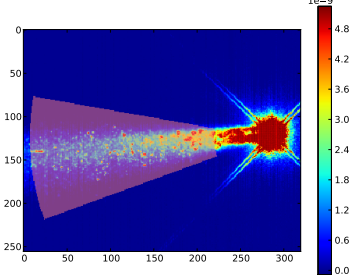
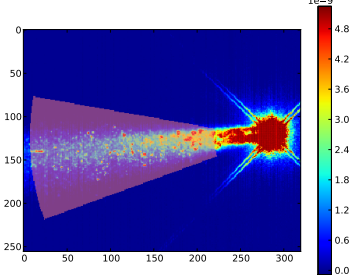
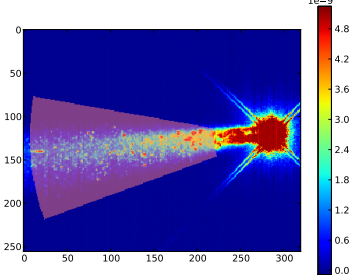
Table 7. Properties of the two optical setups.

Name	Aperture (cm)	FOV per pixel(rad)	Relative obscuration
Small telescope	10.10	$4.10628019324 \times 10^{-5}$	0.0
Large telescope	31.75	$8.81752780784 \times 10^{-6}$	0.130

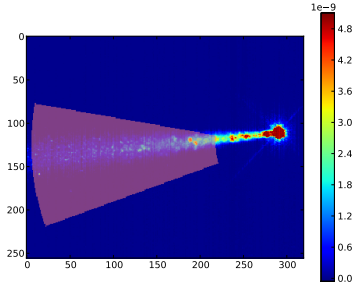
The distance from the laser to the observer is given; this value was assigned in the HELEEOS observer settings accordingly. The off-axis angle was subtracted from 90° and passed to HELEEOS as the “Relative Azimuth from Platform.” For instance, where the off-axis angle was 0.9° , the “Relative Azimuth from Platform” parameter was set to $90 - 0.9 = 89.1^\circ$. The FOV range values given were applied to the “FOV Starting Dist” and “FOV Ending Dist” parameters in HELEEOS. One HELEEOS run was performed for each laser in each image, and the results were added together to obtain the HELEEOS irradiances given here.

The uncertainties for the DCCT output were computed as the standard deviation of the irradiances for all the frames.

Table 8. Field irradiance and corresponding HELEEOS output (red areas in the images denote the region over which summation was performed)

		2009-07-15/0004.xvi (frames 1-2876)									
		Optics:	Large telescope								
		Distance:	3015 m								
		Off-axis angle:	0.900°								
		FOV range:	100 – 400 m								
		<table border="1"> <thead> <tr> <th></th> <th>Wavelength</th> <th>Power</th> </tr> </thead> <tbody> <tr> <td rowspan="3">Lasers:</td> <td>1.5887μm</td> <td>5.50 W</td> </tr> <tr> <td>1.5953μm</td> <td>5.70 W</td> </tr> <tr> <td>1.5326μm</td> <td>5.50 W</td> </tr> </tbody> </table>			Wavelength	Power	Lasers:	1.5887 μm	5.50 W	1.5953 μm	5.70 W
	Wavelength	Power									
Lasers:	1.5887 μm	5.50 W									
	1.5953 μm	5.70 W									
	1.5326 μm	5.50 W									
		DCCT irradiance:	$1.617 \times 10^{-05} \pm 3.07 \times 10^{-07} \text{ W/m}^2$								
		HELEEOS irradiance:	$8.874 \times 10^{-07} \text{ W/m}^2$								
		2009-07-15/0004.xvi (frames 3245-6455)									
		Optics:	Large telescope								
		Distance:	3015 m								
		Off-axis angle:	0.900°								
		FOV range:	100 – 400 m								
		<table border="1"> <thead> <tr> <th></th> <th>Wavelength</th> <th>Power</th> </tr> </thead> <tbody> <tr> <td rowspan="2">Lasers:</td> <td>1.5887μm</td> <td>5.50 W</td> </tr> <tr> <td>1.5953μm</td> <td>5.70 W</td> </tr> </tbody> </table>			Wavelength	Power	Lasers:	1.5887 μm	5.50 W	1.5953 μm	5.70 W
	Wavelength	Power									
Lasers:	1.5887 μm	5.50 W									
	1.5953 μm	5.70 W									
		DCCT irradiance:	$1.404 \times 10^{-05} \pm 4.95 \times 10^{-07} \text{ W/m}^2$								
		HELEEOS irradiance:	$8.874 \times 10^{-07} \text{ W/m}^2$								

2009-07-15/0004.xvi (frames 6490-9425)



Optics: Large telescope

Distance: 3015 m

Off-axis angle: 0.900°

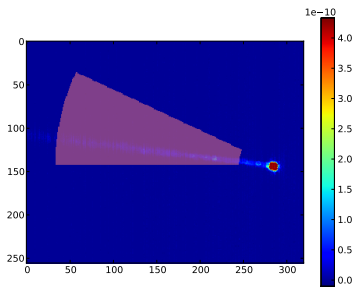
FOV range: 100 – 400 m

Lasers:	Wavelength	Power
	1.5887 μ m	5.50 W

DCCT irradiance: $4.156 \times 10^{-06} \pm 1.77 \times 10^{-07} W/m^2$

HELEEOS irradiance: $4.386 \times 10^{-07} W/m^2$

2009-07-15/0005.xvi (frames 4118-13056)



Optics: Small telescope

Distance: 3015 m

Off-axis angle: 0.900°

FOV range: 299 – 1200 m

Lasers:	Wavelength	Power
	1.5887 μ m	5.50 W

DCCT irradiance: $9.421 \times 10^{-08} \pm 9.28 \times 10^{-09} W/m^2$

HELEEOS irradiance: $2.282 \times 10^{-06} W/m^2$

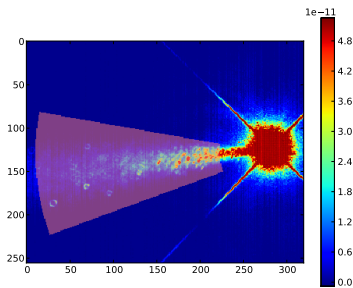
2009-07-15/0006.xvi (frames 11822-22138)

Optics: Large telescope

Distance: 3015 m

Off-axis angle: 0.900°

FOV range: 100 – 400 m



	Wavelength	Power
--	------------	-------

Lasers:	1.5887 μ m	0.60 W
---------	----------------	--------

	1.5953 μ m	0.60 W
--	----------------	--------

DCCT irradiance: $9.113 \times 10^{-08} \pm 4.57 \times 10^{-09} \text{ W/m}^2$

HELEEOS irradiance: $9.509 \times 10^{-08} \text{ W/m}^2$

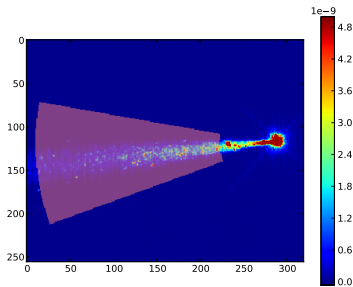
2009-07-15/0008.xvi (frames 7986-16537)

Optics: Large telescope

Distance: 3015 m

Off-axis angle: 0.900°

FOV range: 100 – 400 m



	Wavelength	Power
--	------------	-------

Lasers:	1.5857 μ m	0.60 W
---------	----------------	--------

DCCT irradiance: $4.301 \times 10^{-06} \pm 1.66 \times 10^{-07} \text{ W/m}^2$

HELEEOS irradiance: $4.795 \times 10^{-08} \text{ W/m}^2$

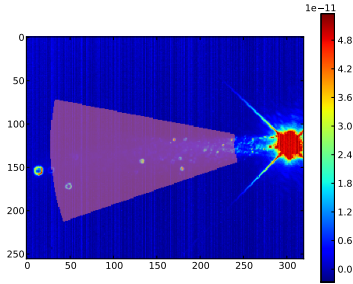
2009-07-15/1109.xvi (frames 1-9273)

Optics: Large telescope

Distance: 3015 m

Off-axis angle: 0.900°

FOV range: 100 – 400 m



	Wavelength	Power
Lasers:	1.5326 μ m	0.60 W
	1.5857 μ m	0.60 W
	1.5953 μ m	0.60 W

DCCT irradiance: $3.464 \times 10^{-08} \pm 7.38 \times 10^{-09} \text{ W/m}^2$

HELEEOS irradiance: $1.444 \times 10^{-07} \text{ W/m}^2$

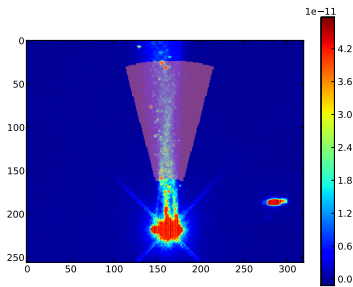
2009-07-15/2243.xvi (frames 1-5588)

Optics: Large telescope

Distance: 3015 m

Off-axis angle: 0.900°

FOV range: 100 – 299 m



	Wavelength	Power
Lasers:	1.5326 μ m	0.60 W
	1.5857 μ m	0.60 W
	1.5953 μ m	0.60 W

DCCT irradiance: $4.345 \times 10^{-08} \pm 2.13 \times 10^{-09} \text{ W/m}^2$

HELEEOS irradiance: $9.248 \times 10^{-08} \text{ W/m}^2$

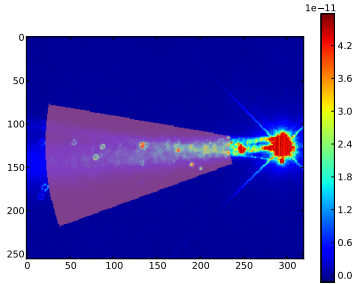
2009-07-15/2250.xvi (frames 1-6962)

Optics: Large telescope

Distance: 3015 m

Off-axis angle: 0.900°

FOV range: 100 – 400 m



	Wavelength	Power
Lasers:	1.5326 μ m	0.60 W
	1.5857 μ m	0.60 W
	1.5953 μ m	0.60 W

DCCT irradiance: $6.822 \times 10^{-08} \pm 2.54 \times 10^{-09} \text{ W/m}^2$

HELEEOS irradiance: $1.444 \times 10^{-07} \text{ W/m}^2$

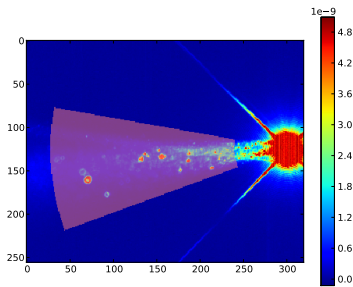
2009-07-15/2300.xvi (frames 1-2408)

Optics: Large telescope

Distance: 3015 m

Off-axis angle: 0.900°

FOV range: 100 – 400 m

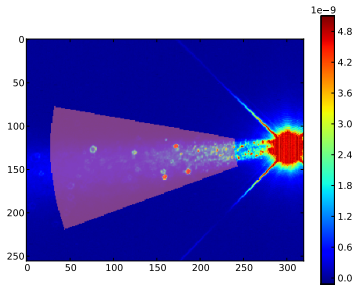


	Wavelength	Power
Lasers:	1.5857 μ m	0.60 W
	1.5953 μ m	0.60 W
	1.5326 μ m	0.60 W

DCCT irradiance: $6.935 \times 10^{-06} \pm 3.16 \times 10^{-07} \text{ W/m}^2$

HELEEOS irradiance: $9.519 \times 10^{-08} \text{ W/m}^2$

2009-07-15/2300.xvi (frames 2583-2791)



Optics: Large telescope

Distance: 3015 m

Off-axis angle: 0.900°

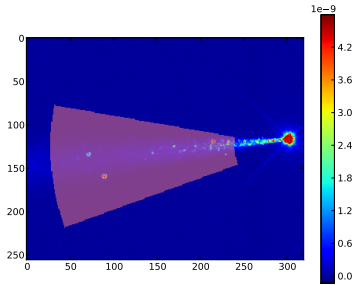
FOV range: 100 – 400 m

	Wavelength	Power
Lasers:	1.5857 μ m	0.60 W
	1.5953 μ m	0.60 W

DCCT irradiance: $6.682 \times 10^{-06} \pm 2.72 \times 10^{-07} \text{ W/m}^2$

HELEEOS irradiance: $9.519 \times 10^{-08} \text{ W/m}^2$

2009-07-15/2300.xvi (frames 2837-3082)



Optics: Large telescope

Distance: 3015 m

Off-axis angle: 0.900°

FOV range: 100 – 400 m

	Wavelength	Power
Lasers:	1.5857 μ m	0.60 W

DCCT irradiance: $2.096 \times 10^{-06} \pm 7.37 \times 10^{-08} \text{ W/m}^2$

HELEEOS irradiance: $4.795 \times 10^{-08} \text{ W/m}^2$

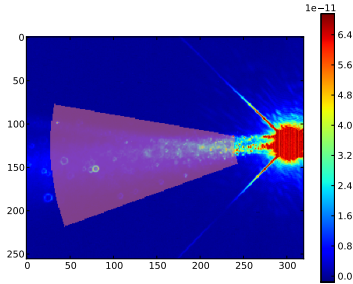
2009-07-15/2306.xvi (frames 4571-21983)

Optics: Large telescope

Distance: 3015 m

Off-axis angle: 0.900°

FOV range: 100 – 400 m



	Wavelength	Power
Lasers:	1.5326 μ m	0.60 W
	1.5857 μ m	0.60 W
	1.5953 μ m	0.60 W

DCCT irradiance: $9.283 \times 10^{-08} \pm 4.70 \times 10^{-09} \text{ W/m}^2$

HELEEOS irradiance: $1.444 \times 10^{-07} \text{ W/m}^2$

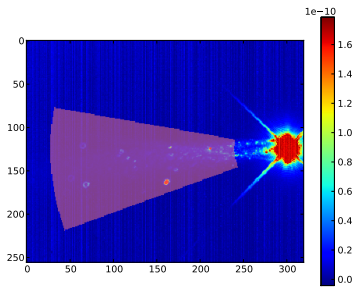
2009-07-15/2310.xvi (frames 1-2050)

Optics: Large telescope

Distance: 3015 m

Off-axis angle: 0.900°

FOV range: 100 – 400 m



	Wavelength	Power
Lasers:	1.5326 μ m	0.60 W
	1.5857 μ m	0.60 W
	1.5953 μ m	0.60 W

DCCT irradiance: $1.230 \times 10^{-07} \pm 4.98 \times 10^{-09} \text{ W/m}^2$

HELEEOS irradiance: $1.444 \times 10^{-07} \text{ W/m}^2$

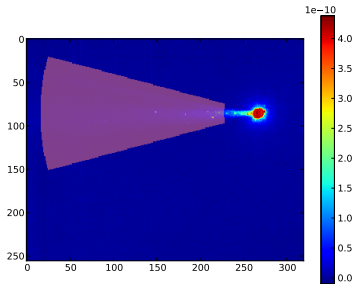
2009-07-15/2315-SmallTele.xvi (frames 1-2169)

Optics: Small telescope

Distance: 3015 m

Off-axis angle: 0.900°

FOV range: 299 – 1199 m



	Wavelength	Power
Lasers:	1.5326 μm	0.60 W
	1.5857 μm	0.60 W
	1.5953 μm	0.60 W

DCCT irradiance: $1.081 \times 10^{-07} \pm 4.46 \times 10^{-09} W/m^2$

HELEEOS irradiance: $7.515 \times 10^{-07} W/m^2$

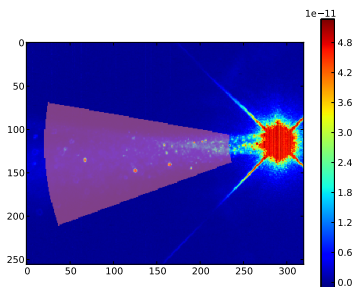
2009-07-15/2318.xvi (frames 1-4107)

Optics: Large telescope

Distance: 3015 m

Off-axis angle: 0.900°

FOV range: 100 – 400 m



	Wavelength	Power
Lasers:	1.5326 μm	0.60 W
	1.5857 μm	0.60 W
	1.5953 μm	0.60 W

DCCT irradiance: $5.174 \times 10^{-08} \pm 2.56 \times 10^{-09} W/m^2$

HELEEOS irradiance: $1.444 \times 10^{-07} W/m^2$

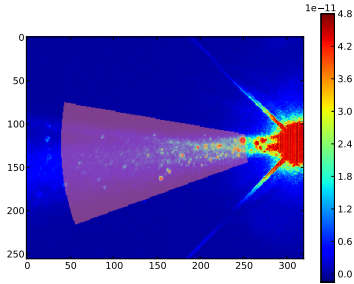
2009-07-15/2331.xvi (frames 1-1663)

Optics: Large telescope

Distance: 3015 m

Off-axis angle: 0.900°

FOV range: 100 – 400 m



	Wavelength	Power
Lasers:	1.5326 μ m	0.60 W
	1.5857 μ m	0.60 W
	1.5953 μ m	0.60 W

DCCT irradiance: $7.887 \times 10^{-08} \pm 4.49 \times 10^{-09} \text{ W/m}^2$

HELEEOS irradiance: $1.444 \times 10^{-07} \text{ W/m}^2$

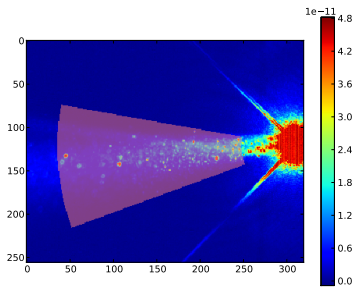
2009-07-15/2334.xvi (frames 1-1434)

Optics: Large telescope

Distance: 3015 m

Off-axis angle: 0.900°

FOV range: 100 – 400 m

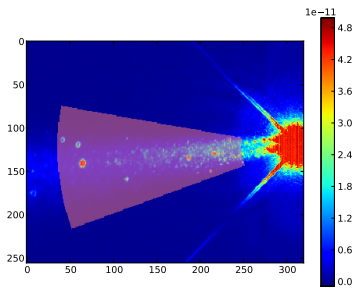


	Wavelength	Power
Lasers:	1.5857 μ m	0.60 W
	1.5326 μ m	0.60 W
	1.5953 μ m	0.60 W

DCCT irradiance: $7.433 \times 10^{-08} \pm 1.64 \times 10^{-09} \text{ W/m}^2$

HELEEOS irradiance: $4.795 \times 10^{-08} \text{ W/m}^2$

2009-07-15/2334.xvi (frames 1510-1612)



Optics: Large telescope

Distance: 3015 m

Off-axis angle: 0.900°

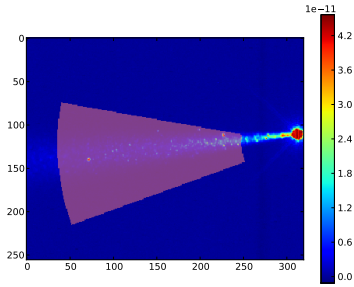
FOV range: 100 – 400 m

	Wavelength	Power
Lasers:	1.5857 μ m	0.60 W
	1.5953 μ m	0.60 W

DCCT irradiance: $6.837 \times 10^{-08} \pm 1.47 \times 10^{-09} \text{ W/m}^2$

HELEEOS irradiance: $4.795 \times 10^{-08} \text{ W/m}^2$

2009-07-15/2334.xvi (frames 1623-1910)



Optics: Large telescope

Distance: 3015 m

Off-axis angle: 0.900°

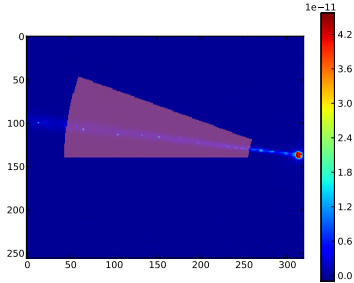
FOV range: 100 – 400 m

	Wavelength	Power
Lasers:	1.5857 μ m	0.60 W

DCCT irradiance: $2.199 \times 10^{-08} \pm 6.52 \times 10^{-10} \text{ W/m}^2$

HELEEOS irradiance: $4.795 \times 10^{-08} \text{ W/m}^2$

2009-07-15/2337.xvi (frames 3966-6004)



Optics: Large telescope

Distance: 3015 m

Off-axis angle: 0.900°

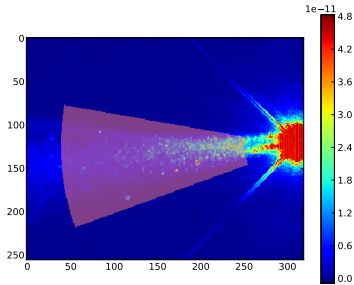
FOV range: 100 – 400 m

Lasers:	Wavelength	Power
	1.5857 μ m	0.60 W

DCCT irradiance: $6.077 \times 10^{-09} \pm 3.73 \times 10^{-10} \text{ W/m}^2$

HELEEOS irradiance: $4.795 \times 10^{-08} \text{ W/m}^2$

2009-07-15/2340.xvi (frames 1-3224)



Optics: Large telescope

Distance: 3015 m

Off-axis angle: 0.900°

FOV range: 100 – 400 m

Lasers:	Wavelength	Power
	1.5326 μ m	0.60 W
	1.5857 μ m	0.60 W
	1.5953 μ m	0.60 W

DCCT irradiance: $7.711 \times 10^{-08} \pm 2.20 \times 10^{-09} \text{ W/m}^2$

HELEEOS irradiance: $1.444 \times 10^{-07} \text{ W/m}^2$

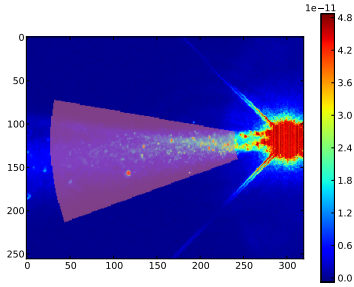
2009-07-15/2351.xvi (frames 1-2862)

Optics: Large telescope

Distance: 3015 m

Off-axis angle: 0.900°

FOV range: 100 – 400 m



	Wavelength	Power
Lasers:	1.5326 μ m	0.60 W
	1.5857 μ m	0.60 W
	1.5953 μ m	0.60 W

DCCT irradiance: $8.053 \times 10^{-08} \pm 4.07 \times 10^{-09} \text{ W/m}^2$

HELEEOS irradiance: $1.444 \times 10^{-07} \text{ W/m}^2$

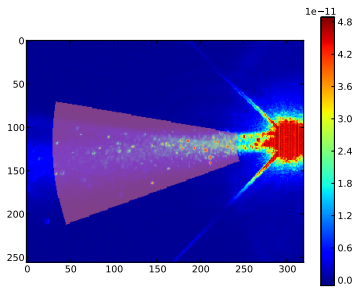
2009-07-15/2354.xvi (frames 1-3690)

Optics: Large telescope

Distance: 3015 m

Off-axis angle: 0.900°

FOV range: 100 – 400 m

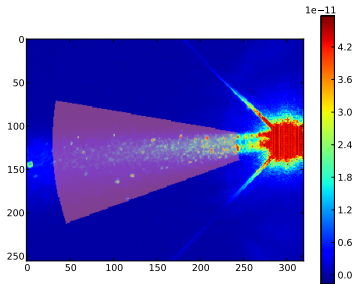


	Wavelength	Power
Lasers:	1.5857 μ m	0.60 W
	1.5326 μ m	0.60 W
	1.5953 μ m	0.60 W

DCCT irradiance: $8.093 \times 10^{-08} \pm 2.61 \times 10^{-09} \text{ W/m}^2$

HELEEOS irradiance: $1.444 \times 10^{-07} \text{ W/m}^2$

2009-07-15/2354.xvi (frames 3717-3874)



Optics: Large telescope

Distance: 3015 m

Off-axis angle: 0.900°

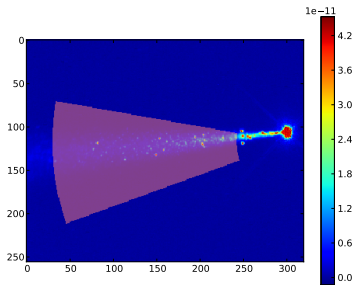
FOV range: 100 – 400 m

	Wavelength	Power
Lasers:	1.5857 μ m	0.60 W
	1.5953 μ m	0.60 W

DCCT irradiance: $7.570 \times 10^{-08} \pm 1.98 \times 10^{-09} \text{ W/m}^2$

HELEEOS irradiance: $1.444 \times 10^{-07} \text{ W/m}^2$

2009-07-15/2354.xvi (frames 3896-4014)



Optics: Large telescope

Distance: 3015 m

Off-axis angle: 0.900°

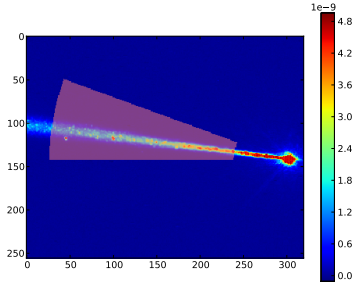
FOV range: 100 – 400 m

	Wavelength	Power
Lasers:	1.5857 μ m	0.60 W

DCCT irradiance: $2.534 \times 10^{-08} \pm 7.91 \times 10^{-10} \text{ W/m}^2$

HELEEOS irradiance: $1.444 \times 10^{-07} \text{ W/m}^2$

2009-07-15/2356.xvi (frames 5536-12133)



Optics: Large telescope

Distance: 3015 m

Off-axis angle: 0.900°

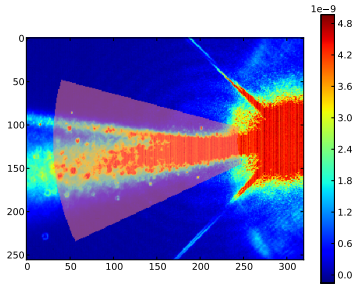
FOV range: 100 – 400 m

Lasers:	Wavelength	Power
	1.5953 μ m	5.40 W

DCCT irradiance: $5.133 \times 10^{-06} \pm 2.86 \times 10^{-07} \text{ W/m}^2$

HELEEOS irradiance: $4.252 \times 10^{-07} \text{ W/m}^2$

2009-07-15/2356.xvi (frames 12452-13903)



Optics: Large telescope

Distance: 3015 m

Off-axis angle: 0.900°

FOV range: 100 – 400 m

Lasers:	Wavelength	Power
	1.5326 μ m	5.70 W
	1.5857 μ m	5.60 W
	1.5953 μ m	5.40 W

DCCT irradiance: $3.904 \times 10^{-05} \pm 1.31 \times 10^{-06} \text{ W/m}^2$

HELEEOS irradiance: $1.340 \times 10^{-06} \text{ W/m}^2$

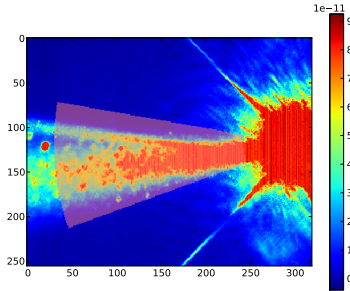
2009-07-15/2358.xvi (frames 1-21247)

Optics: Large telescope

Distance: 3015 m

Off-axis angle: 0.900°

FOV range: 100 – 400 m



	Wavelength	Power
Lasers:	1.5326 μ m	5.50 W
	1.5857 μ m	5.50 W
	1.5953 μ m	5.70 W

DCCT irradiance: $5.828 \times 10^{-07} \pm 6.60 \times 10^{-08} \text{ W/m}^2$

HELEEOS irradiance: $1.340 \times 10^{-06} \text{ W/m}^2$

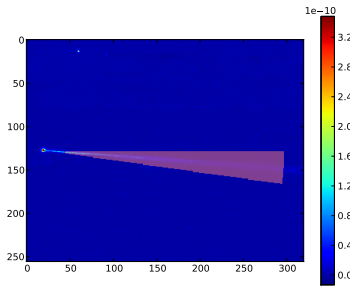
2009-07-17/0700.xvi (frames 4185-7401)

Optics: Small telescope

Distance: 2160 m

Off-axis angle: 1.220°

FOV range: 99 – 749 m

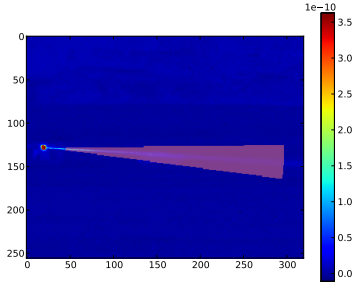


	Wavelength	Power
Lasers:	1.5326 μ m	0.60 W

DCCT irradiance: $3.601 \times 10^{-08} \pm 5.65 \times 10^{-09} \text{ W/m}^2$

HELEEOS irradiance: $2.627 \times 10^{-07} \text{ W/m}^2$

2009-07-17/0708.xvi (frames 1-5178)



Optics: Small telescope

Distance: 2160 m

Off-axis angle: 1.220°

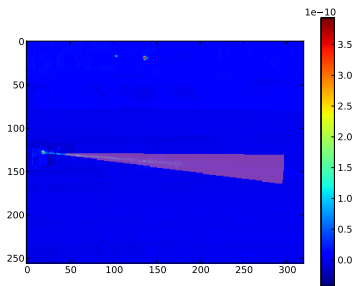
FOV range: 99 – 749 m

Lasers:	Wavelength	Power
	1.5326 μ m	0.60 W

DCCT irradiance: $2.974 \times 10^{-08} \pm 2.49 \times 10^{-09} \text{ W/m}^2$

HELEEOS irradiance: $2.626 \times 10^{-07} \text{ W/m}^2$

2009-07-17/0712.xvi (frames 1-6274)



Optics: Small telescope

Distance: 2160 m

Off-axis angle: 1.220°

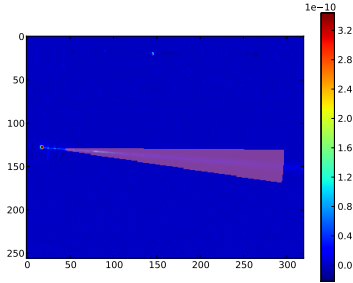
FOV range: 99 – 749 m

Lasers:	Wavelength	Power
	1.5887 μ m	0.60 W

DCCT irradiance: $2.494 \times 10^{-08} \pm 1.86 \times 10^{-09} \text{ W/m}^2$

HELEEOS irradiance: $2.521 \times 10^{-07} \text{ W/m}^2$

2009-07-17/0725.xvi (frames 3685-11954)



Optics: Small telescope

Distance: 2160 m

Off-axis angle: 1.220°

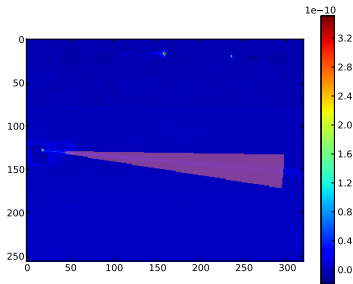
FOV range: 99 – 749 m

Lasers:	Wavelength	Power
	1.5326 μ m	0.60 W

DCCT irradiance: $2.184 \times 10^{-08} \pm 2.52 \times 10^{-09} \text{ W/m}^2$

HELEEOS irradiance: $2.626 \times 10^{-07} \text{ W/m}^2$

2009-07-17/0728.xvi (frames 1-4755)



Optics: Small telescope

Distance: 2160 m

Off-axis angle: 1.220°

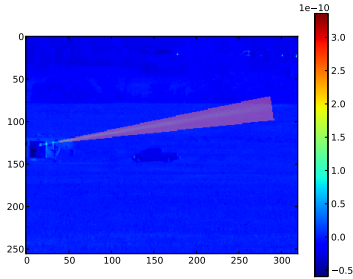
FOV range: 99 – 750 m

Lasers:	Wavelength	Power
	1.5887 μ m	0.60 W

DCCT irradiance: $1.607 \times 10^{-08} \pm 1.66 \times 10^{-09} \text{ W/m}^2$

HELEEOS irradiance: $2.522 \times 10^{-07} \text{ W/m}^2$

2009-07-17/0730.xvi (frames 1-8817)



Optics: Small telescope

Distance: 2160 m

Off-axis angle: 1.220°

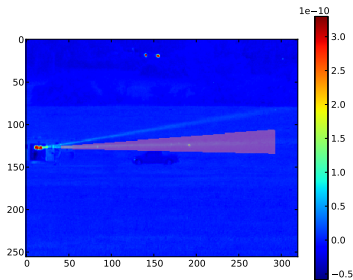
FOV range: 99 – 749 m

Lasers:	Wavelength	Power
	1.5326 μ m	0.60 W

DCCT irradiance: $2.075 \times 10^{-08} \pm 1.93 \times 10^{-09} \text{ W/m}^2$

HELEEOS irradiance: $2.626 \times 10^{-07} \text{ W/m}^2$

2009-07-17/0730.xvi (frames 2049-5952)



Optics: Small telescope

Distance: 2160 m

Off-axis angle: 1.220°

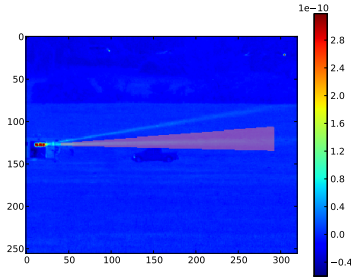
FOV range: 99 – 749 m

Lasers:	Wavelength	Power
	1.5887 μ m	0.60 W

DCCT irradiance: $2.532 \times 10^{-08} \pm 9.00 \times 10^{-09} \text{ W/m}^2$

HELEEOS irradiance: $2.520 \times 10^{-07} \text{ W/m}^2$

2009-07-17/0730.xvi (frames 5981-8817)



Optics: Small telescope

Distance: 2160 m

Off-axis angle: 1.220°

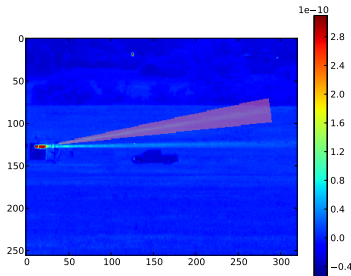
FOV range: 99 – 749 m

	Wavelength	Power
Lasers:	1.5887 μm	0.60 W
	1.5953 μm	0.60 W

DCCT irradiance: $2.532 \times 10^{-08} \pm 9.01 \times 10^{-09} \text{ W/m}^2$

HELEEOS irradiance: $2.520 \times 10^{-07} \text{ W/m}^2$

2009-07-17/0734.xvi (frames 1-3147)



Optics: Small telescope

Distance: 2160 m

Off-axis angle: 1.220°

FOV range: 99 – 750 m

	Wavelength	Power
Lasers:	1.5326 μm	0.60 W

DCCT irradiance: $2.300 \times 10^{-08} \pm 8.71 \times 10^{-09} \text{ W/m}^2$

HELEEOS irradiance: $2.628 \times 10^{-07} \text{ W/m}^2$

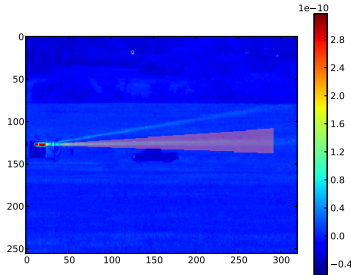
2009-07-17/0734.xvi (frames 1-3147)

Optics: Small telescope

Distance: 2160 m

Off-axis angle: 1.220°

FOV range: 99 – 750 m



	Wavelength	Power
Lasers:	1.5887 μ m	0.60 W
	1.5953 μ m	0.60 W

DCCT irradiance: $3.844 \times 10^{-08} \pm 8.64 \times 10^{-09} \text{ W/m}^2$

HELEEOS irradiance: $2.522 \times 10^{-07} \text{ W/m}^2$

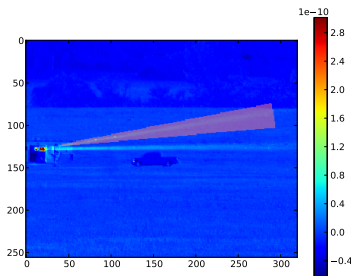
2009-07-17/0736.xvi (frames 1-5702)

Optics: Small telescope

Distance: 2160 m

Off-axis angle: 1.220°

FOV range: 99 – 749 m

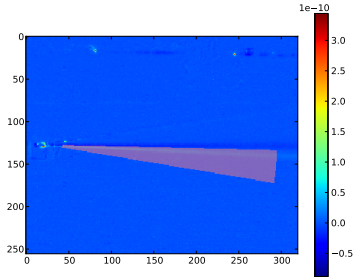


	Wavelength	Power
Lasers:	1.5326 μ m	0.60 W

DCCT irradiance: $1.967 \times 10^{-08} \pm 1.81 \times 10^{-09} \text{ W/m}^2$

HELEEOS irradiance: $2.627 \times 10^{-07} \text{ W/m}^2$

2009-07-17/0736.xvi (frames 1853-5702)



Optics: Small telescope

Distance: 2160 m

Off-axis angle: 1.220°

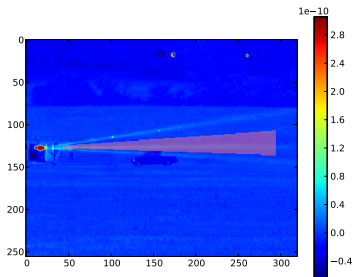
FOV range: 99 – 749 m

Lasers:	Wavelength	Power
	1.5953 μ m	0.60 W

DCCT irradiance: $1.624 \times 10^{-08} \pm 1.22 \times 10^{-09} \text{ W/m}^2$

HELEEOS irradiance: $2.489 \times 10^{-07} \text{ W/m}^2$

2009-07-17/0736.xvi (frames 1936-5702)



Optics: Small telescope

Distance: 2160 m

Off-axis angle: 1.220°

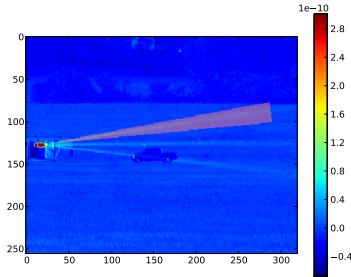
FOV range: 99 – 749 m

Lasers:	Wavelength	Power
	1.5887 μ m	0.60 W

DCCT irradiance: $8.832 \times 10^{-09} \pm 1.73 \times 10^{-09} \text{ W/m}^2$

HELEEOS irradiance: $2.521 \times 10^{-07} \text{ W/m}^2$

2009-07-17/0737.xvi (frames 1-3224)



Optics: Small telescope

Distance: 2160 m

Off-axis angle: 1.220°

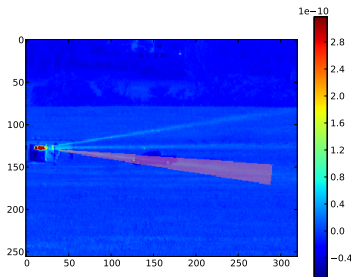
FOV range: 99 – 750 m

Lasers:	Wavelength	Power
	1.5326 μ m	0.60 W

DCCT irradiance: $2.101 \times 10^{-08} \pm 1.67 \times 10^{-09} \text{ W/m}^2$

HELEEOS irradiance: $2.627 \times 10^{-07} \text{ W/m}^2$

2009-07-17/0737.xvi (frames 1-3224)



Optics: Small telescope

Distance: 2160 m

Off-axis angle: 1.220°

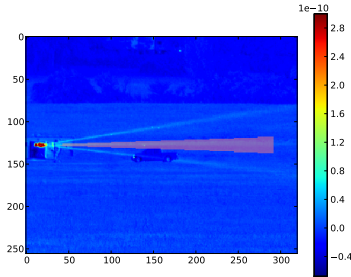
FOV range: 99 – 750 m

Lasers:	Wavelength	Power
	1.5953 μ m	0.60 W

DCCT irradiance: $4.868 \times 10^{-09} \pm 1.67 \times 10^{-09} \text{ W/m}^2$

HELEEOS irradiance: $2.490 \times 10^{-07} \text{ W/m}^2$

2009-07-17/0737.xvi (frames 1-3224)



Optics: Small telescope

Distance: 2160 m

Off-axis angle: 1.220°

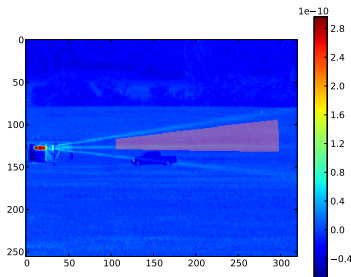
FOV range: 99 – 750 m

Lasers:	Wavelength	Power
	1.5887 μ m	0.60 W

DCCT irradiance: $1.145 \times 10^{-08} \pm 1.31 \times 10^{-09} \text{ W/m}^2$

HELEEOS irradiance: $2.521 \times 10^{-07} \text{ W/m}^2$

2009-07-17/0738.xvi (frames 1-6334)



Optics: Small telescope

Distance: 2160 m

Off-axis angle: 1.220°

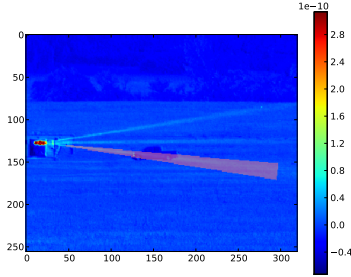
FOV range: 300 – 749 m

Lasers:	Wavelength	Power
	1.5887 μ m	0.60 W

DCCT irradiance: $8.973 \times 10^{-09} \pm 2.59 \times 10^{-09} \text{ W/m}^2$

HELEEOS irradiance: $1.831 \times 10^{-07} \text{ W/m}^2$

2009-07-17/0738.xvi (frames 1-9193)



Optics: Small telescope

Distance: 2160 m

Off-axis angle: 1.220°

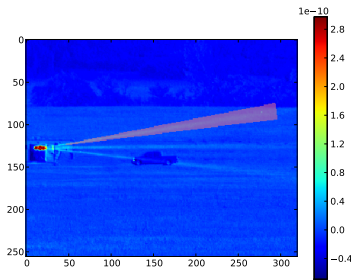
FOV range: 99 – 749 m

Lasers:	Wavelength	Power
	1.5953 μ m	0.60 W

DCCT irradiance: $7.416 \times 10^{-09} \pm 1.59 \times 10^{-09} \text{ W/m}^2$

HELEEOS irradiance: $2.453 \times 10^{-07} \text{ W/m}^2$

2009-07-17/0738.xvi (frames 1-6060)



Optics: Small telescope

Distance: 2160 m

Off-axis angle: 1.220°

FOV range: 99 – 749 m

Lasers:	Wavelength	Power
	1.5326 μ m	0.60 W

DCCT irradiance: $1.774 \times 10^{-08} \pm 1.45 \times 10^{-09} \text{ W/m}^2$

HELEEOS irradiance: $2.627 \times 10^{-07} \text{ W/m}^2$

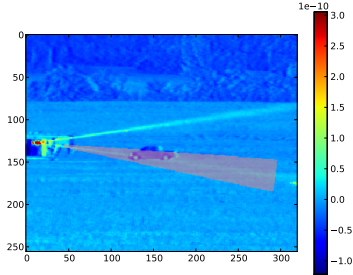
2009-07-17/0742.xvi (frames 1-889)

Optics: Small telescope

Distance: 2160 m

Off-axis angle: 1.220°

FOV range: 99 – 750 m



Lasers:	Wavelength	Power
	1.5953 μ m	0.60 W

DCCT irradiance: $1.206 \times 10^{-06} \pm 9.62 \times 10^{-08} \text{ W/m}^2$

HELEEOS irradiance: $5.150 \times 10^{-07} \text{ W/m}^2$

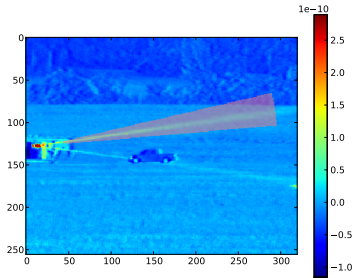
2009-07-17/0742.xvi (frames 1-889)

Optics: Small telescope

Distance: 2160 m

Off-axis angle: 1.220°

FOV range: 99 – 750 m

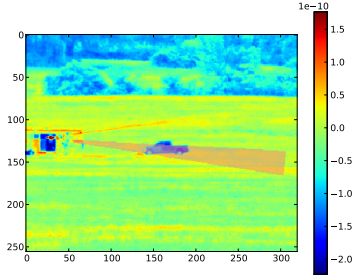


Lasers:	Wavelength	Power
	1.5326 μ m	0.60 W
	1.5887 μ m	0.60 W

DCCT irradiance: $1.229 \times 10^{-06} \pm 2.83 \times 10^{-08} \text{ W/m}^2$

HELEEOS irradiance: $5.150 \times 10^{-07} \text{ W/m}^2$

2009-07-17/0806.xvi (frames 1-3224)



Optics: Small telescope

Distance: 2160 m

Off-axis angle: 1.220°

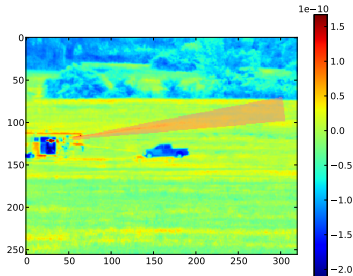
FOV range: 99 – 750 m

Lasers:	Wavelength	Power
	1.5953 μm	0.60 W

DCCT irradiance: $-2.386 \times 10^{-08} \pm 2.85 \times 10^{-08} \text{ W/m}^2$

HELEEOS irradiance: $2.491 \times 10^{-07} \text{ W/m}^2$

2009-07-17/0806.xvi (frames 1-3224)



Optics: Small telescope

Distance: 2160 m

Off-axis angle: 1.220°

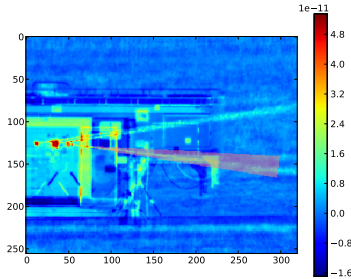
FOV range: 99 – 750 m

Lasers:	Wavelength	Power
	1.5326 μm	0.60 W
	1.5887 μm	0.60 W

DCCT irradiance: $6.042 \times 10^{-08} \pm 2.70 \times 10^{-08} \text{ W/m}^2$

HELEEOS irradiance: $5.150 \times 10^{-07} \text{ W/m}^2$

2009-07-17/0811.xvi (frames 1-3224)



Optics: Large telescope

Distance: 2160 m

Off-axis angle: 1.220°

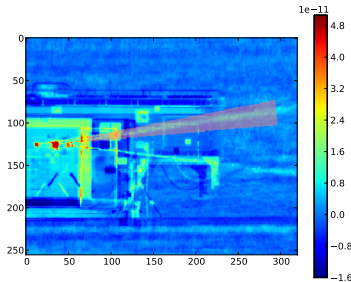
FOV range: 24 – 199 m

Lasers:	Wavelength	Power
	1.5953 μm	0.60 W

DCCT irradiance: $1.106 \times 10^{-08} \pm 8.02 \times 10^{-10} \text{ W/m}^2$

HELEEOS irradiance: $4.567 \times 10^{-08} \text{ W/m}^2$

2009-07-17/0811.xvi (frames 1-3224)



Optics: Large telescope

Distance: 2160 m

Off-axis angle: 1.220°

FOV range: 50 – 225 m

Lasers:	Wavelength	Power
	1.5887 μm	0.60 W
	1.5326 μm	0.60 W

DCCT irradiance: $1.554 \times 10^{-08} \pm 9.20 \times 10^{-10} \text{ W/m}^2$

HELEEOS irradiance: $9.773 \times 10^{-08} \text{ W/m}^2$

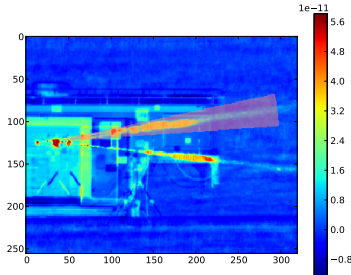
2009-07-17/0815.xvi (frames 1-6585)

Optics: Large telescope

Distance: 2160 m

Off-axis angle: 1.220°

FOV range: 24 – 219 m



	Wavelength	Power
Lasers:	1.5887 μm	0.60 W
	1.5326 μm	0.60 W

DCCT irradiance: $3.578 \times 10^{-08} \pm 7.17 \times 10^{-09} \text{ W/m}^2$

HELEEOS irradiance: $1.082 \times 10^{-07} \text{ W/m}^2$

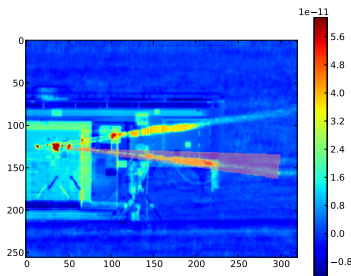
2009-07-17/0815.xvi (frames 1-6585)

Optics: Large telescope

Distance: 2160 m

Off-axis angle: 1.220°

FOV range: 24 – 220 m



	Wavelength	Power
Lasers:	1.5953 μm	0.60 W

DCCT irradiance: $2.569 \times 10^{-08} \pm 5.29 \times 10^{-09} \text{ W/m}^2$

HELEEOS irradiance: $5.239 \times 10^{-08} \text{ W/m}^2$

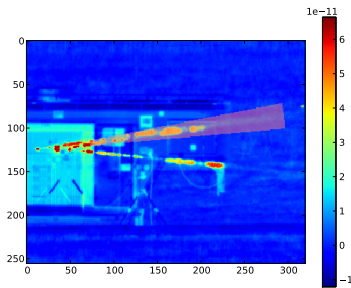
2009-07-17/0817.xvi (frames 1-20234)

Optics: Large telescope

Distance: 2160 m

Off-axis angle: 1.220°

FOV range: 49 – 225 m



	Wavelength	Power
Lasers:	1.5887 μm	0.60 W
	1.5326 μm	0.60 W

DCCT irradiance: $1.984 \times 10^{-08} \pm 8.37 \times 10^{-09} \text{ W/m}^2$

HELEEOS irradiance: $9.843 \times 10^{-08} \text{ W/m}^2$

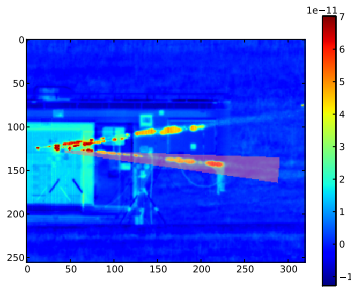
2009-07-17/0817.xvi (frames 1-20234)

Optics: Large telescope

Distance: 2160 m

Off-axis angle: 1.220°

FOV range: 24 – 220 m

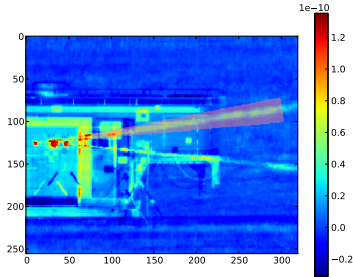


	Wavelength	Power
Lasers:	1.5953 μm	0.60 W

DCCT irradiance: $1.955 \times 10^{-08} \pm 6.82 \times 10^{-09} \text{ W/m}^2$

HELEEOS irradiance: $5.239 \times 10^{-08} \text{ W/m}^2$

2009-07-17/0819.xvi (frames 1-3224)



Optics: Large telescope

Distance: 2160 m

Off-axis angle: 1.220°

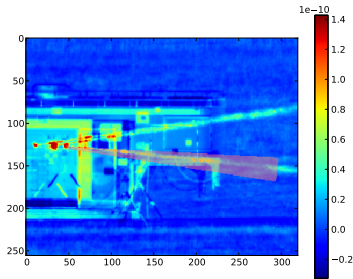
FOV range: 49 – 224 m

	Wavelength	Power
Lasers:	1.5326 μ m	0.60 W
	1.5887 μ m	0.60 W

DCCT irradiance: $7.497 \times 10^{-08} \pm 3.29 \times 10^{-09} \text{ W/m}^2$

HELEEOS irradiance: $9.829 \times 10^{-08} \text{ W/m}^2$

2009-07-17/0819.xvi (frames 1-3224)



Optics: Large telescope

Distance: 2160 m

Off-axis angle: 1.220°

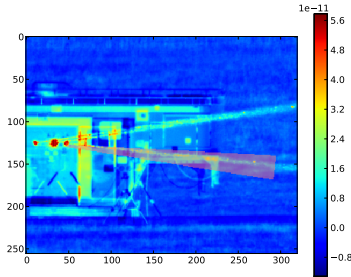
FOV range: 24 – 220 m

	Wavelength	Power
Lasers:	1.5953 μ m	0.60 W

DCCT irradiance: $6.986 \times 10^{-08} \pm 2.86 \times 10^{-09} \text{ W/m}^2$

HELEEOS irradiance: $5.147 \times 10^{-08} \text{ W/m}^2$

2009-07-17/0820.xvi (frames 1-3224)



Optics: Large telescope

Distance: 2160 m

Off-axis angle: 1.220°

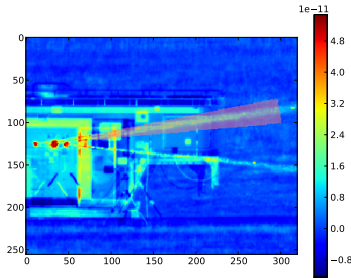
FOV range: 24 – 220 m

Lasers:	Wavelength	Power
	1.5953 μ m	0.60 W

DCCT irradiance: $2.657 \times 10^{-08} \pm 9.56 \times 10^{-10} \text{ W/m}^2$

HELEEOS irradiance: $5.227 \times 10^{-08} \text{ W/m}^2$

2009-07-17/0820.xvi (frames 1-3224)



Optics: Large telescope

Distance: 2160 m

Off-axis angle: 1.220°

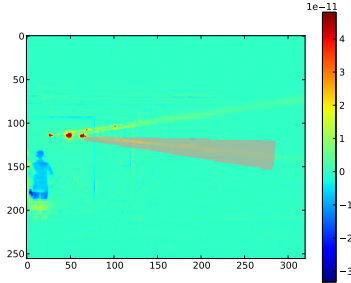
FOV range: 49 – 224 m

Lasers:	Wavelength	Power
	1.5326 μ m	0.60 W
	1.5887 μ m	0.60 W

DCCT irradiance: $2.718 \times 10^{-08} \pm 9.34 \times 10^{-10} \text{ W/m}^2$

HELEEOS irradiance: $9.829 \times 10^{-08} \text{ W/m}^2$

2009-07-17/0843.xvi (frames 1-2232)



Optics: Large telescope

Distance: 2160 m

Off-axis angle: 1.220°

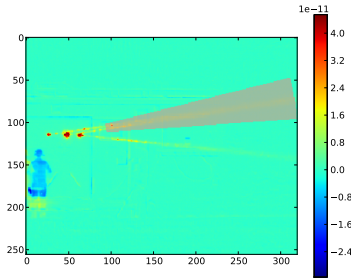
FOV range: 24 – 199 m

Lasers:	Wavelength	Power
	1.5953 μm	0.60 W

DCCT irradiance: $3.917 \times 10^{-09} \pm 1.01 \times 10^{-09} \text{ W/m}^2$

HELEEOS irradiance: $4.646 \times 10^{-08} \text{ W/m}^2$

2009-07-17/0843.xvi (frames 1-1594)



Optics: Large telescope

Distance: 2160 m

Off-axis angle: 1.220°

FOV range: 49 – 224 m

Lasers:	Wavelength	Power
	1.5887 μm	0.60 W
	1.5326 μm	0.60 W

DCCT irradiance: $5.660 \times 10^{-09} \pm 4.25 \times 10^{-10} \text{ W/m}^2$

HELEEOS irradiance: $9.829 \times 10^{-08} \text{ W/m}^2$

Bibliography

- [1] “ABL YAL 1A Airborne Laser, USA”, July 2009.
<http://www.airforce-technology.com/projects/abl/>.
- [2] “Advanced Tactical Laser (ATL)”, July 2005.
<http://www.globalsecurity.org/military/systems/aircraft/systems/at1.htm>.
- [3] Belton, Scott L. *The Simulation of Off Axis Laser Propagation Using Helecos*. Master’s thesis, Graduate School of Engineering, Air Force Institute of Technology (AETC), Wright-Patterson AFB OH, March 2006. AFIT/GSS/ENP/06-01.
- [4] Bergeron, Bryan P. “A Laser-Communications Primer—Part 1”. *QST*, September 1990. URL <http://www.arrl.org/tis/info/pdf/9009019.pdf>.
- [5] Bevington, Philip R and D Keith Robinson. *Data Reduction and Error Analysis for the Physical Sciences*. McGraw-Hill, 3rd edition, 2003.
- [6] Boyd, Robert W. *Radiometry and the Detection of Optical Radiation*. John Wiley & Sons, Inc., 1983.
- [7] CI Systems. “Acceptance Test Report (ATR), SR-80-4HT/7HT/12HT High Temperature Absolute Blackbody”, 2007.
- [8] Cohen, Capt Jean. “Laser Safety Plan, MZA Long Range Turbulence Profiler - Gen II”, June 2009.
- [9] Dereniak, Eustace L. and G.D. Boreman. *Infrared Detectors and Systems*. John Wiley & Sons, Inc., 1996.
- [10] Fiorino, S. T., R. J. Bartell, G. P. Perram, D. W. Bunch, L. E. Gravley, C. A. Rice, Z. P. Manning, and M. J. Krizo. “The HELEEOS Atmospheric Effects Package: A Probabilistic Method for Evaluating Uncertainty in Low-Altitude High Energy Laser Effectiveness”. *Journal of Directed Energy*, 2006.
- [11] Fiorino, Steven T. Personal communication, 2009.
- [12] Gruner, William. Personal communication, 2009.
- [13] Louthain, James A. *Integrated Approach to Airborne Laser Communication*. Ph.D. dissertation, Graduate School of Engineering, Air Force Institute of Technology (AETC), Wright-Patterson AFB OH, September 2002. AFIT/DEE/ENG/09-02.
- [14] Petty, Grant W. *A First Course in Atmospheric Radiation*. Sundog Publishing, 2006.

- [15] Rasmussen, Carl Edward and Christopher K.I. Williams. *Gaussian Process Regression for Machine Learning*. MIT Press, 2006. ISBN 978-0-262-18253-9. URL <http://www.gaussianprocess.org/gpml/>.
- [16] Rice, Chris. Personal communication, 2009.
- [17] Smith, Greg. Personal communication, 2009.
- [18] Weichel, Hugo. *Laser beam propagation in the Atmosphere*. SPIE Optical Engineering Press, 1990.
- [19] Wiscombe, W.J. "Improved Mie scattering algorithms". *Applied Optics*, 19(9), 1980.
- [20] Xenics. "XS-1.7-320", 2010. URL http://xenics.com/documents/20090714_LR_XS-1.7-320_scientific_A4.pdf.
- [21] Yang, Ping, Qian Feng, Gang Hong, George W. Kattawar, Warren J. Wiscombe, Michael I. Mishchenko, Oleg Dubovik, Istvan Laszlo, and Irina N. Sokolik. "Modeling of the scattering and radiative properties of nonspherical dust-like aerosols". *Journal of Aerosol Science*, 2007.
- [22] Zuev, V. E. *Laser Beams in the Atmosphere*. Consultants Bureau, 1982.

Vita

1Lt John Haiducek was born in Midland, Michigan, spending part of his childhood years in Sarnia, Canada. After graduating from Dow High School in Midland, he spent one year at the University of Michigan, later graduating from the U.S. Air Force Academy with a Bachelor's Degree in Physics in May 2006. He was then assigned to the Air Force Technical Applications Center (AFTAC) at Patrick Air Force Base, Florida, where he worked in nuclear treaty monitoring. He entered graduate school at the Air Force Institute of Technology in August 2008, where he is currently completing his Master's Degree. His anticipated follow-on assignment is to the Air Force Research Labs Directed Energy Directorate (AFRL/RD) at Kirtland Air Force Base, New Mexico.

REPORT DOCUMENTATION PAGE

Form Approved
OMB No. 0704-0188

The public reporting burden for this collection of information is estimated to average 1 hour per response, including the time for reviewing instructions, searching existing data sources, gathering and maintaining the data needed, and completing and reviewing the collection of information. Send comments regarding this burden estimate or any other aspect of this collection of information, including suggestions for reducing this burden to Department of Defense, Washington Headquarters Services, Directorate for Information Operations and Reports (0704-0188), 1215 Jefferson Davis Highway, Suite 1204, Arlington, VA 22202-4302. Respondents should be aware that notwithstanding any other provision of law, no person shall be subject to any penalty for failing to comply with a collection of information if it does not display a currently valid OMB control number. **PLEASE DO NOT RETURN YOUR FORM TO THE ABOVE ADDRESS.**

1. REPORT DATE (DD-MM-YYYY) 25-03-2010		2. REPORT TYPE Master's Thesis		3. DATES COVERED (From — To) Aug 2008 — Mar 2010	
4. TITLE AND SUBTITLE EXPERIMENTAL VALIDATION TECHNIQUES FOR THE HELEEOS OFF-AXIS LASER PROPAGATION MODEL				5a. CONTRACT NUMBER	
				5b. GRANT NUMBER	
				5c. PROGRAM ELEMENT NUMBER	
6. AUTHOR(S) Haiducek, John D., 1st Lt, USAF				5d. PROJECT NUMBER	
				5e. TASK NUMBER	
				5f. WORK UNIT NUMBER	
7. PERFORMING ORGANIZATION NAME(S) AND ADDRESS(ES) Air Force Institute of Technology Graduate School of Engineering and Management (AFIT/EN) 2950 Hobson Way WPAFB OH 45433-7765				8. PERFORMING ORGANIZATION REPORT NUMBER AFIT/GAP/ENP/10-M07	
9. SPONSORING / MONITORING AGENCY NAME(S) AND ADDRESS(ES) Maj Bryan Best National Science Foundation - The National Consortium for Measures and Signatures Intelligence (MASINT) Research 1030 S Highway AIA Patrick AFB, FL 32925				10. SPONSOR/MONITOR'S ACRONYM(S) NSF-NCMR	
				11. SPONSOR/MONITOR'S REPORT NUMBER(S)	
12. DISTRIBUTION / AVAILABILITY STATEMENT APPROVED FOR PUBLIC RELEASE; DISTRIBUTION UNLIMITED.					
13. SUPPLEMENTARY NOTES					
14. ABSTRACT The High Energy Laser End-to-End Operational Simulation (HELEEOS) off-axis scattering algorithm is designed to predict the irradiance that will be detected at a given off-axis location due to atmospheric scattering of a high-energy laser. The HELEEOS system models the propagation of the laser through the atmosphere, accounting for such effects as turbulence, thermal blooming, and atmospheric absorption. The HELEEOS off-axis scattering algorithm uses the scattering phase functions of the Mie scattering models to predict the amount of radiation that will be scattered toward a particular observation location from each point along the beam path, and the total irradiance that will be received at that location. Algorithm outputs were compared with data from a laser test conducted at Wright-Patterson Air Force Base using 1.53-1.59 μm communications lasers operating at 0.6 W of power. The off-axis irradiance was measured using an Indium Gallium Arsenide (InGaAs) camera. A software application was developed to assist in camera calibration and the analysis of the collected images. The application was used to reduce the data from each image to a single irradiance value which could be compared with HELEEOS predictions. Preliminary results show an agreement within 1-2 orders of magnitude between the HELEEOS algorithm and the measured off-axis irradiance, although the potential exists for improving this result through more detailed analysis of the same data set.					
15. SUBJECT TERMS					
16. SECURITY CLASSIFICATION OF:			17. LIMITATION OF ABSTRACT	18. NUMBER OF PAGES	19a. NAME OF RESPONSIBLE PERSON
a. REPORT	b. ABSTRACT	c. THIS PAGE			Dr. Steven T. Fiorino
U	U	U	U	142	19b. TELEPHONE NUMBER (include area code) (937) 255-3636, x4506; steven.fiorino@afit.edu

Standard Form 298 (Rev. 8-98)
Prescribed by ANSI Std. Z39.18